

Cyclotron resonant scattering features in the line forming region of highly magnetized neutron stars

Diploma Thesis in Physics

submitted by

Fritz-Walter Schwarm

Advisor: Prof. Dr. Jörn Wilms

Dr. Karl Remeis Observatory Bamberg, Astronomical Institute of the
Friedrich-Alexander-University of Erlangen-Nürnberg

September 14, 2010

Abstract

Like all objects in the universe, a star has a finite lifetime. Once its fuel is exhausted, the star collapses leaving a remnant. Three types of remnants are known: Black hole candidates, white dwarfs and neutron stars. All of them exhibit magnetic fields, the determination of whose is challenging. Cyclotron resonant scattering features (CRSF) provide a way to do so. They are observed at neutron stars with magnetic fields way beyond the strongest magnetic fields that can be produced in laboratories on earth. This thesis focuses on the theoretical formation of these features and how they can be simulated using Monte-Carlo methods. Such simulations are rather complicated due to their dependence on a large set of parameters. The thesis discusses how these parameters can be obtained numerically and what they imply for the physical processes leading to CRSFs. Up to the date of submission more than 10000 lines of source code have been written (exactly 10230 excluding blank lines) providing functions that calculate, interpolate and sample parameters involved in the line formation process. In contrast to other simulation approaches a fully relativistic quantum mechanical treatment is applied allowing the expandability to future requirements. This is computationally expensive. Therefore parallelization is utilized to speed up calculations by using more than one CPU. Interim results have been compared to literature and to corresponding results from Osamu Nishimura in the course of a international collaboration. Furthermore the compatibility to a recent macro-physical model of Peter Becker and Michael Wolff has been discussed with the authors and was found to be feasible. Up to now, there are 17 neutron stars known exhibiting a CRSF. Future missions like NuSTAR, however, will be able to resolve not only the CRSFs themselves, but their shape also. Bringing together the micro- and macro-physics will allow for drawing conclusions from line shapes. For that reason a unified model is of major significance. This thesis is a step forward to such a model.

Contents

1	Introduction	6
1.1	Neutron Stars and Their Magnetic Fields	6
1.2	Accretion mechanisms	7
1.3	Accretion column	9
1.3.1	Optical depth	9
1.3.2	Influence of strong magnetic fields	10
1.3.3	Position of the line forming region	11
1.3.4	Temperature and electron momentum distribution	13
1.3.5	Measuring a neutron star’s magnetic field	14
1.4	Structure of this thesis	16
2	Electrons in strong magnetic fields	18
2.1	Classical treatment	18
2.2	Quantum mechanical treatment	18
2.2.1	Non-relativistic	19
2.2.2	Relativistic	19
2.3	Cyclotron resonant scattering features	20
2.3.1	Cyclotron emission	20
2.3.2	Absorption cross section	21
2.3.3	Scattering cross section	22
3	A photon’s history	25
3.1	Mean free path and profile functions	26
3.2	Electron momentum	28
3.3	Initial and final Landau level	28
3.4	Scattering angle	30
3.5	Kinematics	30
3.6	Photon spawning	31
3.6.1	The spawning process	31
3.6.2	Decay rates	31
3.6.3	Branching ratios and consequences	32
4	Simulation of CRSF	35
4.1	Model geometries	35
4.2	Model continua and photon injection	35
4.3	Numerical approaches	36
4.4	MC code: 1st revision	36
4.4.1	Aims: First comparison of the MC model with observational data . . .	37
4.4.2	Restrictions	37
4.4.3	Results	37
4.5	MC code: 2nd revision	38
4.5.1	Aims: Revision of the means free path sampling	39
4.5.2	Numerical methods: Adaptive Simpson integration	39
4.5.3	Numerical methods: Adaptive grid refinement	39
4.5.4	Computational methods: Multiprocessing	41
4.5.5	Mean free path sampling	44
4.5.6	Results	46

4.6	MC code: 3rd revision	48
4.6.1	Aims: Revised momentum sampling	48
4.6.2	Numerical methods: Binary search	49
4.6.3	Momentum sampling	49
4.6.4	Results	50
4.7	CycloSim: The new Code	52
4.7.1	Aims: Less restrictions and a readable and maintainable source code . .	52
4.7.2	Restrictions	55
4.7.3	Results	55
5	Summary and outlook	58

List of Figures

1	Sketch of accretion and Her X-1 spectrum	8
2	Variations of the X-ray flux of Vela X-1	9
3	Sketch of an accreting neutron star showing the Alfvén surface and the hot spot formation	10
4	Sketch of an accretion column in the super-Eddington regime	11
5	Correlations between the luminosity and the cyclotron energy	13
6	Sources with cyclotron lines and their magnetic fields	15
7	Spectrum of 4 U0115+63	16
8	Feynman diagram for cyclotron emission	20
9	Feynman diagram for cyclotron absorption	21
10	Feynman diagrams for cyclotron scattering	23
11	Compton scattering cross section with respect to energy	24
12	Compton scattering cross section with respect to electron parallel momentum	24
13	Flow chart of a Monte-Carlo process propagating photons through a CRSF medium	25
14	Thermally averaged compton cross sections	27
15	Sampling of final Landau level	29
16	Decay rates for initial Landau level $n_i = 2$	32
17	Decay rates for initial Landau level $n_i = 1$	33
18	Differential decay rates with respect to the emission angle	33
19	Simulated spectra for the first revision of the MC code	38
20	Sampled electron momenta and mean free paths for revision 1	38
21	Number of momentum grid points with respect to the energy	40
22	Number of energy grid points with respect to the angle	40
23	3D-Plot of profile interpolation table	42
24	Screenshot of the output of <i>Traceanalyzer</i>	44
25	Comparison of sampled mean free path for 1st and 2nd revision of the MC code	45
26	Comparison of the profiles from Harding & Daugherty (1991) to own calculations	45
27	Comparison of the profiles from O. Nishimura to own calculations	46
28	Comparison of the spectra resulting from revisions 1 and 2 for slab 1-0 geometry	47
29	Comparison of the spectra resulting from revisions 1 and 2 for slab 1-1 geometry	47
30	Comparison of the spectra resulting from revisions 1 and 2 for cylinder geometry	48
31	Comparison of the spectra resulting from revisions 1 and 2 for different optical depths	49
32	Profiles sampled from MC code revision 3 for $\mu = 0$	50
33	Profiles sampled from MC code revision 3 for $\mu = 0.5$	51
34	Profiles sampled from MC code revision 3 for $\mu = 1$	52
35	Comparison of the spectra resulting from revisions 1 and 3 for slab 1-0 geometry	53
36	Comparison of the spectra resulting from revisions 1 and 3 for slab 1-1 geometry	53
37	Comparison of the spectra resulting from revisions 1 and 3 for cylinder geometry	54
38	Visualization of some simulation geometries	54
39	Spectra from <i>CycloSim</i> for slab 1-0 geometry	56
40	Spectra from <i>CycloSim</i> for slab 1-1 geometry	57
41	Spectra from <i>CycloSim</i> for cylinder geometry	57

1 Introduction

1.1 Neutron Stars and Their Magnetic Fields

The lifetime of stars is limited by the amount of matter available for thermonuclear fusion. The radiation produced in that way counters the gravitational pressure and prevents the star from collapsing. Different stages of evolution are passed starting with hydrogen burning up to heavier elements. Finally iron remains which has the largest binding energy per nucleon and therefore no more energy can be gained by nuclear fusion. Goldberg & Scadron (1981) or Kippenhahn & Weigert (1990) discussed this in detail and provide more information about the possible stages. At the end of each stage the radiation declines due to the lack of fusionable matter and the gravitational pressure forces the stellar core to shrink. This process is accompanied by an increase of the plasma temperature enabling the ignition of the next heavier elements. Once iron is reached the star collapses into a supernova leaving a stellar remnant the type of which is mainly determined by the progenitor star's compact core mass remaining after the outer envelopes have been ejected during the supernova. Low mass stars end as white dwarfs while high mass stars form neutron stars or black holes. Chandrasekhar (1931) and Oppenheimer & Volkoff (1939) gave some first theoretical limits for the masses of compact stellar cores. As a rule of thumb stars with mass $\lesssim 1.4 M_\odot$ form white dwarfs, those with masses between $\sim 1.4 M_\odot$ and $\sim 4 M_\odot$ form neutron stars and more massive stars leave a black hole. Woosley et al. (2002) discussed this in detail and approximated the remnant mass of stars with main sequence masses $11 M_\odot - 20 M_\odot$ to be between $1.3 M_\odot$ and $1.6 M_\odot$. Under appropriate circumstances a binary system can form, mostly consisting of a neutron star and a optical companion star. Binary systems emitting X-ray radiation are classified via the mass of the companion star as Low-Mass (LMXB) and High-Mass X-ray Binaries (HMXB). They have one in common which is that they convert gravitational energy into radiation due to efficient accretion of matter from a companion star. But the exact accretion geometry, the accretion rate and its variability differ significantly due to different accretion mechanisms. In binary systems, consisting for example of a stellar remnant and an active star (also called companion star), the mass of the remnant can be determined by measuring relativistic orbital effects. In this way Thorsett & Chakrabarty (1999) estimated the mass of 26 neutron stars within such systems and found an average mass of $1.35 \pm 0.04 M_\odot$. Using the non-relativistic degenerate pressure the mass-radius relation for a neutron star can be estimated by (Meszaros, 1992)

$$R \simeq 4.50 \frac{\hbar^2}{Gm_p^{8/3}} M^{-1/3} \quad (1)$$

where m_p is the proton mass. The resulting radius is $R \sim 12$ km for a typical neutron star mass of $M \simeq 1.4 M_\odot$. Neutron stars are very fast rotating due to the conservation of angular momentum of the progenitor star. Since they possess a magnetic field synchrotron radiation and high energy particles, accelerated by inverse compton scattering, are beamed along the field axis. Taking into account the rotation, this leads to a pulsed emission pattern. If the radiation axis crosses the line of sight the neutron star becomes observable and is called a pulsar.

A rough estimate of the magnitude of the magnetic fields of neutron stars can be made by considering flux conservation during the stellar collapse. Since

$$\Phi = \int \vec{B} \cdot d\vec{l} = \iint \vec{B} \cdot d\vec{A} \sim B \cdot A = \text{constant} \quad (2)$$

where $d\vec{l}$ is a differential of length along a closed path enclosing a bundle of magnetic field lines

\vec{B} , and $d\vec{A}$ is a differential of area directed normal to a surface that is bounded by the integration circuit (Meszaros, 1992). Approximating the surface by an equatorial section $A = \pi R^2$ of the neutron star with normal parallel to the stellar magnetic field of $\sim 10^2$ G results in neutron star fields of $\sim 10^{12}$ G.

Once a neutron star is formed, its magnetic field may decay. Kreykenbohm (2004) summarized some results about these decay processes showing that a decay of the magnetic field of a solitary neutron star takes longer than the neutron star's maximum age. In binary systems, on the other hand, a reduction of the field caused by external influences, as for example accretion flows, becomes possible. The accretion of matter can lead to a spin down of the neutron star's crust whose coupling to the core also influences the magnetic field. Furthermore the neutron star can get heated by the in-falling matter which results in a decrease of the neutron stars conductivity leading to a reduced magnetic field. According to Harding & Lai (2006) who summarized some observational results, strong magnetic fields of the order $\sim 10^{11} - 10^{15}$ G are typically observed for young neutron stars (most radio pulsars, HMXB) while the older ones (millisecond pulsars, LMXB) have weaker fields of the order of $\sim 10^9$ G. If there is an evolutionary connection between them, the corresponding magnetic field reduction takes place on a timescale of 10^9 yr.

1.2 Accretion mechanisms

If the neutron star is in a binary system matter can flow from the normal star onto the neutron star. This process is called accretion. Several accretion mechanisms are possible depending on the parameters of the binary system. They are described in the following together with an example source.

Roche Lobe Overflow: In close binary systems mass can flow from the companion to the neutron star if the companion has filled its Roche lobe which is defined by the inner Lagrange point of the effective gravitational potential. The conservation of angular momentum may lead to the formation of an accretion disk around the neutron star. A example is Her X-1. It is a fast rotating neutron star which is accreting matter through Roche lobe overflow under the formation of an accretion disk. The disk might be twisted due to the precession of the companion star which could explain the 35-day periodicity observed by periodic obscuration of the pulsed X-rays (Petterson, 1975). More recent results including numerical simulations confirm that idea and show that a change of the tilt of such a disk is necessary for an explanation of the observed features (Klochkov et al., 2006). Fragner & Nelson (2010) also showed that such a configuration is expected to induce warping and rigid-body precession of the disc under suitable physical conditions. Caused by tidal torques, the disk is forced to precess in the direction opposite to the orbital motion and its outer parts undergo nutation which is also affected by dynamical action of the accretion streams (Shakura et al., 1999). According to Levine & Jernigan (1982) this effect is at least partly responsible for the turn on of the source near the orbital phases 0.2 and 0.7. The optical companion of Her X-1, HZ Her, has a mass of $M = 2.2M_{\odot}$ making the system a LMXB which is slightly heavier than typical LMXBs. Fig. 1 shows a sketch of the accretion mechanism and a spectrum of Her X-1 obtained during a balloon flight in 1975. It is showing the first cyclotron line ever measured (see below, Section 1.3.5).

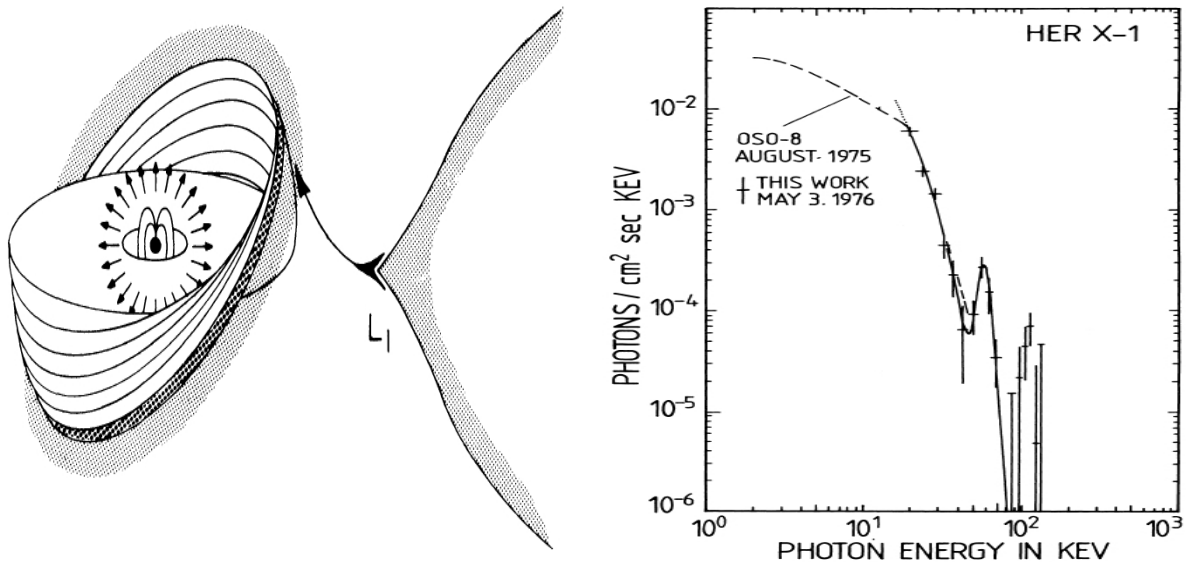


Figure 1: Sketch of a neutron star forming a twisted accretion disk by Roche lobe overflow over the first Lagrange point from (Petterson, 1975) (left) and a deconvolved spectrum of Her X-1 from (Truemper et al., 1978) in which the first cyclotron resonant scattering feature was found (right).

Wind Accretion: If the companion is an OB giant, radiation driven winds might feed the neutron star. An example of a wind accretor is Vela X-1 as an HMXB with an orbital period of ~ 9 days (Barziv et al., 2001) which can be determined easily due to the eclipsing nature of the orbit. It is ~ 2 kpc away (Nagase, 1989) and consists of the B0.5Ib super giant HD77581 with a mass of $\sim 23M_{\odot}$ and a radius of $\sim 30R_{\odot}$ as well as a neutron star with mass of $\sim 1.8M_{\odot}$ and a spin period of ~ 283.5 s (Barziv et al., 2001; Staubert et al., 2004). The neutron star's orbit is within a region of strong stellar winds, because its distance to the companion is very small. This is leading to high accretion rates in the order of $4 \times 10^{-5} \frac{M_{\odot}}{\text{yr}}$ (Nagase et al., 1986). Wind accretion generally does not mean that the accretion rate is constant or that a constant luminosity might be expected: “Vela X-1 shows constant flaring, with some flares reaching fluxes of more than 3.0 Crab between 20-60 keV for several 100 seconds, while the average flux is around 250 mCrab.” (Fürst et al., 2010). The light curve in Fig. 2 shows such flaring activity as measured by Integral/IBIS. One origin of the flaring might be the clumping of the wind as for example described by Liermann et al. (2010).

Be-Accretion: Slightly less than half of the HMXB are believed to be wind accretors (Bildsten et al., 1997) while the others are performing Be-Accretion. Neutron stars on highly elliptical orbits cross regions of increased matter density like the periastron and/or the accretion disk of a donator star. This variability of the accretion flow can cause the neutron star to become unobservable for some time making it a transient source. A large amount of matter is flowing from the companion to the neutron star leading to enormous raise in luminosity within an outburst. In the aphelion on the other hand no matter is available resulting in a quite state. However, an accretion disk around the neutron star is able to sustain the accretion flow for a short time (Kreykenbohm, 2004). 4U 0115+63 is such a object. Its orbital period, according to Rappaport et al. (1978), is ~ 24 d with an eccentricity of $e = 0.34$.

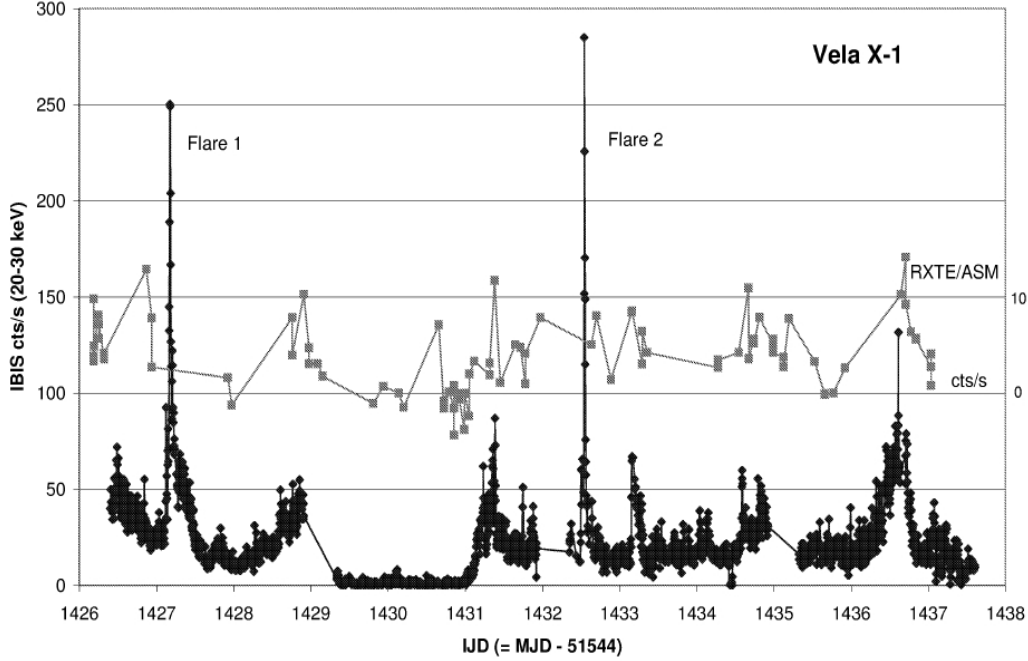


Figure 2: Variations of the X-ray flux of Vela X-1 (Fürst et al., 2010). Two giant outbursts and a smaller one can be seen as well as a quiet state.

1.3 Accretion column

Coming closer to the neutron star an accretion column forms if the magnetic field is sufficiently strong. This behavior has its origin in the interplay between ram pressure and magnetospheric pressure and will be explained in section 1.3.2. Many different shapes have been considered from simple obvious ones like filled cylinders to complex shapes as “spaghetti-like” multiple accretion flows or hollow cylinders. Throughout this thesis the case of filled cylinders with different densities parallel and perpendicular to the field but without any kinds of density gradients are assumed. Since the usage of densities also involves constraints on the dimensions of the accretion column and therefore further parameters it is more convenient to use optical depths instead as described in section 1.3.1. The section ends with a description of the formation, the height, and the temperature of the line forming region which is the region where the magic happens and therefore the starting point for all Monte-Carlo simulations.

Although there are of course also other particles than electrons within the accretion column their influence is not a matter of this thesis. On the contrary electrons are considered to be the only particles within the column. However, proton cyclotron lines will be discussed shortly in Chapter 5 since they provide evidence for ultra-strong magnetic fields in the order $\gtrsim 10^{14}$ G (Zane et al., 2001).

1.3.1 Optical depth

The probability for a photon being scattered before it can escape from the accretion column increases with the column density N_e and the dimensions of the column which leads to deeper absorption lines. These parameters however can be merged to one parameter, the optical depth τ which is a measure of transparency. It is related to the source intensity I_0 and the observed

intensity I by

$$I = I_0 e^{-\tau} \quad (3)$$

All optical depth in this thesis are given in units of the Thomson optical depth τ_T which is related to the column density N_e by

$$N_e = \frac{\tau_T}{\sigma_T} \approx 1.5 \times 10^{24} \tau_T \text{ cm}^{-2} \quad (4)$$

with Thomson cross section

$$\sigma_T = \frac{8\pi}{3} \left(\frac{\alpha \hbar}{m_e c} \right)^2 \approx 6.65 \times 10^{-25} \text{ cm}^2 \quad (5)$$

The amount of matter falling down to the neutron star surface, its magnetic field and the geometry of the accretion column lead to optical depths which are very poorly restricted. In this thesis they are assumed to be of the order of 10^{-4} - 10^{-2} resulting in column densities of about $N_e \sim 10^{21} \text{ cm}^{-2}$ which are about 10 times lower than the ones assumed by Nishimura (2005) or Becker & Wolff (2007). Isenberg et al. (1998) did simulations involving even optical depth up to $\tau \approx 10$ and discussed the effect of different optical depths and magnetic field angles on the line formation process.

1.3.2 Influence of strong magnetic fields

Once the accreted matter gets in the vicinity of strong magnetic fields their effect on the accretion stream has to be taken into account. The surface at which the magnetospheric pressure exceeds the ram pressure of the in-falling matter is called Alfvén surface. The position of the Alfvén surface depends on the accretion geometry and flow. For the case of radial free fall towards a nonrotating star, Lamb et al. (1973) estimated the resulting Alfvén radius to be in the order of $10^5 - 10^6 \text{ m}$ for typical neutron star parameters which corresponds to about 100 neutron star radii. This justifies the assumption of the formation of an accretion column close to the surface and therefore the formation of a hot spot with radius of order

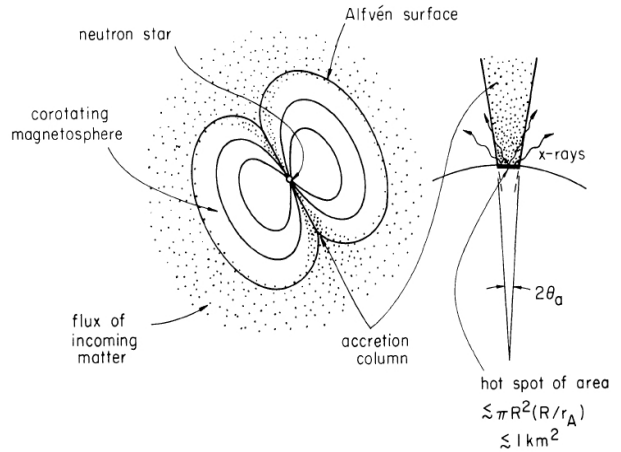


Figure 3: Sketch of an accreting neutron star showing the Alfvén surface and the hot spot formation from Lamb et al. (1973).

$$r_{\text{hot}} = \frac{R^{3/2}}{\sqrt{r_A}} \sim 0.8 \text{ km} \quad (6)$$

for a dipole field (Davidson & Ostriker, 1973). Therefore the magnetic field is responsible for the formation of an accretion column since it forces the particles to hit the neutron star surface at its magnetic poles. In principle also more complex magnetic fields than a dipole field are possible. The effects of those non-dipole fields on the peak energies of cyclotron absorption lines were, for example, investigated by Nishimura (2005) but they are beyond the scope of this thesis. For completeness sake it just should be mentioned that even in the case of only two

magnetic poles they do not necessarily have to be on the same axis. Blum & Kraus (2000), for example, report that for Her X-1 one pole has an offset of $\delta < 5^\circ$ from the antipodal position of the other pole. Thinking about the rotation around another axis, the orbit of the binary system and gravitational light deflection one can see that it is not trivial to draw conclusions about the observers viewing angle to the accretion column which is a very important parameter as we will see in Section 4.

1.3.3 Position of the line forming region

CRSFs are believed to be formed within a small area of the accretion column, the line forming region. For simulations the actual shape of this region can be modeled by simple geometries (see Section 4.1) but information about the height is very important for such simulations since it correlates the measured magnetic field at the height of the line forming region to the surface magnetic field of the neutron star. This has to be taken into account for the interpretation of observational data because the height may change significantly with the accretion rate. This means that spectra taken during the rising edge of an outburst may differ from those taken during the falling edge. By comparing these spectra information about the identities explained in the following can be gained.

The typical mass accretion rate for a neutron star strongly depends on its accretion mechanism and determines whether the accretion column has to be treated as a sub- or super-Eddington luminosity column. The impact of matter on the neutron star surface leads to a hot spot emitting blackbody radiation at a certain temperature T with its intensity within a certain energy range dk given by

$$I(k)dk = \frac{2k^3}{e^{\frac{k}{T}} - 1} dk \quad (7)$$

The temperature depends on the mass accretion rate and the geometry which is determined by the magnetic field, the neutron stars orbit, phase and accretion flow. If the accretion rate increases the blackbody luminosity from the hot spot is expected to increase, too. This holds as long as the luminosity is in the sub-Eddington regime. Once the radiation pressure exceeds the gravitational pressure an equilibrium between both forces the line forming region to stay at a height significantly above the neutron star (super-Eddington regime). Models for such accretion columns have been developed for example by Becker & Wolff (2007) who described the formation of a sonic shock front followed by a thin layer where gas pressure is important (Kirk, 1985), if the overall radiation pressure dominates the gas pressure. That is the case if the X-ray luminosity exceeds the critical luminosity (Becker, 1998)

$$L_{\text{crit}} = \frac{R_*}{r_0} L_E^* = 3.14 \times 10^{37} \left(\frac{M_*}{M_\odot} \right) \left(\frac{r_0}{R_*} \right) \frac{\text{ergs}}{\text{s}} \quad (8)$$

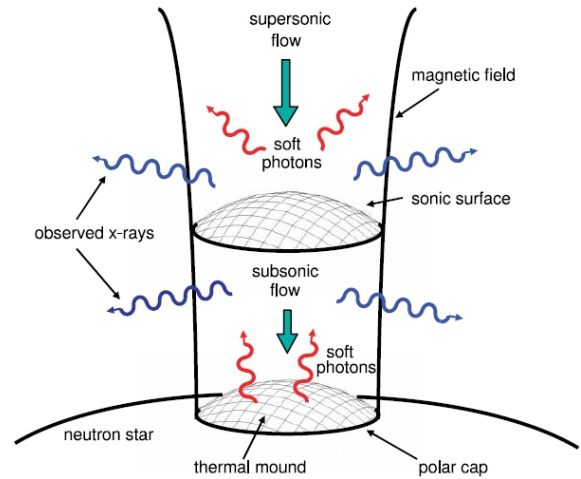


Figure 4: Sketch of an accretion column in the super-Eddington regime (Becker & Wolff, 2005).

with the “scaled” Eddington limit

$$L_{E*} = \frac{\pi r_0^2 L_E}{R_*^2 4\pi} \quad (9)$$

where stellar radius R_* , stellar mass M_* , polar cap radius r_0 and spherical Eddington luminosity

$$L_E = \frac{4\pi G M_* c}{\kappa} \quad (10)$$

with opacity κ . In this super-Eddington regime the line forming region might be high enough above the neutron star that the actually measured magnetic field is lower than the surface magnetic field. Becker (1998) also provided lower boundaries for the height of the sonic point x_* and the height of the shock which corresponds to the coordinate of the stagnation point x_{st} in the sonic point centered coordinate system used

$$\lim_{M_\infty \rightarrow \infty} x_{st} = \frac{r_0}{2\sqrt{3}} \sqrt{\frac{\sigma_\perp}{\sigma_\parallel}} \ln\left(\frac{7}{3}\right) \approx \frac{r_0}{4} \sqrt{\frac{\sigma_\perp}{\sigma_\parallel}} \quad (11)$$

$$\lim_{M_\infty \rightarrow \infty} x_* = \frac{r_0}{2\sqrt{3}} \sqrt{\frac{\sigma_\perp}{\sigma_\parallel}} \ln\left(\frac{7}{6}\right) \approx 0 \quad (12)$$

These boundaries depend on the ratio $\frac{\sigma_\perp}{\sigma_\parallel}$ of the scattering cross sections parallel and perpendicular to the magnetic field for which an approximation is described in the following. The exact cross sections will be derived in the next chapter.

Wang & Frank (1981) considered the case of photons whose propagation and electric vectors are coplanar with the external magnetic field, also referred to as ordinary mode, and perpendicular to each other. This assumption is insofar reasonable for $\omega \ll \omega_B$ as that the electrons act rather like linear antennas in this regime. The corresponding approximate scattering cross section is given by

$$\sigma(\omega, \vartheta, B) \simeq \sigma_T \left(\sin^2 \vartheta + \frac{\omega^2}{\omega_B^2} \right) \quad (13)$$

where ω_B is the classical gyrofrequency (Eq. 24) and ϑ is the angle between the magnetic field axis and the photon’s direction of incidence. This is only appropriate if the photon energy ω obeys $\omega_p \ll \omega \ll \omega_B$ with the the plasma frequency ω_p which, for the case of electrons is given by

$$\omega_p = \sqrt{\frac{4\pi N_e e^2}{m_e}} \quad (14)$$

By introducing a averaged photon energy $\bar{\omega}$ the parallel cross section ($\vartheta = 0$) can now be approximated by

$$\sigma_\parallel(\bar{\omega}, B) \simeq \begin{cases} \sigma_T \left(\frac{\bar{\omega}}{\omega_B}\right)^2 & \text{for } \bar{\omega} \lesssim \omega_B \\ \sigma_T & \text{for } \bar{\omega} \gtrsim \omega_B \end{cases} \quad (15)$$

The corresponding perpendicular cross section is simply given by

$$\sigma_\perp \simeq \sigma_T \quad (16)$$

and is related to the column radius r_0 , the column density N_e and the optical depth τ_\perp by

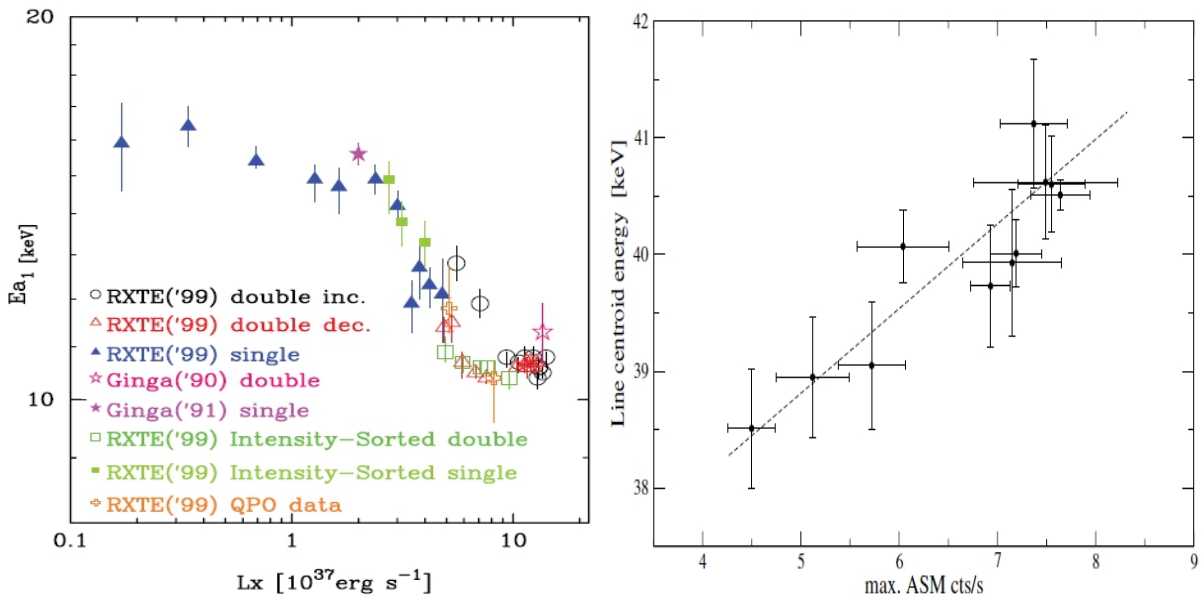


Figure 5: Anticorrelation between the luminosity and the cyclotron energy as observed for 4U 0115+63 (left) by Nakajima et al. (2006) and correlation seen in spectra of Her X-1 (right) by Staubert et al. (2007).

$$\sigma_{\perp} = \frac{\tau_{\perp}}{N_e r_0} \quad (17)$$

Changes of the height of the line forming region due to accretion flow variations will from now on also be referred to as changes of the source's state. Positive (Staubert et al., 2007), negative (Nakajima et al., 2006), or no correlation (Caballero, 2009) between a source's luminosity and its cyclotron line energy have been found. Fig. 5 shows anticorrelation for 4U 0115+63 and correlation for Her X-1. At least for the anticorrelation there is an evident model: If the luminosity raises, the radiation pressure increases pushing the line forming region upwards (Burnard et al., 1991; Nakajima et al., 2006). The local magnetic field therefore decreases attended by a shifting of the cyclotron energy to lower energies.

1.3.4 Temperature and electron momentum distribution

The electrons in the accretion column are assumed to be distributed somehow with respect to their parallel momentum because of a certain plasma temperature which on small time scales is constant due to an equilibrium between cooling and heating processes. One possible cooling scenario is Compton scattering. Riffert (1987) investigated the influence of such Compton cooling on the temperature distribution and presented a numerical solution for the radiative transfer in a finite slab together with a consistent computation of the temperature profile. The model however is appropriate only for low luminosities $\sim 10^{25} \frac{\text{erg}}{\text{cm}^2 \text{s}}$ because it neglects the influence of the radiation on the dynamics of the plasma flow and the cooling perpendicular to the magnetic field which, with respect to hydrodynamical models like for example by Davidson (1973), represents the major cooling contribution.

The electron momenta perpendicular to the magnetic field are quantized as derived in the following Chapter. Quantized means that perpendicular momenta can only be increased or decreased in units of whole momentum quanta. This discretizes the classically continuous set of possible scattering momenta. A thermal momentum distribution therefore only affects the

momenta parallel to the field at least if all electrons can be assumed to be initially in the ground state. This assumption is justified because of the large decay rate compared to the collisional excitation rate (see Section 3.3). The thermal distribution therefore reduces to a one dimensional relativistic distribution of the parallel momenta p which is given by

$$f_e(p)dp = Ne^{-\frac{\sqrt{m^2+p^2}-m}{T}} dp \quad (18)$$

where N is the normalization and T is the temperature in units of MeV. This distribution was also used by Araya & Harding (1999). The parallel temperature has a great impact on the physics discussed in the next two chapters since the electron parallel momenta have to be taken into account for energy and momentum conservation. The frame in which this distribution is symmetric in parity will be used as the lab frame. Some calculations have to be performed in the electron rest frame which is the frame in which the electron parallel momentum vanishes. The electron rest frame is marked by sub-scripting “rf” (x_{rf}). The electrons are falling down to the neutron star surface with very large velocities which are not necessarily constant within the line forming region depending on the state of the source (see Section 1.3.3). That is not yet taken into account by most simulations though it is in principle easily achievable by doing a proper Lorentz transformation similar to those in Eq. 51 and 52.

1.3.5 Measuring a neutron star’s magnetic field

The first cyclotron resonant scattering feature (from now on CRSF or cyclotron line) was found 1977 in spectra of the Her X-1 obtained with a NaI scintillation detector carried by a balloon (Truemper et al., 1978). Up to this point there had been no reliable way for determining the magnetic field of a neutron star. Now that we know about cyclotron resonant scattering features (CRSF) it is even possible to measure them directly. But the question where exactly the magnetic field is measured still remains unanswered. This depends on the accretion geometry and flow as described in Chapter 1.3.3. Nevertheless a rough estimate for the order of the magnetic field can be made quickly by applying the so called $12\text{-}B_{12}$ -rule which gives the cyclotron energy E_{cyc} where the first absorption feature appears in the spectrum at

$$E_{\text{cyc}} \approx 12 \times B_{12} \text{ keV} \quad (19)$$

with B_{12} being the magnetic field in units of 10^{12} G. Gravitational light bending leads to an energy shift with

$$z \approx \frac{1}{\sqrt{1 - \frac{2GM}{Rc^2}}} - 1 \approx 0.3 \quad (20)$$

for typical neutron star masses resulting in

$$E_{\text{cyc}} \approx \frac{1}{1+z} \times 11.6 \times B_{12} \text{ keV} \quad (21)$$

with a more precise proportional constant. For a detailed analysis the complete formula (eq. 42) which also takes the angle dependence into account should be used together with the gravitational redshift factor $\frac{1}{1+z}$ if information about the viewing angle is available. For converting the cyclotron line centroid energies to magnetic fields, $z = 0.3$ is assumed (see Section 1.3.5) throughout this thesis.

Source	E_{cyc} (keV)	P_{puls} (s)	P_{orb} (d)	companion	discovery
Swift J1626.6–5156	10	15	132.9	Be	RXTE (deCesar, '09)
4U 0115+63	14, 24, 36, 48, 62	3.6	24.31	Be	HEAO-1 (Wheaton, '79) RXTE, SAX (Heindl '99, Sant.,'99)
4U 1907+09	18, 38	438	8.38	B2 III–IV	SAX (Cusumano, '98)
4U 1538–52	22, 47	530	3.73	B0I	Ginga (Clark,'90), RXTE (Rodes-Roca, '09)
Vela X-1	24, 52	283	8.96	B0.5Ib	Mir-HEXE (Kendziorra, '92), RXTE (Kreykenbohm, '02)
V0332+53	27, 51, 74	4.37	34.25	Be	Ginga (Makishima, '90)
Cep X-4	28	66.25	>23	B1	Ginga (Mihara, '91)
Cen X-3	29	4.8	2.09	O6.5II	SAX (Santangelo, '98) RXTE (Heindl, '98)
X Per	29	837	250.3	B0 III–Ve	RXTE (Coburn, '01)
MXB 0656–072	33	160	100?	O9.7Ve	RXTE (Heindl, '03)
XTE J1946+274	36	15.8	169.2	B0-1V-IVe	RXTE (Heindl, '01)
4U 1626–67	37	7.66	0.028	WD?	SAX (Orlandini, '98) RXTE (Heindl, '98)
GX 301–2	37	690	41.5	B1.2Ia	Ginga (Mihara, '95)
Her X-1	41	1.24	1.7	A9-B	Ballou-HEXE (Trümper, '78)
A0535+26	50, 110	105	110.58	Be	HEXE (Kendziorra, '92, '94), CGRO (Maisack, '97)
1A1118–61	55	408	400-800 d?	O9.5IV-Ve	RXTE (Doroshenko, '10)
GRO J1008–57	88?	93.5	247.8	B1–B2	CGRO (Shrader, '99)

Figure 6: Table from Wilms et al. (2010) listing sources with cyclotron lines

Currently there are 17 sources known having at least one cyclotron line (Wilms et al., 2010) with 4U 0115+63 being the one with the highest number of harmonics, four according to Santangelo et al. (1999) or Heindl et al. (1999), seen in the spectra. Fig. 6 lists them with their cyclotron energies, pulse periods, and orbital periods. In the following some results about cyclotron lines in the spectra of the example sources described in Section 1.2 are presented.

Her X-1: Gruber et al. (2001) showed that the cyclotron line centroid energy is at 41 keV which would correspond to a magnetic field of $\sim 4.6 \times 10^{12}$ G close to the neutron star surface. They also state that this energy increased by 23% from originally 34 keV some time between 1991 and 1993 indicating a change change of the height of the region where the cyclotron line is produced (see Section 1.3.3). Enoto et al. (2008) however recently found the cyclotron line to be at ~ 36 keV and detected a second line at ~ 73 keV in the pulse phase-resolved spectra at the descending edge of the main peak.

Vela X-1: Kreykenbohm et al. (2002) found two cyclotron lines in data obtained from the Rossi X-ray Timing Explorer (RXTE) satellite which were later confirmed by Schanne et al. (2007) at slightly higher energies of ~ 27 keV and ~ 54 keV. The corresponding magnetic field is approximately 3×10^{12} G.

4U 0115+63: This source is the record holder regarding the number CRSF found with a total number of four features seen in the spectra of an outburst observed in 1999 by BeppoSAX (Fig. 7) at energies (12.74, 24.16, 35.74, 49.5 keV) (Santangelo et al., 1999). This makes it the ideal source for the study of line ratios and their evolution during an outburst. Santangelo et al. (1999) found the ratios 1:(1.9):(2.8):(3.9) between the centroid energies with respect to the first feature. So the lines are almost equally spaced but a variation of those ratios is expected if the viewing angle changes since the relativistic energy shifting depends on the angle. The energy of the fundamental line indicates a magnetic field of $\sim 1.4 \times 10^{12}$ G. Originally one absorption line was found at an energy of 20.1 ± 0.5 keV (Wheaton et al., 1979). This line was probably the first harmonic instead of the fundamental line and therefore the magnetic field was overestimated.

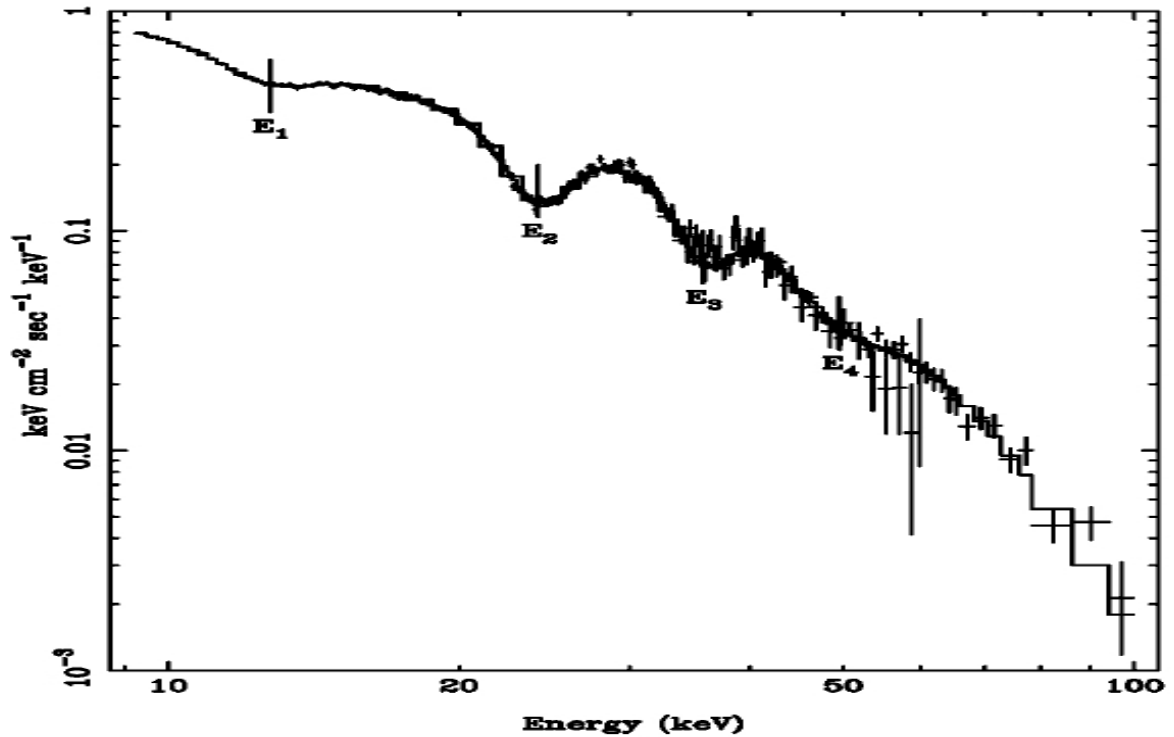


Figure 7: Unfolded spectrum of the descending edge of an outburst of 4U 0115+63 (Santangelo et al., 1999). Four CRSF can be seen with the fundamental line being less deep than the first harmonic.

1.4 Structure of this thesis

The possible scenarios of accretion mechanisms are described in Section 1.2 on the example of three corresponding sources.

In the case of a accreting binary system with a strong magnetic field, the accretion flow is funneled along the magnetic field lines forming an accretion column in which influent particles interact with internally produced photons. Therefore the photons which escaped from the column reveal information about the physical parameters and processes within the column. Many processes are theoretically imaginable to contribute to the emergent spectra as, for example, pair production and annihilation, Möller and Bhabah scattering, or trident production, just to mention a few of them (see Sina (1996) for detailed derivations of them with respect to strong magnetic fields). Dominating in this regime are, however, cyclotron emission and absorption, and compton scattering. Their influence on the spectra of accreting neutron stars is investigated in this thesis.

Section 1.3.3 gives an introduction about the dynamics of the line forming region. A recent model of the accretion column from Becker & Wolff (2007) is utilized to explain the principle of correlations between the height of the line forming region and the luminosity of a neutron star. Section 1.3.4 describes the connection between the plasma temperature and the electron momenta within the column. The Chapter ends listing sources exhibiting cyclotron resonant scattering features (CRSFs).

The characteristics of the physics of electrons in such accretion columns and their interactions with photons in the vicinity of strong magnetic fields are explored in Chapter 2. Many physical parameters are involved in the formation of cyclotron lines and some equations can not be solved analytically. Therefore numerical simulations have been applied to the problem by

many authors. Rafael Araya wrote a program, from now on called MC code (with “MC” referring to the Monte-Carlo nature of the simulation), which is able to propagate photons through a suitable plasma and bins the resulting emergent photons with respect to their angle and energy. A version of this program revised by Schönherr (2007) was the starting point for the numerical simulations done in course of this thesis. Chapter 3 focuses on the evaluation of parameters required for Monte-Carlo simulations of neutron star spectra like the mean free path of a photon or the initial momentum of an interacting electron. Corresponding numerical results from own calculations are discussed and the methods were utilized to develop software for suitable calculation of the important parameters, and simulation of the processes leading to the cyclotron resonant scattering features (CRSF) which are the observational evidence for interactions taking place in strong magnetic fields. Chapter 4 gives an overview over approaches to simulate spectra with CRSFs and explains the Monte-Carlo simulation written by R. Araya and the modifications made as part of this thesis. Furthermore a completely new Monte-Carlo code is introduced together with the major computational methods used in there. Simulated spectra from both codes are shown and different revisions of the Araya code are compared in terms of the sampled parameters and how they affect the spectra. Finally some prospects for future research are given which would not be possible without new simulation codes like the one provided by the author.

2 Electrons in strong magnetic fields

This Chapter gives a short introduction to the physics of electrons in magnetic fields and their interaction with photons. The basic principle of their partly quantized nature is introduced in the beginning and is essential for the understanding of the possible interactions with photons described afterwards. CGS units are used like in almost all of the references given in this thesis.

2.1 Classical treatment

Classically a moving charge in a magnetic field is affected by the Lorentz force which forces it to change its trajectory into a helix. In the following only the most important equations are mentioned following Canuto & Ventura (1977). The equation of motion for a particle with mass m and charge q in a external homogeneous magnetic field B is given by

$$m \frac{dv}{dt} = \frac{q}{c} v \times B \quad (22)$$

The trajectory of the electron results in a helix ($v_{\parallel} \neq 0$) or a circle ($v_{\parallel} = 0$) with Lamor radius

$$R = \frac{v_{\perp}}{\omega} = \frac{v_{\perp} m c}{e B} \quad (23)$$

in the plane perpendicular to the magnetic field. For relativistic electrons the Lamor frequency ω should be transformed:

$$\omega_B = \frac{e B}{m c} \rightarrow \frac{e B c}{E} \quad (24)$$

with energy

$$E = \frac{m c^2}{\sqrt{1 - \beta^2}} = \sqrt{m^2 c^4 + p^2 c^2} \quad (25)$$

The classical treatment can be seen as valid as long as the Lamor radius is significantly smaller than the de Broglie wavelength of the electron $\lambda_B = \frac{\hbar}{m v}$ which implies a boundary on the magnetic field:

$$B \ll \frac{m^2 c^3}{e \hbar} \left(\frac{v}{c} \right)^2 \quad (26)$$

This motivates the introduction of a unit of magnetic fields, the critical magnetic field:

$$B_{\text{crit}} = \frac{m^2 c^3}{e \hbar} = 4.414 \times 10^{13} \text{ G} = 4.414 \times 10^9 \text{ T} \quad (27)$$

“which is precisely the field for which the cyclotron energy is equal to the electron rest energy” (Sina, 1996). From now on magnetic fields are given in units of this critical magnetic field B_{crit} if not indicated otherwise.

2.2 Quantum mechanical treatment

Once the magnetic field is comparable to the critical magnetic field the usage of classical mechanics is not justified anymore and quantum mechanical calculations have to be performed. The corresponding notation and methods are described in the following. Natural units are used which means that the magnetic field is given in units of the critical field B_{crit} as described above and $c = \hbar = 1$.

2.2.1 Non-relativistic

Ignoring relativistic effects the energy E of an electron with wave functions Ψ occupying Landau level n is given by the eigenvalues of the Hamiltonian H for an electron in a magnetic field B . Starting from the stationary Schrödinger equation

$$H\Psi = \left(\frac{1}{2m} (p - eA)^2 - \mu B + e\Phi \right) \Psi = E\Psi \quad (28)$$

the form of a harmonic oscillator with frequency $\omega_B = \frac{eB}{mc}$ arises with energy solutions

$$E_n = \left(n + \frac{1}{2} + \sigma \right) \hbar\omega_B + \frac{p_z^2}{2m} \quad (29)$$

where $\sigma = \pm\frac{1}{2}$ as, for example, shown by Schönherr (2007).

2.2.2 Relativistic

For a complete relativistic quantum mechanical treatment the Dirac equation has to be solved for the Hamiltonian

$$H = \alpha\pi + \beta m \quad (30)$$

with the electron mass m , the generalized momentum operator $\pi = p + A$ and

$$\alpha_j = \begin{bmatrix} 0 & \sigma_j \\ \sigma_j & 0 \end{bmatrix} \quad (31)$$

$$\beta = \begin{bmatrix} I & 0 \\ 0 & -I \end{bmatrix} \quad (32)$$

where σ_j are the Pauli matrices ($j = 1, 2, 3$) and $A = \frac{1}{2}B \times r$ is the vector potential of the magnetic field B .

The corresponding energy eigenvalues of an electron in Landau level n with parallel momentum p as derived by Rabi (1928) are

$$E_n = \sqrt{m^2 + p^2 + 2nB} \quad (33)$$

Special attention has to be paid to the eigenfunctions which must be an eigenstate of a spin operator for which different versions are given in literature. The one given by Johnson & Lippmann (1949) does not have physical significance, does not reflect any symmetry between electron and positron, does not commute with the radiative correction to the Hamiltonian and can not be Lorentz transformed in an appropriate way (Sina, 1996; Graziani, 1992). For that reasons the magnetic momentum operator

$$M = \frac{eB}{2m^2} \begin{pmatrix} \varepsilon & 0 & -p_z & 0 \\ 0 & -\varepsilon & 0 & -p_z \\ p_z & 0 & -\varepsilon & 0 \\ 0 & p_z & 0 & -\varepsilon \end{pmatrix} \quad (34)$$

constructed by Sokolov et al. (1968) should be used instead, because it fulfills all the requirements mentioned above. The corresponding electron wave functions were also derived by Sina (1996).

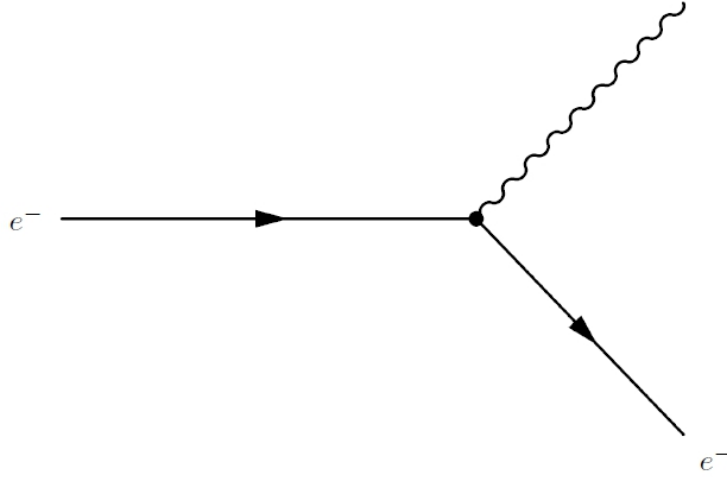


Figure 8: Feynman diagram for cyclotron emission.

2.3 Cyclotron resonant scattering features

The microphysical processes which lead to CRSFs shall be investigated in the following. This includes cyclotron emission, absorption, and scattering. One will see that exact calculations are rather complicated especially for the scattering case and it is very important to keep in mind that the physics is only quantized perpendicular to the field. Nevertheless the separation of the problem has to be performed fully relativistic since simulations show significant deviations to non-relativistic calculations (see Chapter 4).

2.3.1 Cyclotron emission

Cyclotron emission is the radiation of energy due to an deexcitement of an electron from one Landau level to a lower one. An electron in an excited state has a finite lifetime given by the total decay rate from this state to any possible final state. Fig. 8 shows the Feynman graph for cyclotron emission with the corresponding scattering matrix element being

$$S_{fi} = ie \int d^4x \bar{\psi} \gamma_\mu A^\mu \psi \quad (35)$$

with the electron wave function ψ and the photon wave functions A^μ . After integration over time and space the total decay rate results from taking the absolute square of the scattering matrix and integrating over all possible final states:

$$\Gamma = \int \frac{|S_{fi}|^2}{T} \frac{L dp_f}{2\pi} \frac{L da_f}{2\pi\lambda^2} \frac{L^3 d^3k}{(2\pi)^3} \quad (36)$$

where a_f is the x-coordinate of the final electron's orbit center and integration time T is canceling out because it also appears in the absolute square of the matrix element $|S_{fi}|^2$ for which an explicit form is given by (Sina, 1996).

The integration over $\mu = \cos \vartheta$ in the calculation of $|S_{fi}|^2$ has to be done numerically (Herold et al., 1982) and will also be used to sample the angle of the emitted photon. The energy of a photon emitted in a decay process $n_i \rightarrow n_f$ is determined by the conservation of energy and momentum parallel to the field

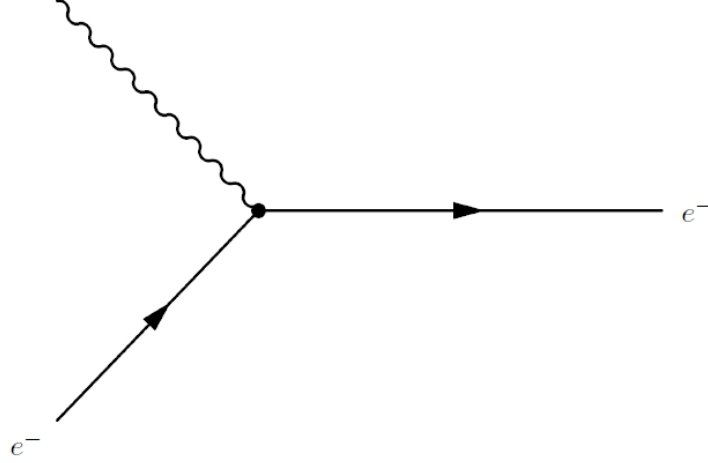


Figure 9: Feynman diagram for cyclotron absorption.

$$p_f = p_i - \omega \cos \vartheta \quad (37)$$

$$E_f = E_i - \omega \quad (38)$$

and by making use of the electron energy E_n from above (Eq. 33) results in

$$\omega_n = \frac{(E_i - p_i \cos \vartheta) - \sqrt{(E_i - p_i \cos \vartheta)^2 - 2mB \sin^2 \vartheta (n_i - n_f)}}{\sin^2 \vartheta} \quad (39)$$

2.3.2 Absorption cross section

From above considerations one can readily write down the resonance condition for cyclotron absorption exciting the electron to Landau level n . It results from the same conservation equations as for emission just with a plus instead of a minus between the right side terms:

$$p_f = p_i + \omega \cos \vartheta \quad (40)$$

$$E_f = E_i + \omega \quad (41)$$

This leads to the resonant energy

$$\omega_n = \frac{1 - \sqrt{1 + 2nB \sin^2 \vartheta}}{\sin^2 \vartheta} m \quad (42)$$

in the electron rest frame where $p_{\parallel} = 0$. The conservation laws, however, can have two, one, or zero solutions for p which, according to Daugherty & Ventura (1978), have to satisfy the equation

$$\sqrt{p^2 + m^2} = p \cos \vartheta + nB \frac{m^2}{\omega} - \frac{\omega}{2} \sin^2 \vartheta \quad (43)$$

which in the case of one solution determines the cutoff energy

$$\omega_{\text{cut}}(n) = \frac{\sqrt{1 + 2nB} - 1}{\sin \vartheta} m \quad (44)$$

above which the condition can not be fulfilled anymore and absorption is suppressed. It is worthwhile to mention that this implies that the largest possible range of p values appears at this energy for small μ . This maximizes the phase space for cross sections averaged over a momentum distribution and therefore leads to photon mean free paths being minimal at the cutoff energy rather than at the resonant energy.

The square of the scattering matrix for cyclotron absorption whose Feynman diagram is shown in Fig. 9 is the same as for cyclotron emission as required by the principle of detailed balance (Sina, 1996). The relation to the cross section is given by

$$\sigma_{\text{abs}} = \int \frac{L^3}{1 - \beta_i \cos \vartheta_i} \frac{|S_{fi}|^2}{T} \frac{L dp_f}{2\pi} \frac{L da_f}{2\pi \lambda^2} \quad (45)$$

with a_f and T as described above.

The rest frame cross section for the absorption of a photon of energy k and angle ϑ by an electron initially in the ground state $n = 0$ with spin $s_i = -1$ as derived by Daugherty & Ventura (1978) but in the electron rest frame was given by Harding & Daugherty (1991). After summation over final spin states and averaging over photon polarization it reads

$$\sigma_{\text{abs}}^n(\vartheta) = \frac{\alpha \pi^2 \hbar^2 c^2}{E_n} \delta(E_n - m - \omega) \frac{e^{-Z} Z^{n-1}}{(n-1)!} \left[(1 + \cos^2 \vartheta) + \frac{Z}{n} \sin^2 \vartheta \right] \quad (46)$$

with $Z = \frac{\omega^2 \sin^2 \vartheta}{2mB}$. These authors also stated that the classical cross section results from above in the limit $nB \ll 1$ in which case $\omega \approx nB$, $Z \ll 1$ and $E_n \approx m$.

The resulting state has a finite lifetime which is given by its decay rate. This introduces an energy uncertainty resulting from the Heisenberg relation for time and energy

$$\Delta E \Delta t \geq \hbar \quad (47)$$

The usual way of dealing with those natural line widths is replacing the δ -function by a Lorentzian

$$L_{n,s}(\omega) = \frac{\Gamma_{n,s}}{2\pi \left[(\omega - \omega_n)^2 + \frac{\Gamma_{n,s}^2}{4} \right]} \quad (48)$$

where $\Gamma_{n,s}$ is the decay rate from Landau level n with spin s .

2.3.3 Scattering cross section

The calculation of the scattering cross section is more complicated than the calculation of the absorption cross section since it involves the summation over real and virtual intermediate states and one has to take into account both possible Feynman diagrams (Fig. 10). Expressions for the non-relativistic (Canuto et al., 1971; Ventura, 1979) as well as for the relativistic case (Herold, 1979; Melrose & Parle, 1983; Daugherty & Harding, 1986; Sina, 1996) have been derived by many authors with the latter ones differing mainly in the choice of the electron wave function, the coordinate system, and the final Landau states taken into account. The most commonly used wave functions are the ones from Johnson & Lippmann (1949) being somewhat simpler and the ones from Sokolov et al. (1968) which should be preferred (see 2.2.2).

The complete expression for the cross sections derived by making use of the Johnson-Lippmann wave functions was given by Harding & Daugherty (1991) where, as pointed out

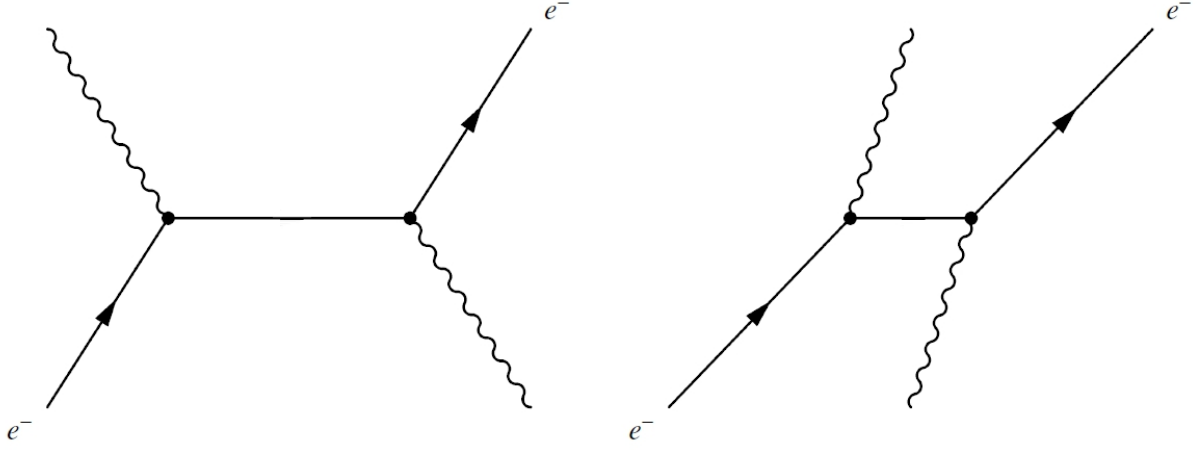


Figure 10: Second order Feynman diagrams for cyclotron scattering. The electron can either first absorb an incoming photon and emit a final photon afterwards, or it first emits the final photon and then the incoming photon gets absorbed.

by Nobili et al. (2008b), due to a typo, in equations (A1)-(A5) all terms $N\epsilon\epsilon'\Lambda_n\Lambda_n$ have to be replaced by $N^2\epsilon\epsilon'\Lambda_n\Lambda_n$. For spin and polarization dependent treatment the equations given by Sina, who is using the Sokolov-Ternov wave functions, should be used. Harding and Daugherty also compared the scattering cross sections with the ones for absorption and found out that they agree quite well within the resonances. Furthermore they derived an approximation for the resonant part of the scattering cross section by normalizing a Lorentz profile with respect to absorption at $\omega = \omega_n$:

$$\sigma_{\text{scat}} \simeq A_n \frac{\frac{E_n^2 \Gamma_n}{2\pi m^2}}{\left(\omega + \frac{\omega^2 \sin^2 \vartheta}{2m} - nBm\right)^2 + \left(\frac{E_n \Gamma_n}{2m}\right)^2} \quad (49)$$

In this thesis functions provided by Ramin Sina which use the formulas described in his dissertation (Sina, 1996) were used because they were also used in the original MC code and seem to be most suitable if one wants to be able to evaluate cross sections also for higher transitions $n' > 2$ and take into account polarization effects. The total Compton scattering cross sections for a photon traveling through a plasma with magnetic field $B = 0.05$ perpendicular to the direction of motion, summed over final states $n' = 0, 1, 2, 3, 4$ with $n' = 0$ representing the continuum part and averaged over polarization modes is seen for different propagation angles to the magnetic field in Fig. 11.

The shifting of the resonant energies and its proportionality to $1 - \mu^2 = \sin^2 \vartheta$ according to Eq. 42 can be seen as well as the reduced width of the higher harmonics for very small angles to the field. Bearing in mind the momentum distribution of the photons it is worth to take a look at the momentum dependency of the cross sections as shown in Fig. 12. Perpendicular momentum components can only be transferred as multiples of the perpendicular momentum quanta $p_{\perp} = 2nB$ leading to a singular behavior. Therefore μ was set to numerically practical values.

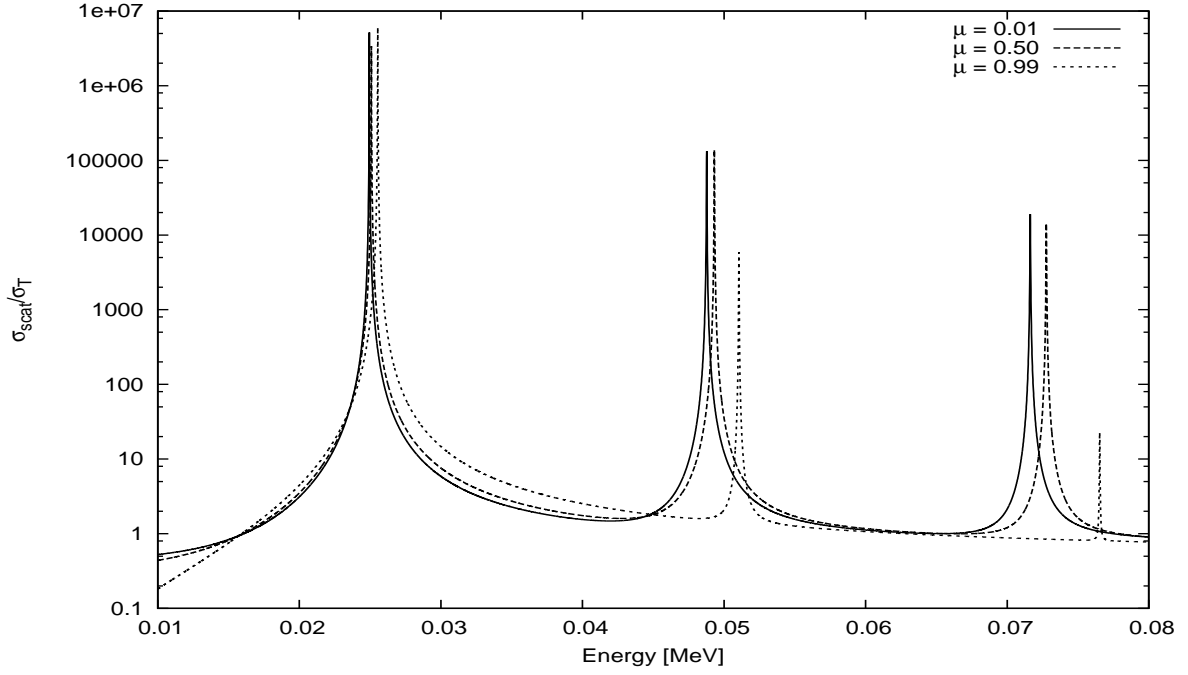


Figure 11: Compton scattering cross sections within a magnetic field of $B = 0.05$ for different angles of the incoming photon $\mu = \cos \vartheta$. While the first peaks agree well for different μ the others are shifted in energy due to strong influence of the $\sin^2 \vartheta$ dependence of the cyclotron energy ω_n especially for higher Landau level $n > 1$.

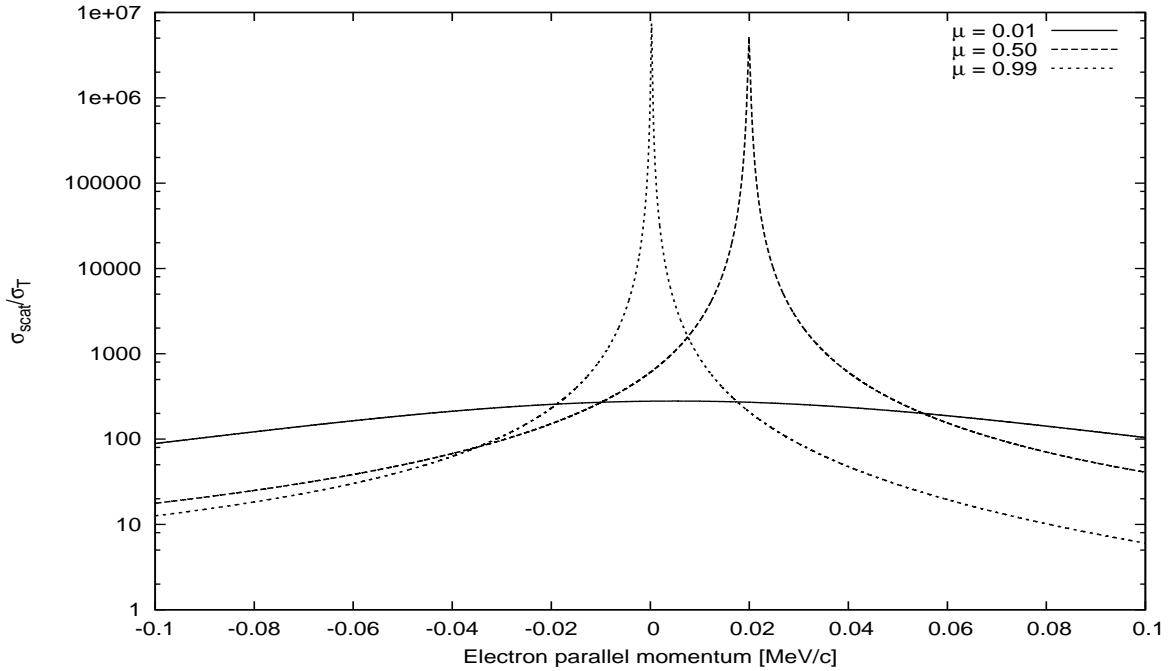


Figure 12: Scattering cross section with respect to the electron parallel momentum for incoming photons with energy $k \approx \omega_1$. In the case of photons perpendicular to the magnetic field ($\mu = 0$) the cross sections are nearly equal because of the conservation of momentum parallel to the field which enables the photon to transfer its momentum to the electron. Since the momentum perpendicular to the field is quantized the cross sections are peaking at $p \approx 0$ for photons parallel to the field ($\mu = 1$).

3 A photon's history

In this Chapter the way of a photon is traced from the injection into the plasma until it escapes from the accretion column. Methods for proper sampling of the intermediate and final parameters are presented as well as particular results explaining the major mechanisms within the line forming region. The figures and tables have been created by a selfwritten program called *accp*, described in more detail in Chapter 4 which also gives a more detailed description of the corresponding numerical methods. The order and methods roughly follow the photon's history presented by Araya & Harding (1999) and can be seen as the basis of the first MC code written by Rafael Araya which also uses the sampling methods described here.

Solving problems with many variables numerically is very time consuming. Often it is more efficient to solve, for example, radiation transfer equations by propagating many photons through a medium by taking proper micro physics into account and afterwards collecting and binning the emergent photons for drawing conclusions on the macroscopic parameters. This way of solving numerical problems is called a Monte-Carlo method. An illustrative example is the estimation of the area of a circle by sampling randomly distributed points within a boundary square whose dimensions are equal to the circle diameter. By counting the points within the circle and relating them to the outer points one can draw conclusions on the area of the circle since the area of the square is well known. Sampling in the context of Monte-Carlo simulations means choosing a parameter value from a corresponding distribution in a random but statistical appropriate way ensuring that the parameter distribution function results in the limit of an infinite number of sampling processes. The simplest example would be a coin flip simulation. In principle it is possible to sample "heads" ten times in a row but taking into account a million sampling processes the distribution function (which basically consists of the values 0.5 and 1.0 in this case) should be retrievable.

Fig. 13 shows a flow chart of all sampling processes involved in Monte-Carlo simulations of cyclotron lines. First of all a photon originating from a photon source within the column is injected. Possible photon sources are the blackbody hot spot at the surface, bremsstrahlung from electrons being abruptly decelerated by the surface or a sonic shock front, or synchrotron radiation within the column. In simulations, like in the old MC code or in the *CycloSim* code introduced later, often a heuristic approach is chosen like using a powerlaw with optional high energy or Fermi-Dirac cut off (see Chapter 4 for realization dependent details about energy and

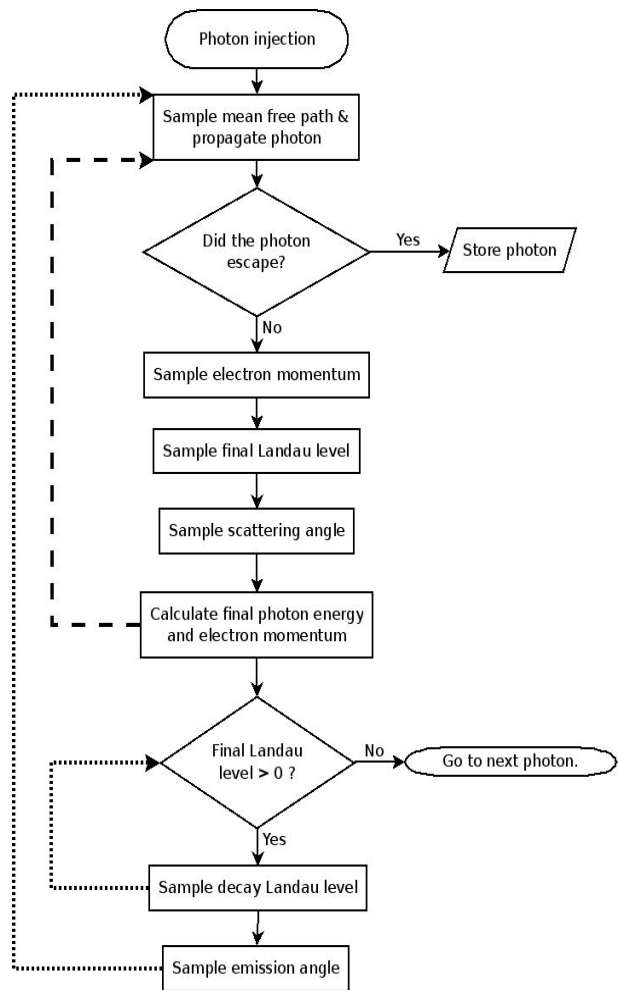


Figure 13: Flow chart of a Monte-Carlo process propagating photons through a CRSF medium.

angular sampling of the input photons). Once a photon is injected its sampled travel path determines whether it stays in the line forming region or can escape. Escaping photons are stored and binned for the production of output spectra. If the photon's travel path is smaller than the optical depth seen by that photon in that direction it gets scattered off or absorbed by an electron whose parallel momentum and final Landau level has to be sampled with the final Landau level being the energy level to which the electron gets excited by the scattering or absorption process. Then the scattering angle has to be sampled by making use of the differential scattering cross sections. At this point all information required for the calculation of the photon's final energy and the electrons final momentum has been gathered and the corresponding calculations can be performed. The scattered photon (dashed line) can now be further propagated. The electron can now create a new photon by a process called photon spawning if it got excited into a Landau level above the ground state. The Landau level to which the electron deexcites has to be sampled by comparing the decay rates to the possible final states and determines the spawned photon's (dotted line) energy. The angle of this cyclotron emission process also depends on the corresponding differential decay rates and has to be sampled too before the spawned photon can be further propagated. Conclusively the number of photons is not conserved and if the final Landau level after the spawning process is still above the ground state the spawning process repeats iteratively. Each step will now be discussed in detail together with some corresponding results from the program I wrote.

3.1 Mean free path and profile functions

The mean free path of a photon within the accretion column depends on several variables. First of all the reason for the presence of CRSFs is the resonant behavior of the absorption/scattering cross sections at certain resonant energies (Eq. 42). Energy k and angle ϑ of the incident photon transformed to the electron rest frame decide whether the resonance condition is met or not. This transformation results in a broadening of the range of resonant energies due to the momentum distribution of the electrons $f_e(p)$ (Eq. 18). Taking into account this momentum distribution the mean free path of a photon with energy k and $\mu = \cos \vartheta$ is given by

$$\lambda(k, \mu) = \frac{1}{\langle \sigma(k, \mu) \rangle_{f_e}} \quad (50)$$

with $\langle \sigma(k, \mu) \rangle_{f_e}$ being the total compton scattering cross section averaged over the momentum distribution, which will also be referred to as profile function. Since the calculation of the scattering cross section will be done in the electron rest frame the photon energy and angle have to be transformed to the rest frame by

$$k \rightarrow k_{\text{rf}} = \gamma(1 - \beta\mu)k \quad (51)$$

$$\mu \rightarrow \mu_{\text{rf}} = \frac{\mu - \beta}{1 - \beta\mu} \quad (52)$$

with

$$\gamma = \sqrt{1 + \frac{p^2}{m^2}} \quad (53)$$

$$\beta = \gamma^{-1} \frac{p}{m} \quad (54)$$

Then the resulting rest frame cross sections $\sigma_{\text{rf}}(k_{\text{rf}}, \mu_{\text{rf}})$ have to be transformed back to the lab frame which leads to the following expression for the profile function:

$$\langle \sigma(k, \mu) \rangle_{f_e} = \int_{-\infty}^{\infty} dp f_e(p) (1 - \mu\beta) \sigma_{\text{rf}}(k_{\text{rf}}, \mu_{\text{rf}}) \quad (55)$$

The distance $\delta\tau$ the photon actually travels before scattering takes place can be sampled by assigning a random number Rn to the normalized primitive of its probability

$$W(x \rightarrow x + \delta\tau) = e^{-\frac{\delta\tau}{\lambda(k, \mu)}} \quad (56)$$

which results in

$$\delta\tau = -\lambda(k, \mu) \ln(\text{Rn}) \quad (57)$$

The calculation of the profile functions is computationally expensive since it involves an integration over the electron momentum parallel to the magnetic field and an integration over all photon final angles μ_f for getting the total cross section. Both integrations need to be done numerically. Especially for small μ the cross sections and therefore the profile functions are sharply peaked within the resonances and need a sensitive numerical integration. On the other hand for most combinations of μ and k much less sampling points are required. For that reason an adaptive mechanism was developed using an adaptive Simpson scheme for integration and storing interim results and the total profile because the interim results are required in the following for the sampling of the electron's parallel momentum. Fig. 14 shows the profile functions (inverse mean free paths) for different angles to the magnetic field. They perfectly agree with those from Harding & Daugherty (1991) as seen in Fig. 26. An adaptive grid refinement in energy and angle was utilized for the production of interpolation tables with a reliable approximation for the maximum error. This speeds up simulations and is described in detail in Section 4.5.3.

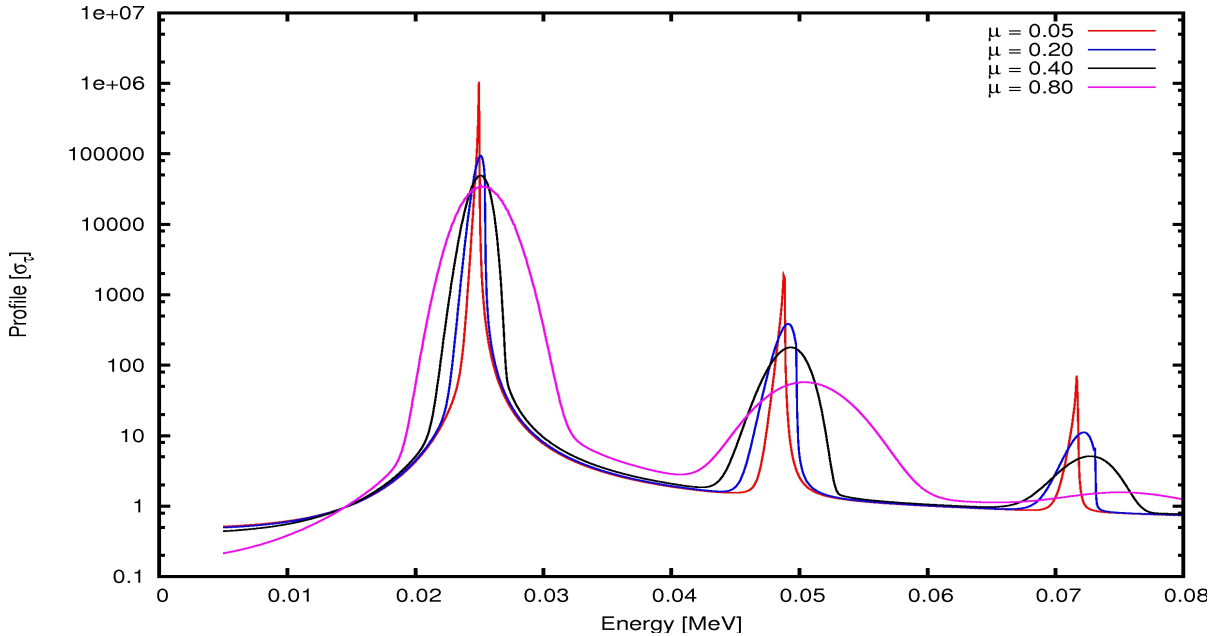


Figure 14: Compton scattering cross sections averaged over a relativistic thermal momentum distribution for different $\mu = \cos \vartheta$ (from highest value within the resonances to the lowest: $\mu = 0.05, 0.2, 0.4, 0.8$). The so called profiles have been calculated and are reproducible by the *accp* program.

3.2 Electron momentum

After translating the photon by the sampled travel path it scatters off an electron whose momentum has to be sampled first. Since the mean free path was evaluated by using the cross section averaged over the momentum distribution, the sampling of the momentum of the electron being the scattering partner has to be done by taking into account the same properties. The momentum sampling was in principle done in the same way as by Araya & Harding (1999) regarding the theory of the sampling process though the numerical methods rather differ. These differences will be discussed below.

The electrons momentum was sampled by assigning a random number $Rn \in [0 : 1]$ to the partial integral of the probability for a photon to scatter off an electron with momentum p which is the integrand in Eq. 55 normalized to the total profile:

$$Rn \rightarrow N \int_{-\infty}^p dp' f_e(p')(1 - \mu\beta)\sigma_{\text{rf}}(k_{\text{rf}}, \mu_{\text{rf}}) \quad (58)$$

with $N = \frac{1}{\langle \sigma(k, \mu) \rangle_{f_e}}$ and $-\infty$ numerically set to -5 MeV which provides an even larger range of momenta than the value of $45T$ used by Araya & Harding up to a temperature of 500 keV , which is far out of the energy range of interest here.

3.3 Initial and final Landau level

Strictly speaking the considerations above already presumed an important assumption which is that the electrons are initially in the ground level. This assumption will now be justified before the sampling of the final Landau level is discussed. Like above $n = 0$ is the ground level and $n = 1$ is the first excited state. The energy difference between those states is responsible for the position of the fundamental line. The inelastic collisions of electrons with each other may excite an electron to a Landau level higher than the ground state. An order of magnitude estimate for the rate of electrons being excited from the ground level to the first excited state was given by Bonazzola et al. (1979):

$$\Gamma_{\text{col}} \sim 6.2 \cdot 10^8 \frac{n_{21}}{B_{12}} \text{ s}^{-1} \approx 2.1 \times 10^{-14} \frac{\tau_T}{B} \text{ cm}^{-2} \text{ s}^{-1} \quad (59)$$

This process can therefore be ruled out as a mechanism for keeping the higher Landau level populated because of the much higher decay rates in the regime of interest which are of the order of

$$\Gamma \sim \tau_0^{-1} \frac{2}{3} B^2 \approx 0.38 \times 10^{19} B^2 \text{ s}^{-1} \quad (60)$$

in the sub-critical field limit (Eq. 69 with $n = 1$). The decay rate is significantly larger than the collisional rate for low optical depths $\tau \sim 10^{-3}$. This means that the electrons can be assumed to be all in the ground state $n = 0$.

For the sampling of the final Landau level two methods were tested during the development of the *CycloSim* program both resulting in similar Landau level sampling. The first and more convenient method is the comparison of the profile functions of scattering into Landau level $n' = 0, 1, 2, \dots$ with the total profile summed over all possible final states. A set of example ratios for a magnetic field of $B = 0.05$ and a temperature $T = 3 \text{ keV}$ for photons perpendicular and parallel to the field are given in Fig. 15. The corresponding values are also shown in tables 1 and 2.

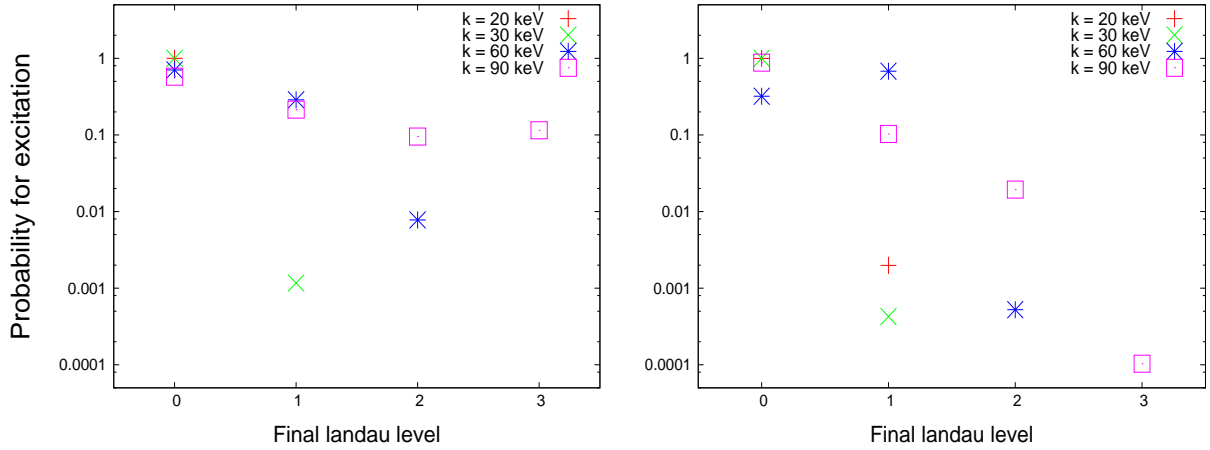


Figure 15: Probability of an excitation of an electron to final Landau level n_f caused by a photon with energy k propagated perpendicular (left) or parallel (right) to the magnetic field $B = 0.05$.

Table 1: Probabilities for electron excitement for the parameters given in the text and photons perpendicular to the magnetic field.

Final Landau level	$k_{\perp} = 20$ keV	$k_{\perp} = 30$ keV	$k_{\perp} = 60$ keV	$k_{\perp} = 90$ keV
0	1.000×10^0	9.988×10^{-1}	7.049×10^{-1}	5.757×10^{-1}
1	0	1.167×10^{-3}	2.873×10^{-1}	2.140×10^{-1}
2	0	0	7.778×10^{-3}	9.509×10^{-2}
3	0	0	0	4.246×10^{-5}

Table 2: Same as table 1 but for the case of photons parallel to the magnetic field.

Final Landau level	$k_{\parallel} = 20$ keV	$k_{\parallel} = 30$ keV	$k_{\parallel} = 60$ keV	$k_{\parallel} = 90$ keV
0	9.980×10^{-1}	9.996×10^{-1}	3.202×10^{-1}	8.776×10^{-1}
1	1.981×10^{-3}	4.262×10^{-4}	6.793×10^{-1}	1.030×10^{-1}
2	0	0	5.240×10^{-4}	1.933×10^{-2}
3	0	0	0	1.032×10^{-4}

The second method is the one used in the old MC code which basically does the same but with the compton scattering cross sections instead of the profile functions. The differences appeared to be roughly 2% with the cross section method leading to even lower probability for excitation to higher Landau level.

3.4 Scattering angle

The compton scattering cross sections are strongly dependent on the angle. Therefore the final angle to the field μ_f under which the photon will be emitted after the scattering process has to be sampled carefully. This was done by assigning a random number to the normalized cumulative angle distribution function of the scattering cross section this time for a certain already sampled electron momentum p parallel to the field:

$$Rn \rightarrow \frac{\int_{-1}^{\mu_f} \frac{d\sigma_{\text{scat}}(k, \mu', p)}{d\mu'} d\mu'}{\int_{-1}^1 \frac{d\sigma_{\text{scat}}(k, \mu', p)}{d\mu'} d\mu'} \quad (61)$$

3.5 Kinematics

If the electron momentum p , the final Landau level n_f , the scattering angle μ_f and energy k and the angle μ of the incoming photon are sampled, the final photon energy k_f and electron momentum p_f can be determined by the conservation of energy and momentum parallel to the field

$$k + E_{n_i} = k_f + E_{n_f} \quad (62)$$

$$k\mu + p = k_f\mu_f + p_f \quad (63)$$

with electron energy E_n as given in Eq. 33. Only momenta parallel to the field are conserved because of the inelastic nature of excitations of perpendicular momentum quanta $p_{\perp} = 2(n_f - n_i)B$. The equations yield a quadratic equation for the final photon energy k_f :

$$k_f = \frac{-b \pm \sqrt{b^2 - 4ac}}{2a} \quad (64)$$

with coefficients

$$a = \sin^2 \vartheta_f \quad (65)$$

$$b = -2 \left(k(1 - \mu\mu_f) - p\mu_f + m \sqrt{1 + 2n_f B + \frac{p^2}{m^2}} \right) \quad (66)$$

$$c = k^2 \sin^2 \vartheta + 2m^2(n_f - n_i)B - 2k\mu p + 2mkE_{n_i} \quad (67)$$

Only the solution with the minus sign in front of the root is physically meaningful which can be seen in the limiting case of $n_i = n_f$, $\vartheta_i = \vartheta_f = \frac{\pi}{2}$ and $p = 0$ where $k_f = k$ (Sina, 1996). The final electron momentum can now be evaluated according to Eq. 62:

$$p_f = p + k\mu - k_f\mu_f \quad (68)$$

3.6 Photon spawning

The spawning process and its relation to the decay rates as well as the decay rates themselves are described in the following.

3.6.1 The spawning process

Photon spawning is the deexcitation of electrons from the excited Landau population ($n > 0$) to a lower Landau level ($n' < n$) by the emission of a photon with the corresponding resonant energy in the electron rest frame. The resonant energy is shifted because of relativistic effects due to the motion of the electrons parallel to the magnetic field. The electrons tend to undergo a transition to the Landau level $n' = n - 1$ which can be seen by comparing the decay rates to all possible final states (see Section 3.6.3).

The energy of the spawned photon is almost identical to the resonant absorption energy ω_{res} . Similarly to what is done with the scattering cross sections for the scattering photon, the angular distribution of the spawned photon is sampled by using normalized decay rate profiles which are stored during integration in a cumulative way. Since the spawned photon's energy varies only slightly around the resonant energy its mean free path is low compared to that of continuum photons. Nevertheless it is possible that a first harmonic, which appears to be deeper than the fundamental line in observations, may result from filling the fundamental line with spawned photons from excited states.

3.6.2 Decay rates

The relativistic decay rates have been derived in various papers (Sokolov et al., 1968; Herold et al., 1982; Latal, 1986). Since there will be missions in the future which will be able to derive information about the polarization of the measured photons, the usage of Sokolov-Ternov wave functions was the most relevant argument for using the decay rates derived by Herold et al. They are in principle the same ones as the ones derived by Sokolov and Ternov themselves, but in Cartesian instead of cylindrical coordinates. Another strong argument for the use of the decay rates based on the Sokolov-Ternov electron wave functions was pointed out and proved by Graziani (1992): “[...] the decay rates obey the expected time dilation scaling relation $\Gamma_{\text{lab}} = \gamma^{-1}\Gamma_{\text{rf}}$ if the states of Herold et al. or Sokolov & Ternov are chosen, but they do not if the states of Johnson & Lippmann are used.”

Latal (1986) derived some useful analytical expressions to approximate the decay rates of transitions to the ground state in the vicinity of sub- and super-critical fields

$$nB \ll 1 \quad : \quad \Gamma^{n \rightarrow 0} \approx t_0^{-1} (2n^2)^n \frac{(n+1)!}{(2n+1)!} B^{n+1} \quad (69)$$

$$nB \gg 1 \quad : \quad \Gamma^{n \rightarrow 0} \approx 0.41 \times t_0^{-1} \sqrt{\frac{B}{n}} \quad (70)$$

as well as between neighboring levels

$$\Gamma^{n \rightarrow n-1} \approx t_0^{-1} \frac{2}{3} (2n-1) B^2 (1+2nB)^{-\frac{3}{2}} \quad (71)$$

with $t_0 = \frac{\hbar}{\alpha mc^2} \approx 1.765 \cdot 10^{-19}$ s being the characteristic time .

In this thesis, the decay rates from Herold et al. will be used which are valid over the entire range of the input parameters, are defined for any possible transition, obey the simple time

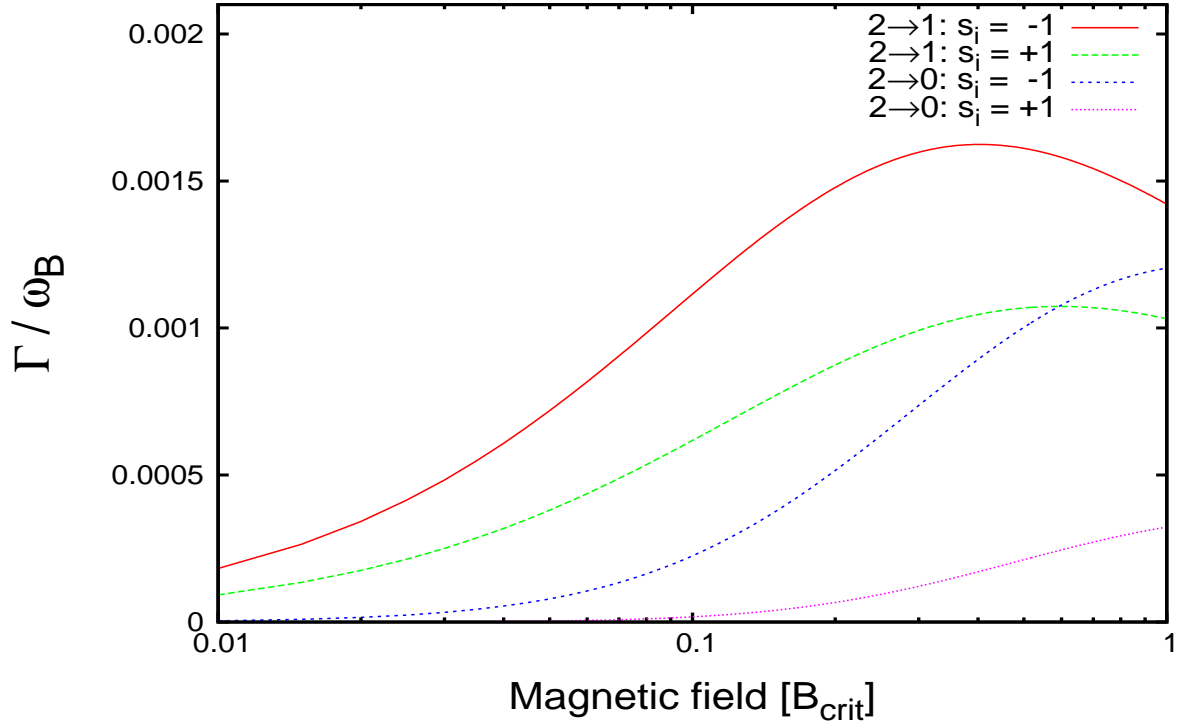


Figure 16: The decay rates of transitions of electrons initially in Landau level $n_i = 2$ to final landau level $n = 0, 1$ for initial spins $s_i = \pm 1$ in units of the cyclotron energy ω_B .

dilation mentioned above, and can be evaluated separately for both polarization states of the emitted photon providing the possibility for polarization state sampling of the spawned photon. See Section 2.3.3 for further information about possible basis states.

Fig. 16 shows the total decay rate of an electron initially occupying the second Landau level with respect to the magnetic field. The rates of an electron with negative spin are larger than those for an electron with positive spin especially for transitions to the ground state where only negative final spin is allowed. The decay rate and therefore the probability for deexcitation to Landau level $n_f = 1$ is larger than for a direct transition to the ground state.

Fig. 17 shows the decay rates for a deexcitation of an electron initially in the first Landau level with the solid line being the decay rate for $s_i = -1$ and the dashed line representing the spin flip case $s_i = 1 \rightarrow s_f = -1$. All decay rates are given in units of the cyclotron energy $\omega_B = mB$.

The angle of the spawned photon has to be sampled too since the decay rates differ for different emission angles. Fig. 18 shows the differential decay rates for emission within a certain angle to the field. The angular dependence increases with the magnetic field strength and angles with $|\mu| \approx 1$ are clearly preferred for large B . For electrons with a parallel momentum the decay rates have to be transformed to the lab frame and that breaks the $\mu = 0$ symmetry which is seen in the electron rest frame. The sampling can be done in the same way as for the final scattering angle but with the decay rates instead of the scattering cross sections.

3.6.3 Branching ratios and consequences

Similarly to the case of the sampling of the final Landau level of the electron immediately after the scattering process, the Landau level to which the electron deexcites to has to be sampled, too. This can be done by comparing the decay rates to the different possible final states. Looking

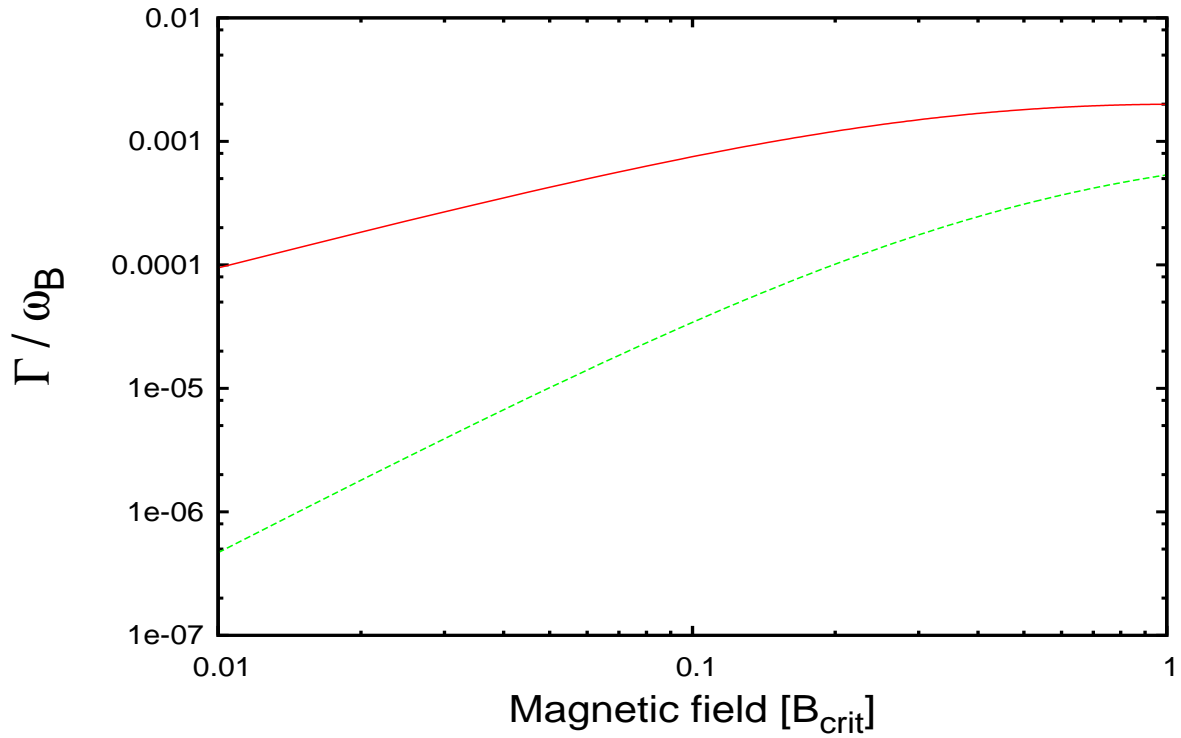


Figure 17: Decay rates for transitions from Landau level $n_i = 1$ for initial spins -1 (solid line) and $+1$ (dashed line). Since only $s_f = -1$ is allowed in the ground state a no spin flip transition is performed in the case of negative initial spin and a spin flip transition is the only possibility for positive initial spin.

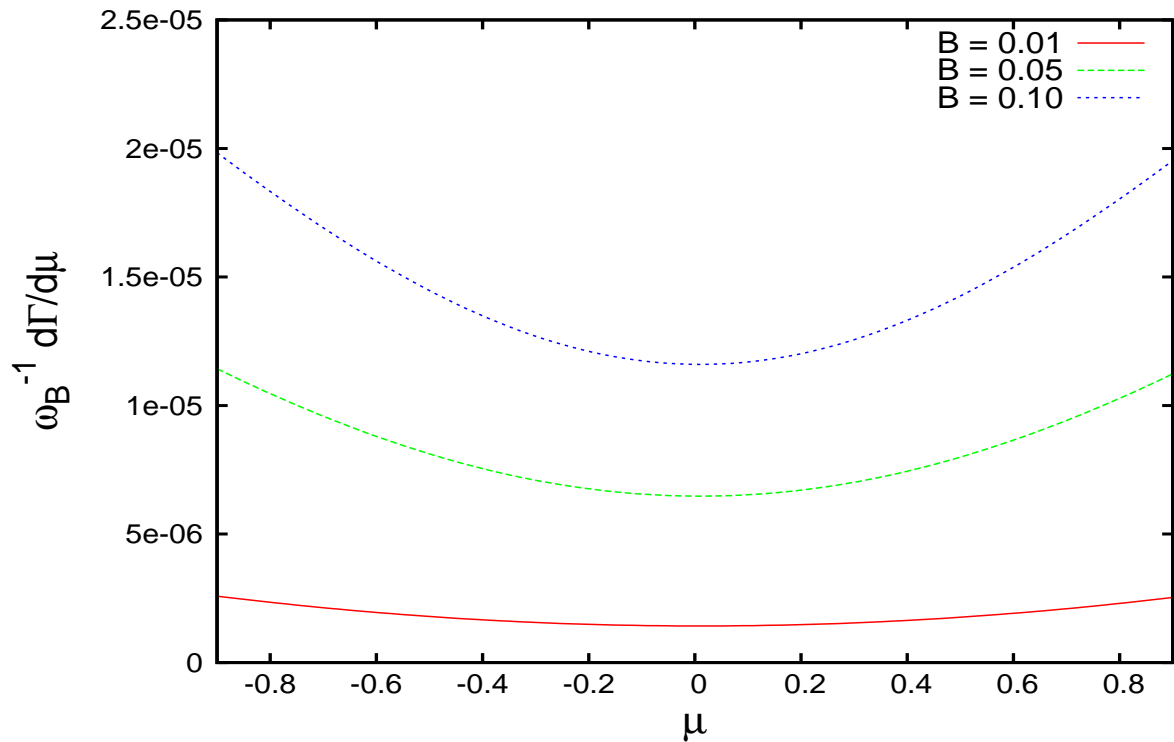


Figure 18: Differential decay rates of an electron in landau level $n_i = 1$ with initial spin $s_i = -1$.

Table 3: The probabilities for the decay from Landau level n_i to a lower level n_f are shown for positive and negative initial electron spins s_i .

Final Landau level	$n_i = 4, s_i = -1$	$n_i = 4, s_i = +1$	$n_i = 3, s_i = -1$	$n_i = 3, s_i = +1$
0	6.385×10^{-3}	6.783×10^{-4}	2.084×10^{-2}	2.005×10^{-3}
1	4.442×10^{-2}	1.838×10^{-2}	1.571×10^{-1}	9.153×10^{-2}
2	1.921×10^{-1}	1.445×10^{-1}	8.221×10^{-1}	9.065×10^{-1}
3	7.571×10^{-1}	8.364×10^{-1}	0	0

at table 3 it can clearly be seen that most of the electrons perform a transition to the next lower Landau level. This is extremely important for the understanding of the line depth of the fundamental line because electrons undergoing transitions from higher Landau levels are spawning photons having the right energy for filling up the fundamental absorption line. The contribution of this effect to the observable spectra strongly depends on the optical depth of the line forming region. A further interesting fact is, that for negative initial spin the decay rate to the ground state is by an order of magnitude larger which is caused by the suppression of spin flip transitions (Herold, 1979).

4 Simulation of CRSF

In this Chapter the properties of the different stages of code revisions of the Monte-Carlo simulation code by Rafael Araya are described as well as the numerical and computational methods I developed and implemented in this code. Those methods were also used for the new simulation code, *CycloSim*, which I wrote during this thesis. The results of the later versions are compared for different geometries which are slab 1-1, slab 1-0, and cylinder geometry and will be described in Section 4.1 followed by some mostly heuristic continuum spectra used for the sampling of the seed photon energies in Section 4.2. An overview over previous simulation approaches by various authors and how they differ from each other is given in Section 4.3 before the old MC code and the new *CycloSim* code will be introduced in detail.

4.1 Model geometries

In this Section the geometries used by Araya and also by other authors are explained. The most common ones are slab 1-0, slab 1-1, and cylinder geometry. The notation of the slabs is representing the ratios of the column densities seen by a photon in the opposite escape direction (Freeman et al., 1999; Schönherr, 2007). A slab 1-0 geometry may be assumed in the case of sub critical luminosity where a hot spot at the neutron star surface is emitting photons upwards and absorbing back-scattered photons reaching the surface. In a slab 1-1 geometry the photons are emitted between two identical slabs by a source plane above the neutron star surface like it is assumed to be the case in a radiation dominated plasma which is building a shock front. Photons can only escape a slab through the bottom or the top. The opposite is the case for cylinder geometry which can be seen as a cylinder of infinite length (instead of infinite radius in the case of slabs) and a certain optical depth perpendicular to the magnetic field which the photons have to overcome before they can escape through the cylinder wall.

4.2 Model continua and photon injection

For being able to simulate absorption lines there have to be seed photons that can be absorbed. Those input photons can be injected in various ways. A blackbody hot spot at the neutron star, for example, can be simplified by a surface parallel source plane emitting photons in all upward directions. A similar source plane can be assumed for photons produced by blackbody radiation or bremsstrahlung within a thin shock front above the surface with the difference that the photons may also be injected towards the surface. Both variants are used by the MC code from Araya for slab 1-0 and slab 1-1 geometry respectively. Bremsstrahlung or synchrotron radiation may also lead to continuous emission through the accretion column with the photon's origin not being limited to a source plane. In this case other models have to be applied like a line-like source in the center of the column. In the MC code the seed photons for cylinder geometry are inserted from such a seed photon line which is positioned parallel to the magnetic field in the middle of the cylinder.

In the old as well as in the new MC code mostly heuristic input spectra are utilized though a physical meaningful blackbody has also been tested in the *CycloSim* program. Four different spectral types of seed spectra are listed in the following together with the energy dependencies of their intensities $I(k)$ at a certain energy k :

- Blackbody source

$$I(k) \propto \frac{k^3}{e^{\frac{k}{T}} - 1} \quad (72)$$

- Powerlaw

$$I(k) \propto k^{-\alpha} \quad (73)$$

- Powerlaw with exponential energy cut off

$$I(k) \propto k^{-\alpha} e^{-\frac{k}{E_{\text{fold}}}} \quad (74)$$

- Powerlaw with Fermi-Dirac cut off

$$I(k) \propto \frac{k^{-\alpha}}{e^{\frac{k-E_{\text{cut}}}{E_{\text{fold}}}} + 1} \quad (75)$$

where α denotes the photon index, E_{cut} the cut off energy, and E_{fold} the folding energy. All of them are implemented in the *CycloSim* code. If not indicated otherwise, spectra produced by the old MC code are using a Fermi-Dirac cut off powerlaw input spectrum with $E_{\text{fold}} = 10$ keV and $E_{\text{cut}} = 12$ keV.

4.3 Numerical approaches

Simulations were done by a variety of authors using similar programs with other restrictions or approximations, but there are also completely different approaches to the problem like, for example, by Nishimura (2005) who is using Feautrier methods to construct such spectra. From the group of Monte-Carlo simulations Isenberg et al. (1998) performed simulations for different magnetic field angles with respect to the plane-parallel slab through which the photons are propagated as well as for a extremely large range of optical depth $8 \times 10^{-4} \leq \tau \leq 10$. Other recent simulations were done by Nobili et al. (2008a) who started with a Monte-Carlo code neglecting relativistic contributions by using non-relativistic approximations and described relativistic corrections in a second paper (Nobili et al., 2008b) with the result, that relativistic corrections regarding the angular redistribution become significant already below a magnetic field of $B = 0.1$. They also restricted themselves to transitions involving only intermediate states $n \leq 2$ and therefore final Landau states $n = 0, 1$. Such simplifications may be appropriate in the low field regime, but with increasing field strength the influence of the higher Landau level has to be taken into account because the probability for an excitation of an electron to such higher levels raises at higher fields. Such high fields are definitely expected for some accreting neutron stars as for example indicated by observational results for A 0535+26 (Kretschmar et al., 2005). It is highly desirable to have a Monte-Carlo code which is capable of proper simulation for all sources and therefore includes this higher transitions as well as relativistic effects, as the MC code does.

4.4 MC code: 1st revision

For investigating the processes within the accretion column Rafael Araya wrote a program which propagates photons through a slab 1-1 geometry, being illuminated from a source plane within the slab, or a cylinder geometry in which photons are injected from the cylinder axis and can only escape through the cylinder wall. A thermal momentum distribution was assumed for the electron momenta parallel to the field. In her dissertation (2005-2007) Gabriele Schönherr added new functionality to the code and refined the internal grids according to the improved

situation in terms of computational power compared to the 1990ies. She also developed a XSPEC model, called *cyclomc*, for its direct comparison to observational data using precalculated Green's function tables which can be used to generate output spectra for arbitrary energy dependencies of the input photons by folding the response of the injection of monoenergetic photons with the desired input spectrum.

4.4.1 Aims: First comparison of the MC model with observational data

The main goal of the first revision of the MC code by Schönherr et al. was to achieve the first quantitative comparison of a theoretical model for cyclotron lines to observational data. For that reason extensive MC simulations were performed on a large multidimensional parameter grid. For a better understanding of the shape of the accretion column a new geometry was added: The Slab 1-0 geometry or bottom illuminated slab. A new Green's functions approach was implemented in order to yield independence from the shape of the spectral continuum. This makes it possible to use different phenomenological continua and test which one works better without having to do the same calculations over and over again. Also, first analytical solutions for the continua were evolving by the time of this first revision (Becker & Wolff, 2007). The first physical XSPEC model for cyclotron lines was implemented working as a convolution and interpolation model on a given continuum spectrum. FITS tables of the Green's functions were calculated for all input energy bins as well as for all three geometries and the model was applied to observations. In order to obtain more detailed spectra the energy grid was refined from 160 to 640 bins while the number of angular bins was doubled from 4 to 8.

4.4.2 Restrictions

A new geometry (slab 1-0 geometry) was added to the original code but further flexibility, like magnetic field or velocity gradients, can only be added qualitatively by application of multiple convolution mechanisms making use of the Green's functions approach. (Schönherr, 2007)

Cylinder and slab geometry are quite rough approximations to the actual shape of the accretion column. In reality the geometry will obviously have elements of both or even of all three types being more similar to one or the other depending on the optical depths seen by a photon looking into the different directions inside the column. Another aspect which has to be investigated in detail is the injection angle of the photon. In the MC code there are several possibilities for that like mono-angular injection, relativistically beamed injection or isotropic injection which is used for all spectra produced here and also for the calculation of the Greens function tables. Isotropic in the context of the MC code means sampling the angle by assigning a random number to its cosine.

4.4.3 Results

Slab 1-0 geometry not only causes the least emission wings but shows also the best fit for first comparisons to data. The lines are in general too pronounced. A possible way to explain this is partial covering, however the more probable explanation is that gradients smear out the theoretical lines in the observed spectra. Such gradients shall be implemented as future work.

Fig. 19 shows simulated spectra resulting from an slab 1-1 and a cylinder geometry with optical depths of 3×10^{-4} and 3×10^{-3} for an magnetic field of $B = 0.05$ at different viewing angles. The second absorption feature is significantly deeper than the first one which agrees with observational results.

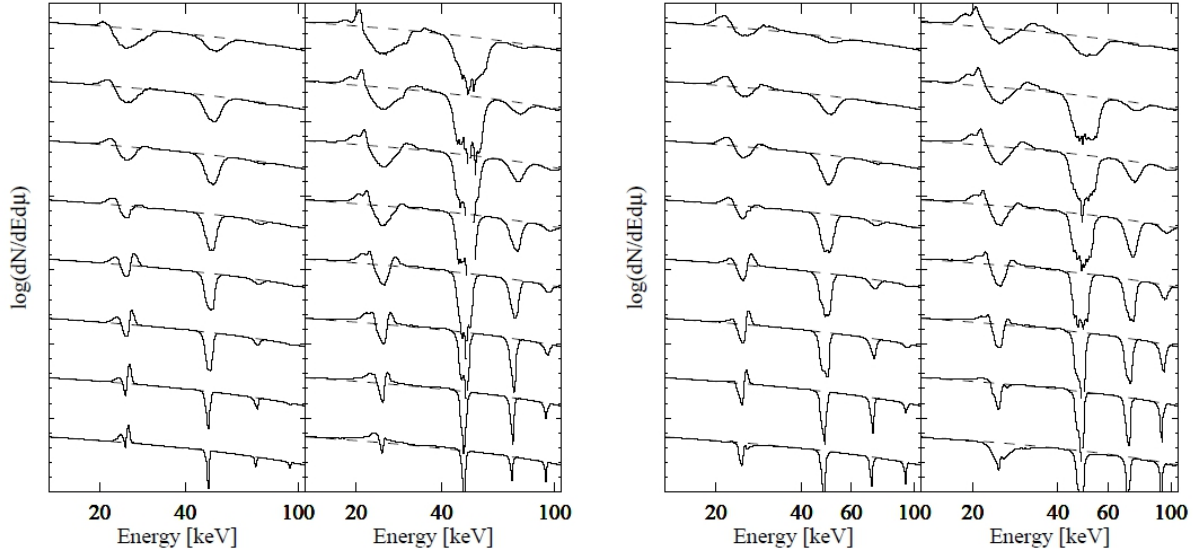


Figure 19: Simulated spectra for the first revision of the MC code from Schönherr et al. (2007) for cylinder geometry (left diagram) and for slab 1-1 geometry (right diagram). In each diagram a optical depth of 3×10^{-4} is shown on the left side and a optical depth of 3×10^{-3} on the right side.

The code was modified to store all sampled mean free paths as well as all sampled electron momenta together with the photon energy and angle at which they appeared. After inversion, binning and averaging some graphs were generated showing the sampled identities (Fig. 20).

4.5 MC code: 2nd revision

From later comparisons of the MC code with the Feautrier approach of O. Nishimura (ISSI international team 2006-2008), and from comparisons to older work from Harding & Daugherty (1991) and Isenberg et al. (1998), G. Schönherr found that the profiles used in the MC code are wrong by a factor of nearly 2 (G. Schönherr, priv. com). This leads to much lower mean free paths and therefore a large number of scatterings for each photon. Fixing this problem is of course crucial for further quantitative modeling of observational data. The XSPEC model was

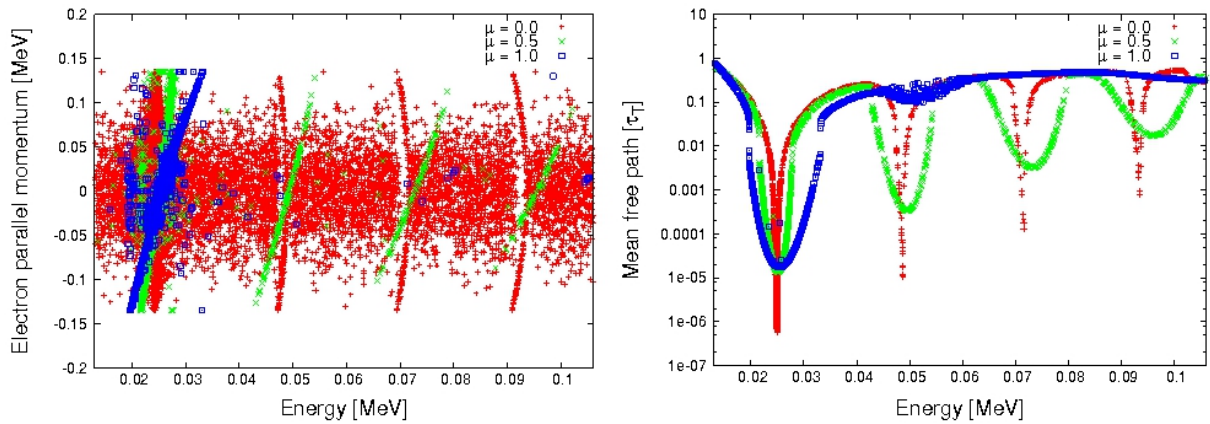


Figure 20: Sampled electron momenta (left) and mean free paths (right) for revision 1. The magnetic field strength is $B = 0.05$ and the temperature is $T = 3 \text{ keV}$.

therefore not published for the scientific community so far and interpretation of the data was only done for parameters which are not affected by this problem. The implementation of a new correct calculation of the profiles was therefore the first major challenge of the work done in this thesis. The computational methods presented below were used to create profile tables which were then accessed by the MC code to interpolate the actual profiles. Because of this interpolation from precalculated tables the time consumption massively decreased from about 10 hours down to 6 hours for a standard input spectrum.

4.5.1 Aims: Revision of the means free path sampling

A new set of functions integrating the scattering cross sections numerically should be developed and compared to the profiles given in literature. After they are verified to agree with the profiles from Harding & Daugherty (1991) which seem to be seen as the right ones by all authors they shall be integrated in the old MC code replacing the wrong mean free path sampling. In the following Section this development is discussed in detail starting with the numerical integration method and ending with a comparison of the resulting Monte Carlo spectra.

4.5.2 Numerical methods: Adaptive Simpson integration

An adaptive Simpson method (McKeeman, 1962) was used for numerical integration. The choice of this method over other ones like Romberg or Gaussian integration was made because of the need for adaptive grid refinement. Integration with the Simpson method generally means approximating the area under a curve by the area of a quadratic function defined by three points on this curve. Since this is only exact for third order polynomials three grid points are normally not enough for functions which have to be integrated numerically. By splitting the integration interval $[a, b]$ in smaller parts one can nevertheless achieve a good approximation for the integral depending on the number of grid points. This can be done by dividing the interval in N smaller ones all with the same width $w_i = \frac{b-a}{N}$ which is also called composite Simpson method or by splitting them adaptively depending on some convergence criterion.

The cross sections are sharply peaked for some electron momenta which depend on the energy and angle of the incoming photon. The integration method has to be sensitive enough for taking the peaks into account but should also stop splitting the intervals early enough for not wasting computing time on trivial parts of the cross section. A common criterion is the following one which is based on an error approximation for the Simpson rule:

$$\frac{|S(a, c) + S(c, b) - S(a, b)|}{15} < \epsilon \quad (76)$$

where $S(x, y)$ denotes the integral from x to y approximated by the Simpson rule (Abramowitz & Stegun, 1964)

$$S(x, y) = \int_x^y f(z) dz = \frac{y-x}{6} \left(f(x) + 4f\left(\frac{x+y}{2}\right) + f(y) \right) - \frac{(y-x)^5}{2880} f^{(4)}(\xi) \quad (77)$$

and c is the midpoint of the interval $[a, b]$ which is split into two intervals with equal width. The interval splitting and integral evaluation is done in a recursive way allowing the storage of the partial integrals for an increasing integration variable in the right order.

4.5.3 Numerical methods: Adaptive grid refinement

Because of the sharply peaked nature of the cross sections for small μ within the resonances and at the relativistic energy cutoffs (Eq. 44) a much larger number of grid points is required in

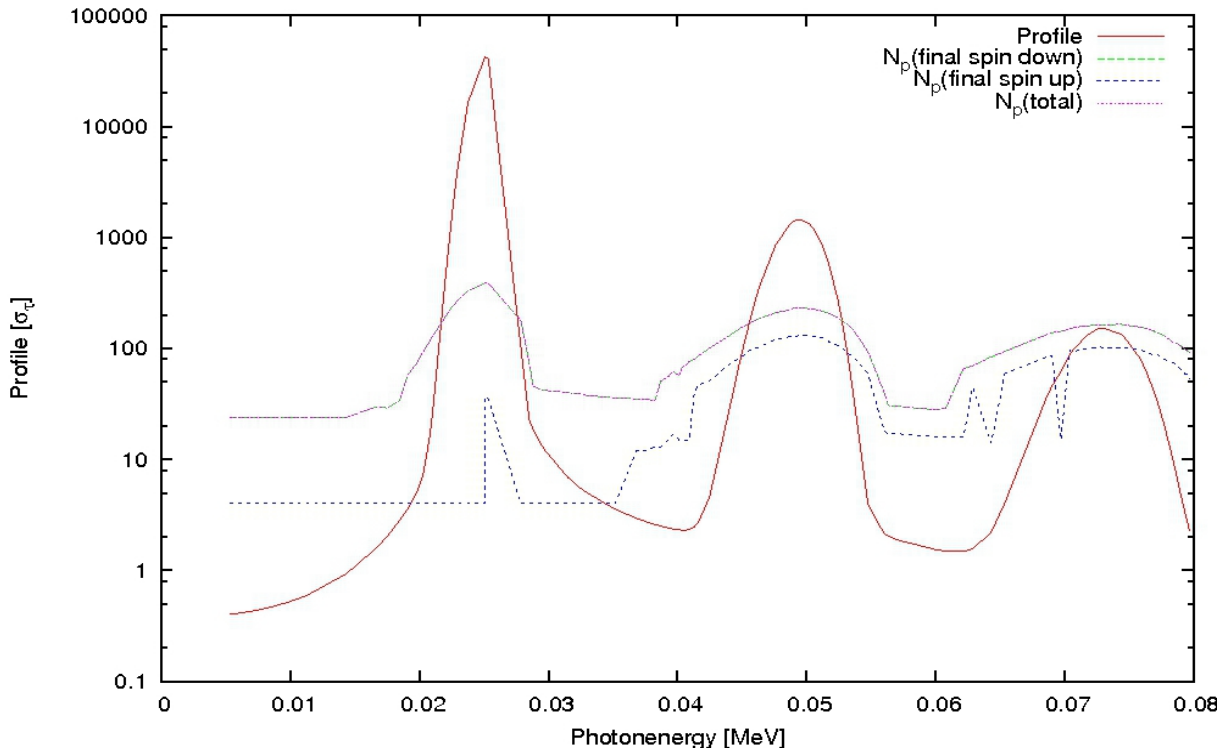


Figure 21: Number of momentum grid points for profile calculation. The solid curve shows the corresponding profile function.

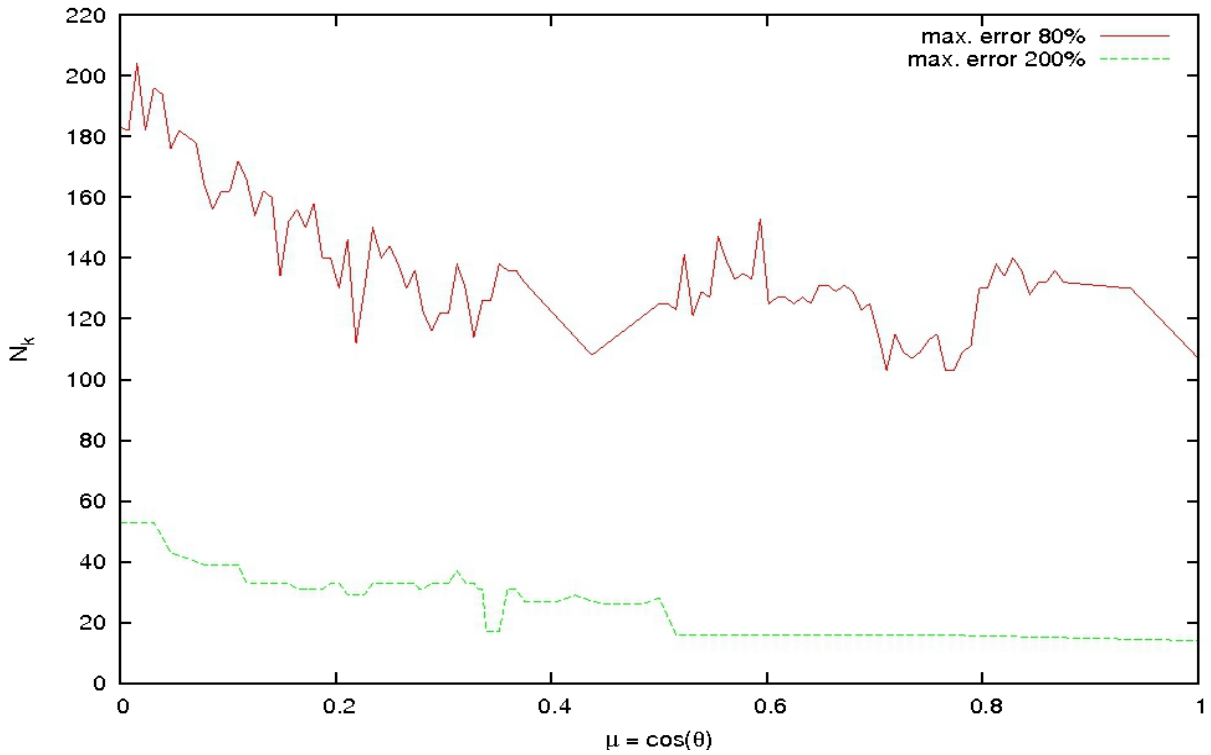


Figure 22: Number of energy grid points with respect to angle to the magnetic field.

this regime. This motivated a adaptive procedure for the grid refinement also in k and μ for the creation of the interpolation tables. The starting μ -grid consists of at least two boundary grid points which can be chosen to be $\mu_1 = 0$ and $\mu_{N_\mu} = 1$ because the calculations are performed in the electron rest frame which is symmetric in negative and positive μ values. For all starting points a k -grid is generated adaptively starting again from a start grid which is consisting of the energy boundaries and some special points ensuring the proper sampling of the peaks which are the resonant energies ω_{res} (Eq. 42), the cut off energies ω_{cut} (Eq. 44) and two points right before and right after them ($\pm 0.1\% / \pm 1.0\%$) for all Landau level which are taken into account. The splitting is done by inserting a new grid point in the middle of two starting grid points, performing the calculation and comparing it with the corresponding interpolated result. If the error is larger then a defined numerical value the intervals are recursively split further until the desired interpolation accuracy is reached. Now a two dimensional interpolation method is utilized to do exactly the same with respect to the μ grid. Several methods were tested and implemented like linear interpolation, logarithmic interpolation and four point interpolation for the case of equally spaced grid points (Abramowitz & Stegun, 1964) with the latter one not being used because of the reliability of the adaptivity. Logarithmic interpolation converges faster for the k refinement while there is almost no speed gain for the μ part as compared to linear interpolation. The inaccuracies of the interpolation methods due to the shift of the resonant energies with μ can be eliminated by converting the photon energy k to a new coordinate (Harding & Daugherty, 1991)

$$k_{\text{rel}} = \frac{\left(\frac{k}{m} \sin^2 \vartheta + 1\right)^2 - 1}{2B \sin^2 \vartheta} \quad (78)$$

representing the order of the resonance as a real number.

The visualization of such a table is depicted in Fig. 23. The contours are showing the positions where the resonant condition (Eq. 42) is met, the positions of the relativistic energy cut offs (Eq. 44) for the different Landau levels and points with equal profiles. The profile functions are extremely peaked for small μ which corresponds to photons nearly perpendicular to the magnetic field. For larger values of μ the profile functions are smeared out by the thermal momentum distribution parallel to the field. The reason for this behavior is that a photon perpendicular to the magnetic field can only transfer perpendicular momentum components to the electron which are quantized and therefore this is only possible if the photon has exactly the resonant energy. There is, of course, some minimal broadening due to energy uncertainties caused by the finite lifetime of the excited states.

4.5.4 Computational methods: Multiprocessing

The calculation of profile interpolation tables takes significant CPU time. A single CPU needs about 6–15 hours, depending on the internal numerical convergence criteria, to calculate such a table for a minimum interpolation accuracy of 50%. For the calculation of Green's function tables many of them have to be calculated. Therefore methods were investigated to reduce the time consumption. Though Moore's law which states that the number of transistors that can be placed inexpensively on an integrated circuit doubles approximately every two years, at the moment in principle stays valid, the clock frequency raise declined. That has its origin in the raising power consumption. The power consumption of compute nodes also doubles every 18 months (Feng, 2003) making efficient cooling systems unavoidable for high end systems. The future of super-computing therefore is efficient parallel computing, also called multi-processing. That is not a new concept at all. Parallelization has always been an important issue regarding

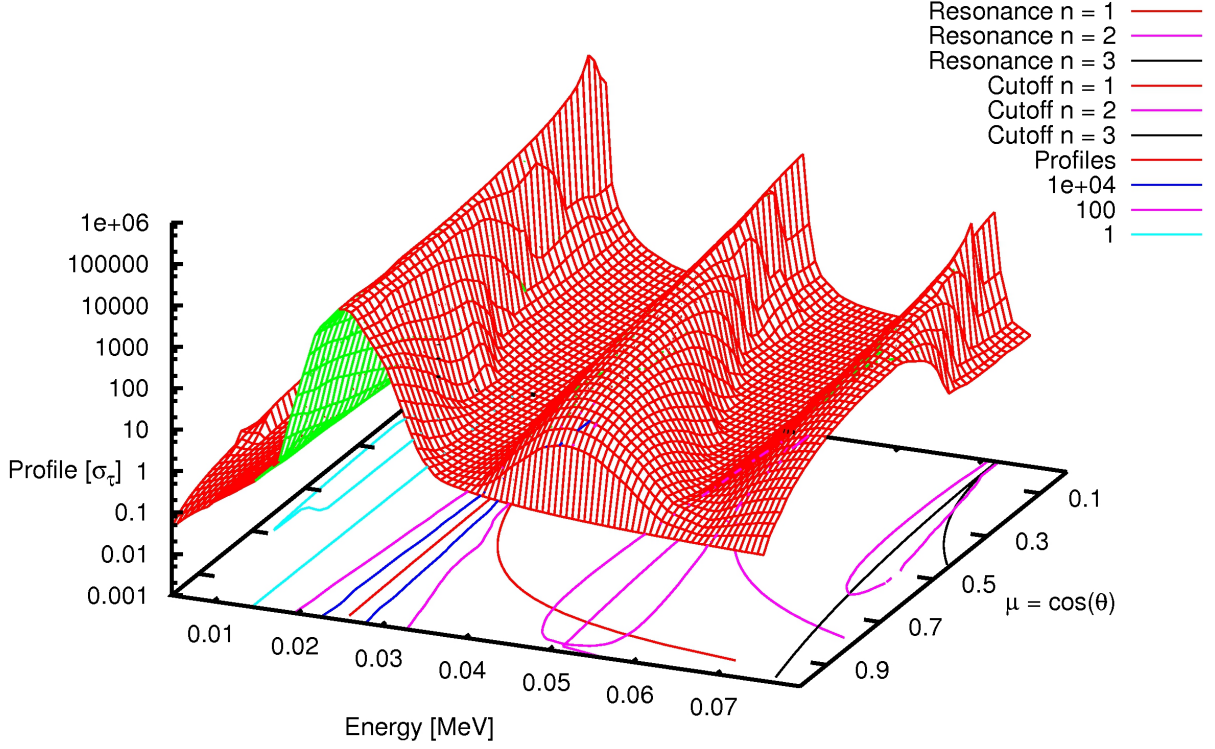


Figure 23: Visualization of a profile interpolation table storing profiles for different values of μ and k on adaptive grids. The contours show the resonance energies ω_n , the relativistic cutoff energies ω_{cut} and some standard contours for different values of the profile. The calculation was performed for a magnetic field of $B = 0.05$ and a maximum error of 30%. The profile cut-offs due to the cut off energies (Eq. 44) can clearly be seen for small μ . Also the zero line width of the cross sections at $\mu = 1$ (compare Fig. 11) results in the higher harmonics disappearing. This leads to a much larger mean free path and therefore to an increased probability of corresponding photons leaving the line forming region and becoming observable. This implies that the corresponding absorption features should almost disappear which can be seen clearly in the simulated spectra.

internal optimization by parallel floating point operation instructions or memory read out. Now that processors will not become very much faster but will instead get more cores responsibility gets transferred to the programmer and with great responsibility comes great power.

There are three possibilities for making use of more than one processor: A Monte Carlo simulation can in principle just distribute the input photons between different processes running the same program on several processors. In this case no communication is possible between the processes. For a problem that has to be solved by multiple processes together a communication mechanism is required. Such mechanisms are provided by OpenMP and MPI. OpenMP is a shared memory multiprocessing method (Hoffmann & Lienhart, 2008). Its main advantage is the straightforwardness of extending a linear program to multi-core functionality by the usage of precompiler instructions which are ignored if no multi-core environment is available. Its main restriction is the missing of inter-node communication. A compute node typically consists of more than one processor sharing the same memory. Nodes can be connected via any kind of networks. The SETI@home project, for example, bundles the computational power of private PCs via the Internet for the cause of searching for extraterrestrial intelligence. Professional clusters on the other hand make use of Infiniband interconnections a type of network providing very high bandwidth. In the course of this thesis I used the Woodcrest cluster of the Regionales Rechenzentrum in Erlangen (RRZE) for expensive calculations. It consists of 217 compute nodes, each with two Xeon 5160 "Woodcrest" chips (4 cores) running at 3.0 GHz. A lack in inter-node communication on this cluster implies a maximum number of 8 processors which is 8 times smaller than the maximum number of processors available for a job without special permissions. This was absolutely unacceptable though OpenMP was tested on Woodcrest and found to be good. Therefore the Message Passing Interface (MPI) was used. MPI is a communication standard specified by the MPI Forum (Sept. 14, 2010), an open group with representatives from many organizations that define and maintain the standard. Different implementations of the standard are available. OpenMPI (the successor of LAM MPI), MPICH2, and Intel MPI were tested and showed only minor differences regarding some special operations. In contrary to OpenMP which provides some basic data reduction methods communication has to be performed by the programmer but these methods are in principle also available. The programming of a program exchanging information with other identities of the same program is very error prone. Common mistakes are the so called dead locks in which two processes are accidentally waiting for a confirmation of, for example, their send request to each other at the same time but since both are waiting no process will receive the other ones message. Hybrid codes using both, MPI and OpenMP, are even more complicated and it remains unclear whether the performance gains of the hybrid approach compensate for the increased programming complexity (Nakajima, 2006).

Fig. 24 shows the output of an Intel program called *Traceanalyzer* which visualizes information about process states and inter-process communication stored during the execution of an MPI program if it has been compiled with the corresponding options. The multi-core efficiency is at about 30%. That can be seen by comparing the time the clients are working (blue bars) to the time in which they do nothing because they have to wait for something (red bars). In this case a simple Master-Worker scheme was used. A master process which does the interpolation and grid refinement sends parameters to the clients which perform the calculations and send back the results to the master. Everytime a client finishes a calculation which in the case of the profiles tables results in one profile for a certain energy and angle the master compares the result with an interpolation between the boundary grid points. If the desired accuracy is not reached yet, the intervals are split further and two new sets of parameters are sent to the next available clients. Such a interval splitting can be seen in the figure with the involved messages being indicated by black arrows on the right side. Client number 7 finished its calculation and

sends the result to the master process. After the accuracy was probed and found to be insufficient the master sends the parameters of the newly inserted grid points to two free processes. This happens nearly at the same time and can not be investigated by using simple messages to stdout because the order of their appearance is not guaranteed to correspond to the time of their creation by the MPI standard. The *Traceanalyzer* therefore is a very useful tool for debugging such inter-process communication.

Fig. 24 also illustrates the problem which is leading to bad efficiency: The clients performing calculations in regions where a lot of grid points are required, for example within the resonances, are inhibiting other clients which already finished their calculations. The idle clients now have to wait for the others to finish, before further refinement of the angular grid can take place. Several possibilities are possible to avoid this like allowing calculations for different μ at the same time. But the efficiency actually is not so bad if one takes into account scalability which is an important benchmark parameter for multi-core applications. Scalability is a measure of how much time can be gained if the processor number is increased. Ideally doubling the number of processors halves the time required for calculation. Practically this is not possible and multiple processors running the same program independently will be faster than multiple processes running identities of the same program and solve a problem by communicating with each other. The efficiency of the *accp* program is not very good but also does not change significantly if the number of processes is increased which leads to a good scalability. In other words the efficiency of about 30% is reached with 4 as well as with 64 processes.



Figure 24: Screenshot of the output of *Traceanalyzer*. The blue and red bars indicate that the corresponding clients are working or idle respectively.

4.5.5 Mean free path sampling

At the first place only the evaluation of the thermally averaged compton scattering cross sections (profiles) was replaced with the old momentum sampling still in use. Fig. 25 shows the profiles sampled by revision 1 and 2 of the MC code. The mean free paths from the 1st revision seem to be smaller by factor of 2 which leads to more scattering processes within the column. In principle this means that spectra produced with the old code can be interpreted as spectra for optical depths at least double as large as intended depending on the geometry.

Fig. 26 shows the profiles calculated by the *accp* program and profiles from Harding & Daugherty (1991) with the same parameters. They perfectly agree for all temperatures and angles as they did in comparisons with other magnetic field strength. For very large temperatures

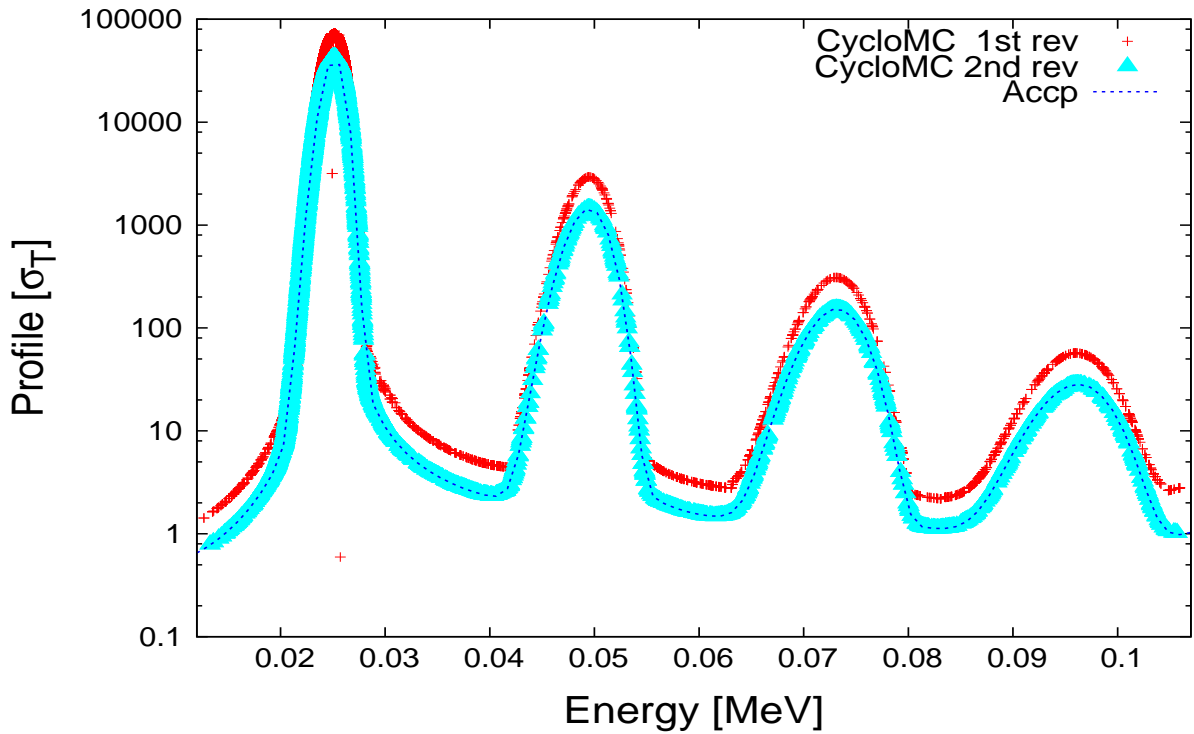


Figure 25: Inverse mean free path logged during simulation runs of the 1st (crosses) and 2nd (triangles) revision of the MC code. The dashed line shows the values calculated with the *accp* program proofing the new mean free path calculation right since the program reproduces the profiles from literature.

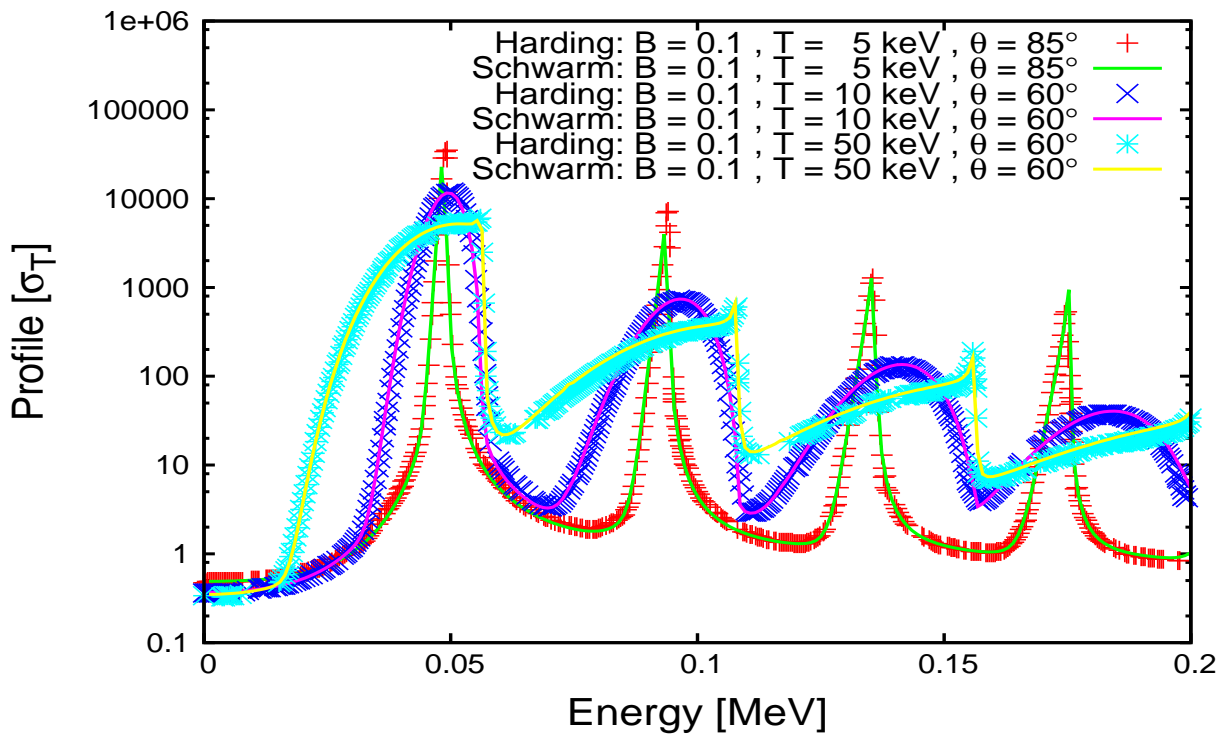


Figure 26: Comparison of the profiles from Harding & Daugherty (1991) to own calculations for different angles and temperatures.

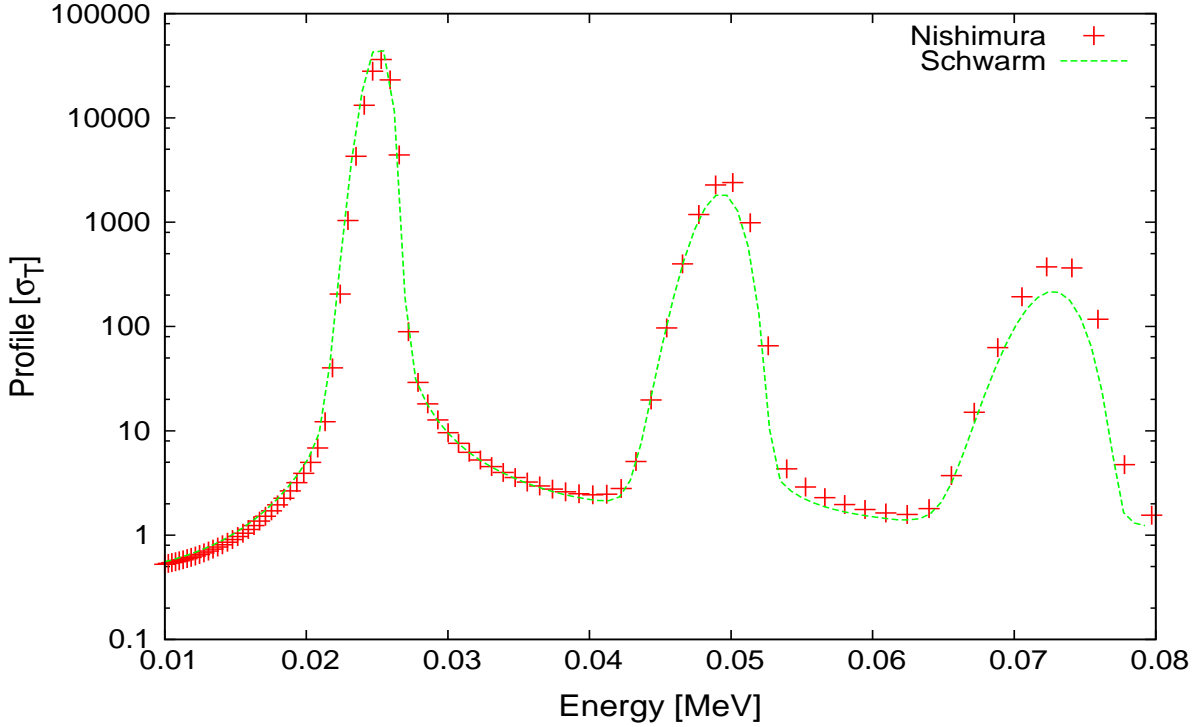


Figure 27: Comparison of the profiles from O. Nishimura to own calculations.

the profiles peak at the cut off energies as expected (see Section 2.3.2) while they are sharply peaked within the resonances for small $\mu = \cos \vartheta$. Fig. 27 shows a similar comparison to the profiles calculated by O. Nishimura. He uses a approximation making use of the absorption cross sections (Eq. 49) for the scattering cross sections (priv. comm.). Both calculation methods agree well in the continuum part with some deviations in the resonances especially in the higher ones.

4.5.6 Results

Fig. 28–30 show the resulting spectra compared to the ones from the first revision for different geometries. Compared to the first revision all geometries clearly show a reduction of the depth of the first harmonic and strongly reduced line wing emissions at the fundamental line. The trend of smaller harmonics for smaller optical depths can also be seen in the spectra of the first revision as shown by Schönherr (2007). This result further constrains the assumption that the usage of mean free paths, smaller by a factor of 2, could be compensated by using decreased optical depths. For further analysis the spectra from the first revision were calculated for a optical depth of 5×10^{-4} which is half of the optical depth which was used so far. Fig. 31 shows the resulting spectra compared to the ones from the second revision which are the same as in the middle panels of Fig. 28–30. Only one angle bin $0.250 \leq \mu < 0.375$ is shown here and the three panels correspond to the different geometries. The spectra exhibit a nearly identical shape except for the right line wing of the fundamental which is much stronger for the smaller optical depth. Such strong line wings have not been observed in X-ray spectra yet and seem to be a numerical artifact appearing for optical thin line forming regions: “For very small optical depth, $\tau_T = 10^{-4}$, this initial emission feature [the line wings] can be confirmed by the Monte Carlo simulations presented here.” (Schönherr, 2007)

Concluding the results in this section one may say that the MC code up to now used wrong

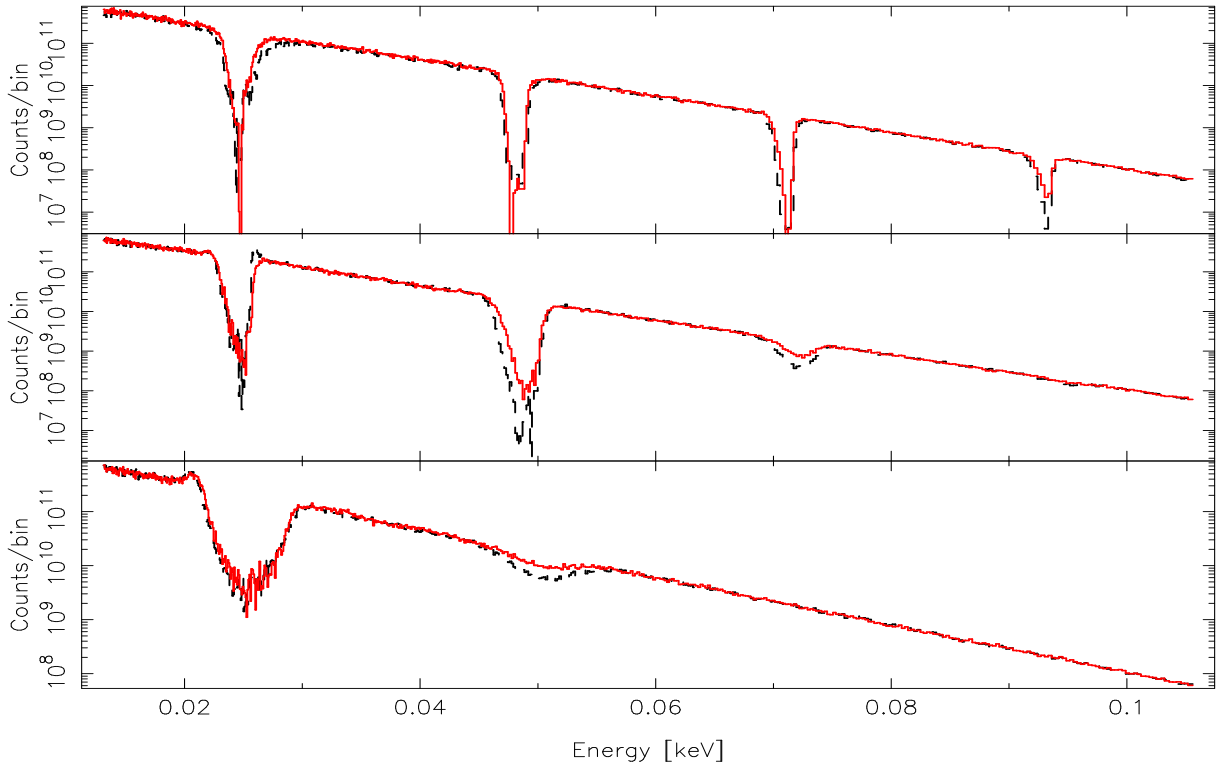


Figure 28: Comparison of the spectra resulting from revisions 1 (dashed) and 2 (solid) for $\mu \in [0 : 0.125[$, $[0.250 : 0.375[$ and $[0.750 : 0.875[$ from top to bottom. The magnetic field strength is $B = 0.05$, a temperature of $T = 3$ keV was chosen for the momentum distribution, the optical depth is $\tau = 10^{-3}$ and a slab 1-0 geometry was assumed.

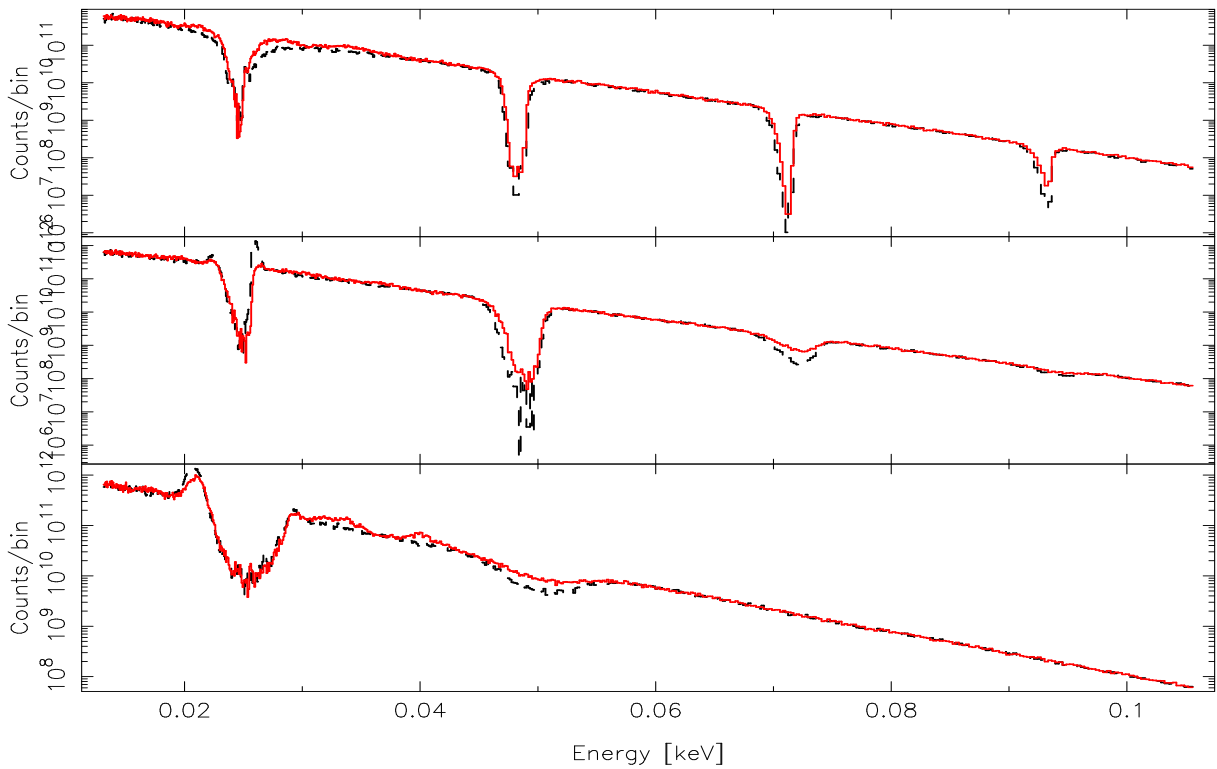


Figure 29: Same as figure 28 but for slab 1-1 geometry.

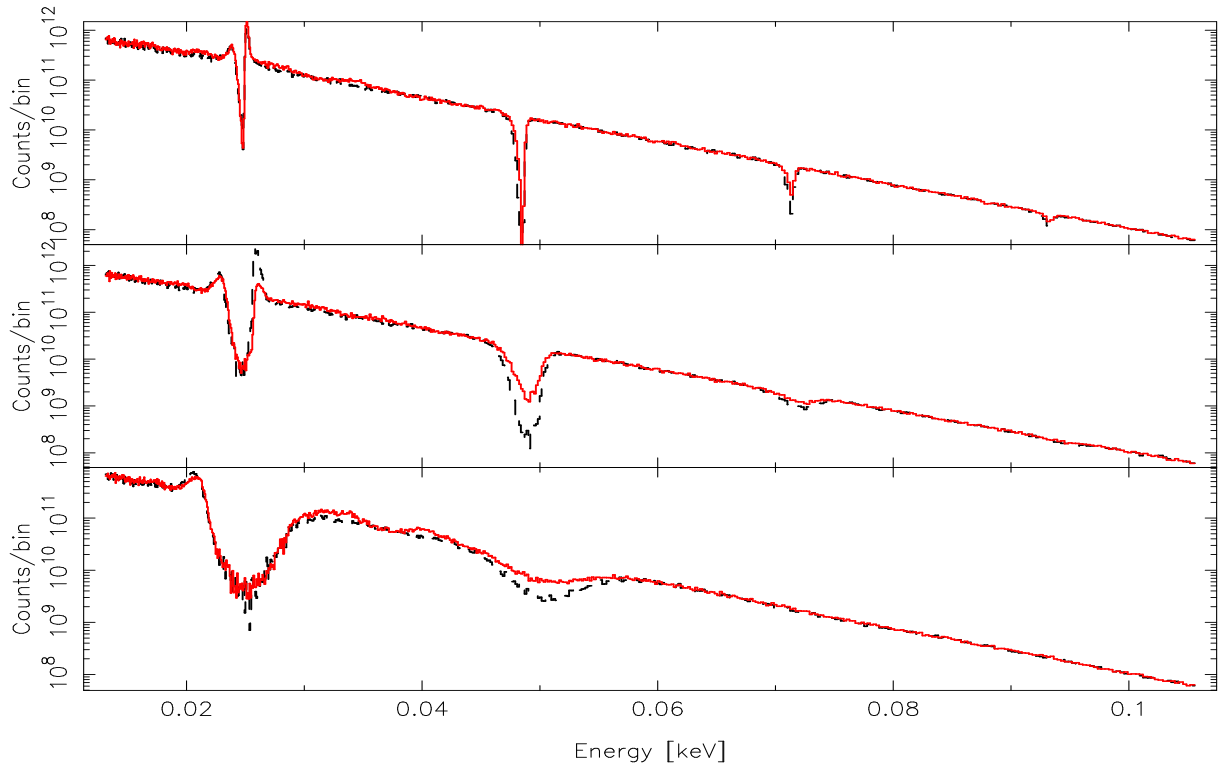


Figure 30: Same as Fig. 28 but for cylinder geometry.

mean free paths smaller by a factor of 2 than the correct ones which resulted in an effective optical depth larger by a factor of 2.

4.6 MC code: 3rd revision

Up to now I described the implementation of a new mean free path sampling in the old MC code which reproduces the profiles from literature and speeds up calculations due to its interpolation nature. The next step was to check the MC code for further error prone parts. The MC simulation should become reliable first before new lengthy Green's function table calculations are started using the revised code. For that reason some suspicious functions of the code were analyzed and independently tested. Unfortunately no example momentum sampling results could be found in literature and therefore new code was developed and integrated in the *accp* program for the reason of comparing its output to the old MC momentum sampling.

4.6.1 Aims: Revised momentum sampling

First of all the momentum sampling was thoroughly checked because the profiles turned out to be wrong and the momentum sampling might have been using the wrong methods, too. The momentum sampling is not only done using the same integrand as for the mean free path evaluation as described above, but was actually already done by the *accp* program and stored in a binary table while calculating the profile. So the old momentum sampling could be replaced easily by own functions at no additional cost. Hereinafter the methods and results of the implementation of an selfwritten momentum sampling implemented in the MC code shall be argued.

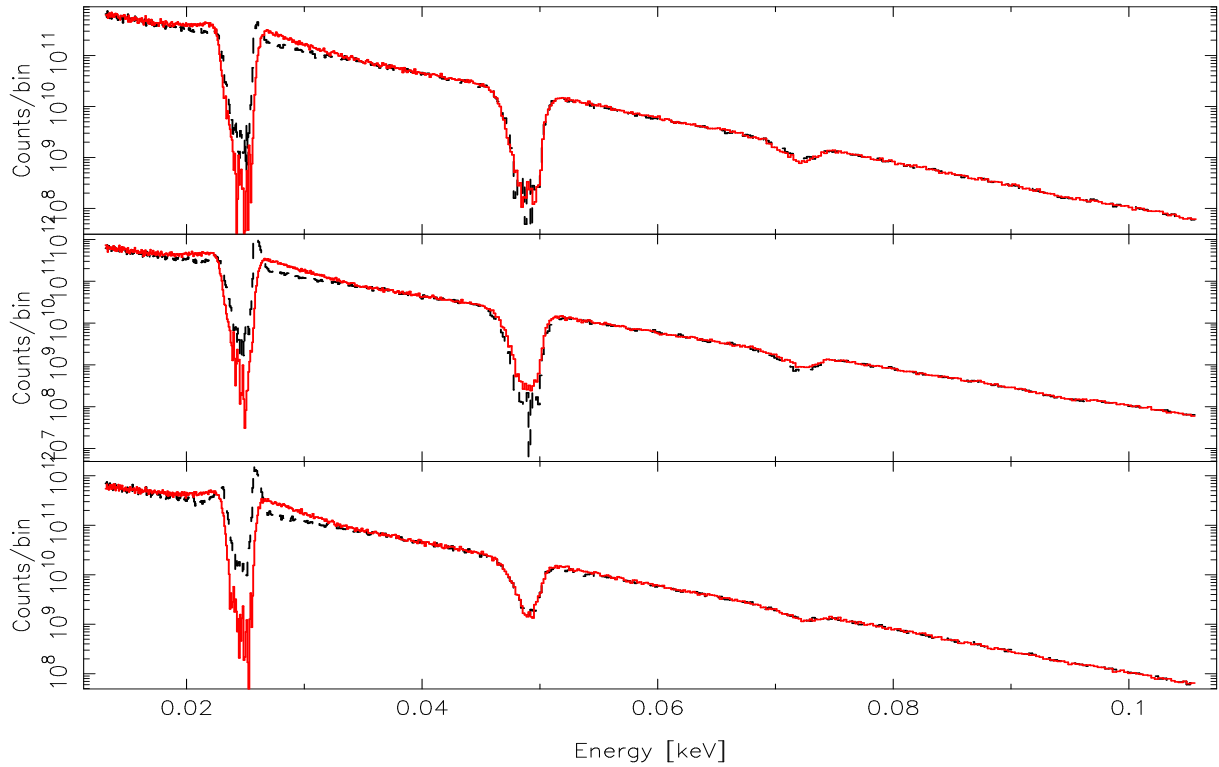


Figure 31: Comparison of spectra from the first revision for $\tau = 5 \times 10^{-4}$ (dashed) and the second revision for $\tau = 10^{-3}$ (solid). Slab 1-0, slab 1-1 and cylinder geometry are shown from top to bottom respectively and the angle bin includes μ with $0.250 \leq \mu < 0.375$.

4.6.2 Numerical methods: Binary search

The adaptive integration described above already provides the momentum sampling distribution function which should not be confused with the thermal momentum distribution function from which it differs in including the information about the scattering photon's energy and angle. All integral values which satisfy the intentional accuracy have already been saved in memory in a cumulative way. This means that the integral value calculated before is added to the actual value and all values are normalized once the total integral has been calculated. For sampling the electron parallel momentum a random number is assigned to a value of this cumulative distribution function (see Section 3.2) and the momentum is interpolated from the corresponding boundary grid points. Since the profiles are stored in a cumulative way they are monotonically increasing. This makes it possible to apply a binary search for finding the boundary grid points. A random number is generated and given to the search function together with a structure storing the distribution function. The binary search then splits the hole interval ($[0 : 1]$ in this case) and tests whether the random number is located in the one or the other by comparing its value to the interval midpoint. This process is reiterated until no further splitting is possible and the surrounding grid points are then used to interpolate the sampled momentum.

4.6.3 Momentum sampling

The mean free path and momentum sampling was replaced by own functions called from the exact same place in the code. The old implementations were removed to save computation time and mean free paths and momenta have been book-kept to follow the impact of those changes on the models. Fig. 32–34 show the sampled electron momenta for different μ . They are very

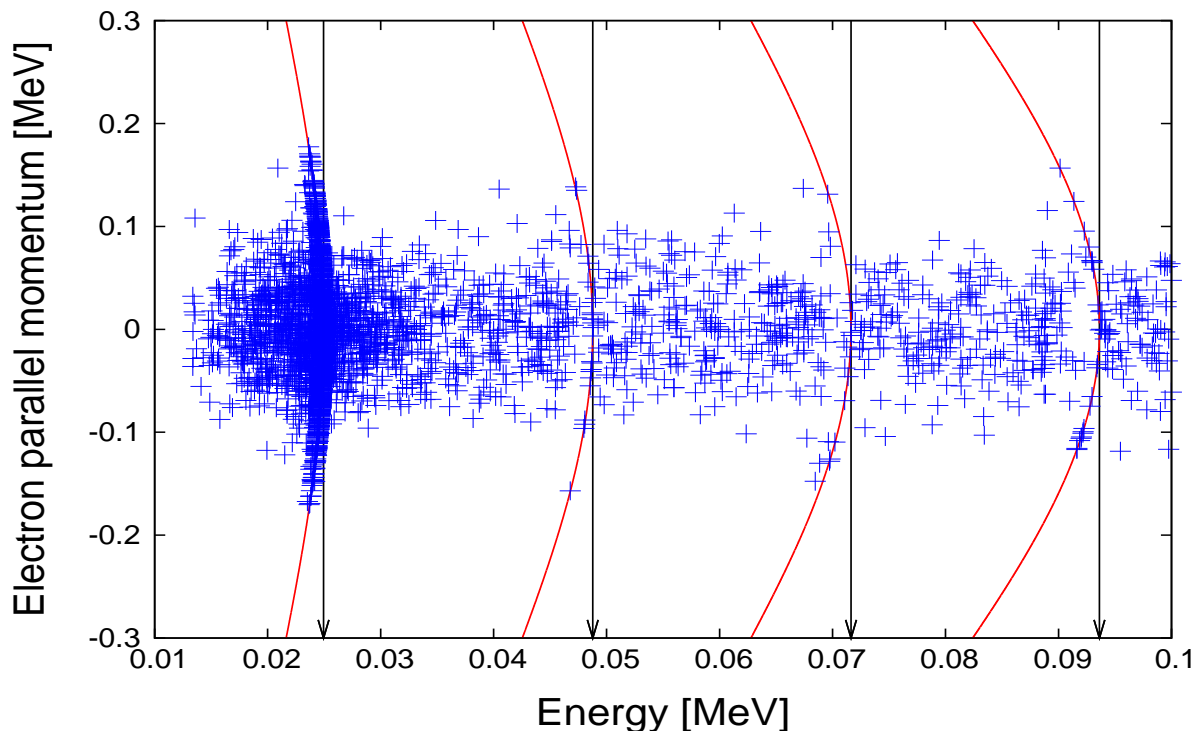


Figure 32: Sampled electron parallel momenta (crosses) for $\mu \approx 0$ and corresponding cutoff energies ω_{cut} (vertical arrows) and zero line width solutions (solid curves) indicating (k, p) pairs at which the conservation laws for cyclotron absorption are satisfied (see Section 2.3.2). Above the cutoff energy no solution exists and therefore only scattering can take place. Right before the cutoff energies on the other hand photons “want” to be absorbed so they are “searching” for an electron which has exactly the right momentum to fulfill the conservation laws.

helpful for the understanding of the relations between the cutoff energy, the possible solutions for the conservation laws, also called zero line width solutions (Araya & Harding, 1999), which are limited by the former and the distribution of the actually sampled momenta. The points on the zero line width solutions are representing the resonant part while the momenta distributed around $p = 0$ correspond to scatterings in which the initial photon somehow persists. In the vicinity of the resonances resonant behavior is preferred while it is suppressed in regions where momenta which would fulfill the conservation laws are not available due to their low abundances in the momentum distribution.

Comparing the electron momentum distribution of the first revision (Fig. 20) with the one from the second revision one can see that both momentum sampling schemes seem to agree quite well. The first revision exhibits much more data points which has its origin in the lower mean free path, but since it is done totally independent from the mean free path calculation (for the zero line width solutions) or at least by using relative mean free path integrals the wrong profiles do not seem to affect the momentum sampling.

4.6.4 Results

A comparison of the third to the first revision can be seen in Fig. 35–37. The higher harmonics do not change much for small μ no matter which geometry is chosen but they are significantly reduced for larger values of μ like in the first comparison. The fundamental line is again chang-

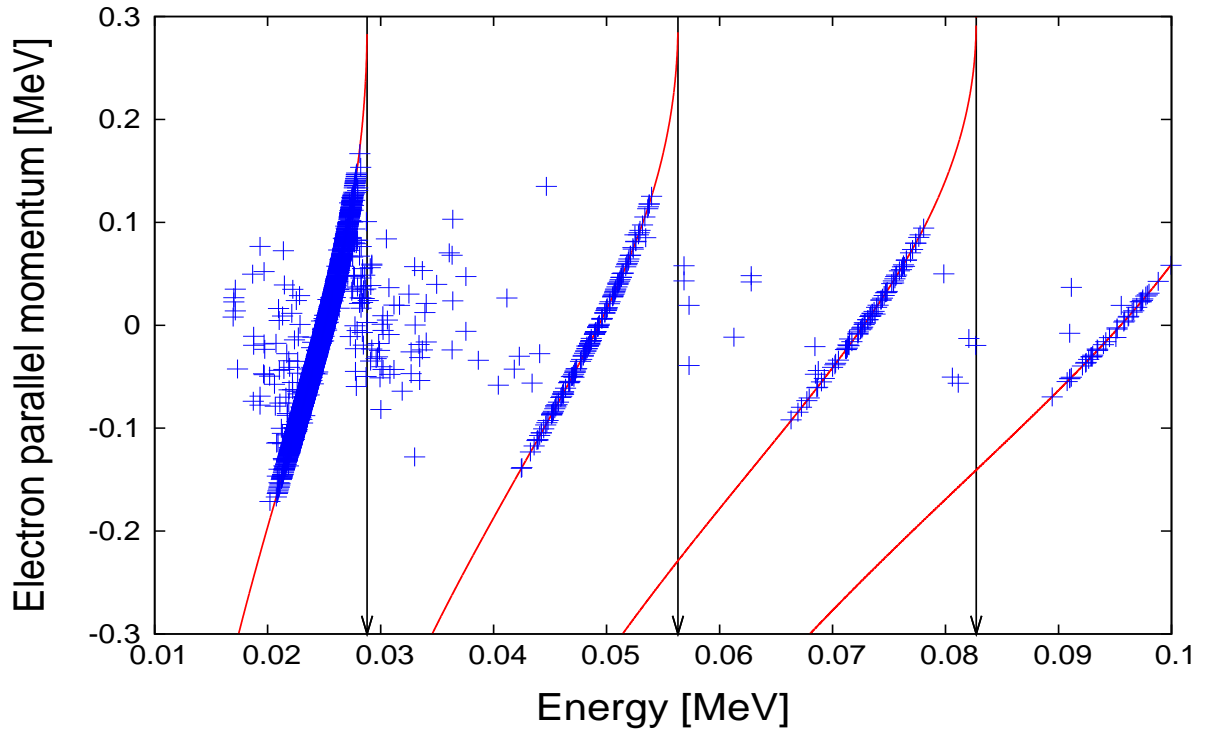


Figure 33: Same as Fig. 32 but for photons with an incoming angle of 60° to the magnetic field ($\mu \approx 0.5$). The cutoff energies are shifted to higher values according to Eq. 44 rendering the fourth one already invisible in the energy range taken into account. Also the momentum parity symmetry is broken because relativistic effects involving the boost of the projection of the photon energy on the magnetic field axis (which is zero in the $\mu = 0$ case) have to be taken into account. Like in Fig. 32 the majority of the momenta in regions where the conservation laws can be satisfied are congruent with the zero line width solutions. It of cause also depends on the thermal width of the momentum distribution if such solutions are available practically.

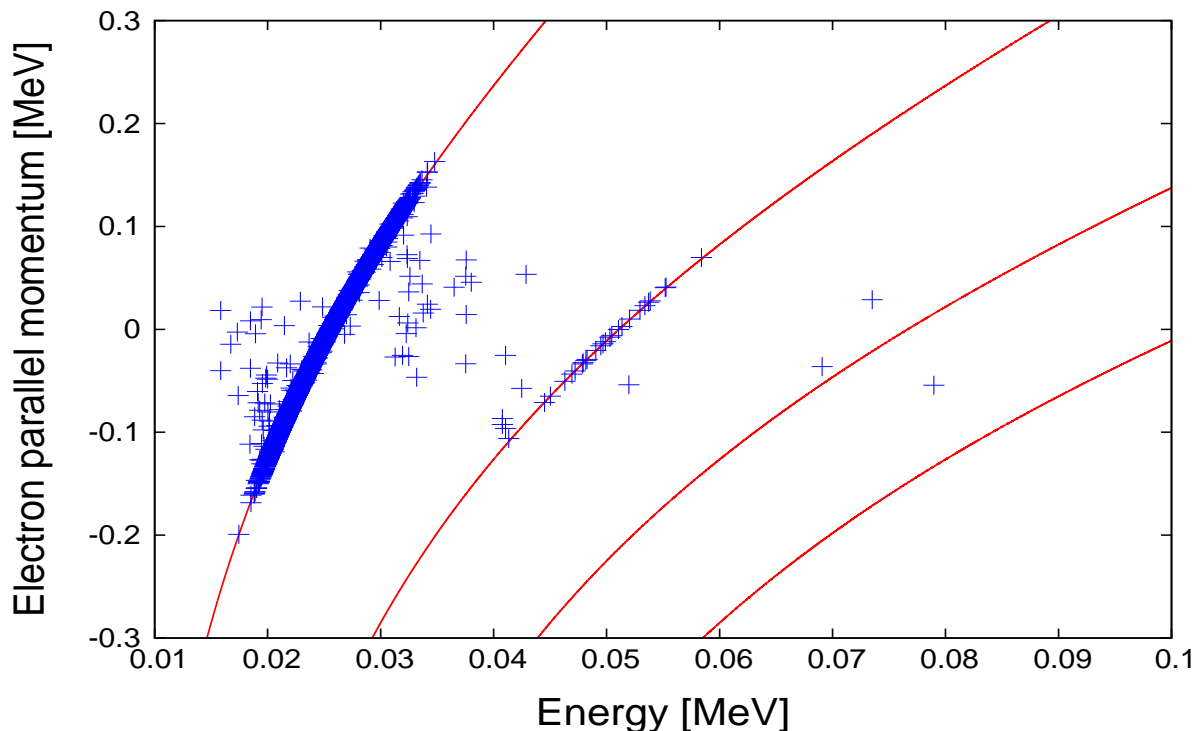


Figure 34: Same as Fig. 32 but for $\mu \approx 1.0$. The relativistic effects get maximal in this configuration and the cutoff energies diverge.

ing significantly especially in the line wings which are becoming less sharp. The momentum sampling has at least a great impact on the line wings and should be done very carefully since it is mainly responsible for the complex shape of the fundamental line.

4.7 CycloSim: The new Code

The old MC code has been revised and improved. Sampled mean free paths and electron momenta have been compared to calculations by other authors and are finally believed to be sufficiently validated. Nevertheless the old MC code appears to lack a clear structure and it is uncertain that all errors have been eliminated. Furthermore the sampling of the required parameters as described in Chapter 3 cedes clearance to the programmer regarding the order of execution. Therefore I developed a new Monte-Carlo simulation program. The principles of this new code are explained in the following section.

4.7.1 Aims: Less restrictions and a readable and maintainable source code

The main goal was to replace the old MC code by a completely new code written in C and considering modern requirements such as multiprocessing scalability. It is transparent in terms of maintaining and debugging of the code by making use of a well organized and defined set of functions. A library called *libaccp* containing all functions required for calculation, sampling and interpolation during the propagation of a photon through a CRSF medium was developed. The corresponding program *accp* provides a user interface to those functions which can be used to reproduce the graphs in this thesis. Furthermore it is able to create interpolation tables for profile functions by refining both the energy and the angle grid in an adaptive way. The calculation of such interpolation tables is computational intensive and a simple Master-Worker

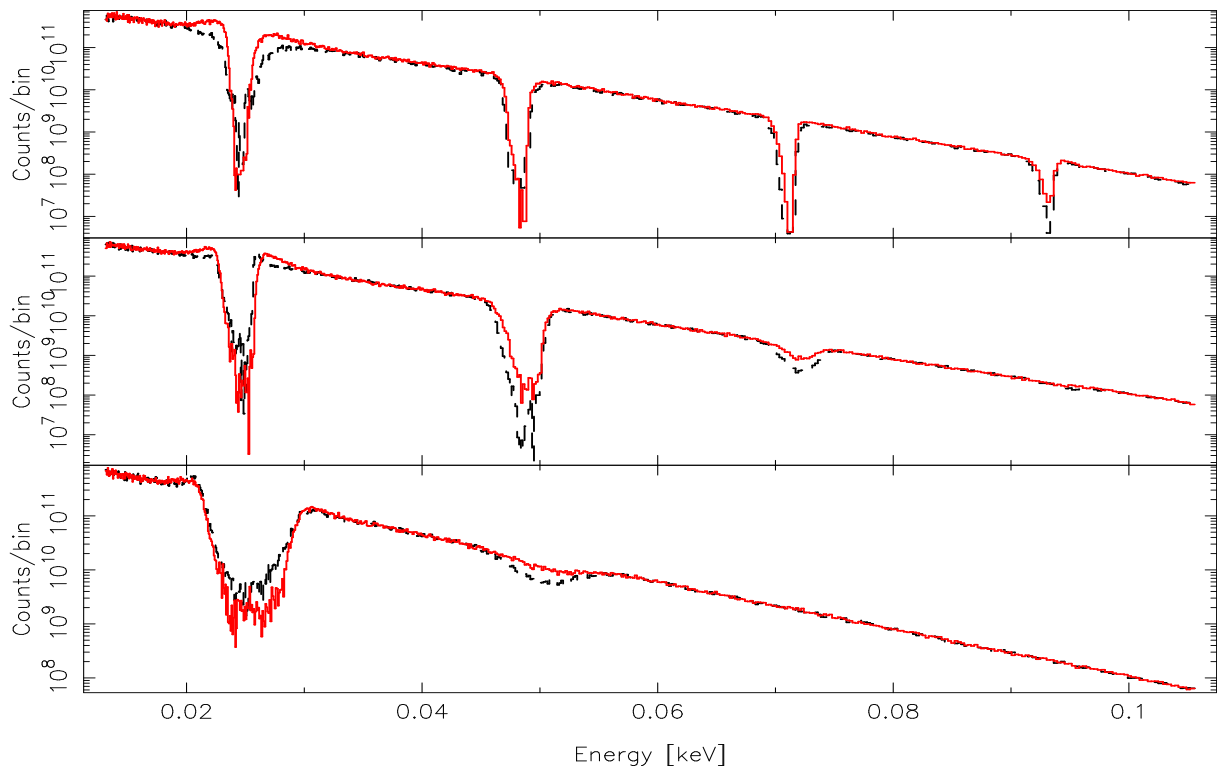


Figure 35: Simulated spectra of the revisions 1 (dashed) and 3 (solid) for a slab 1-0 geometry and same parameters and μ values as in Fig. 16.

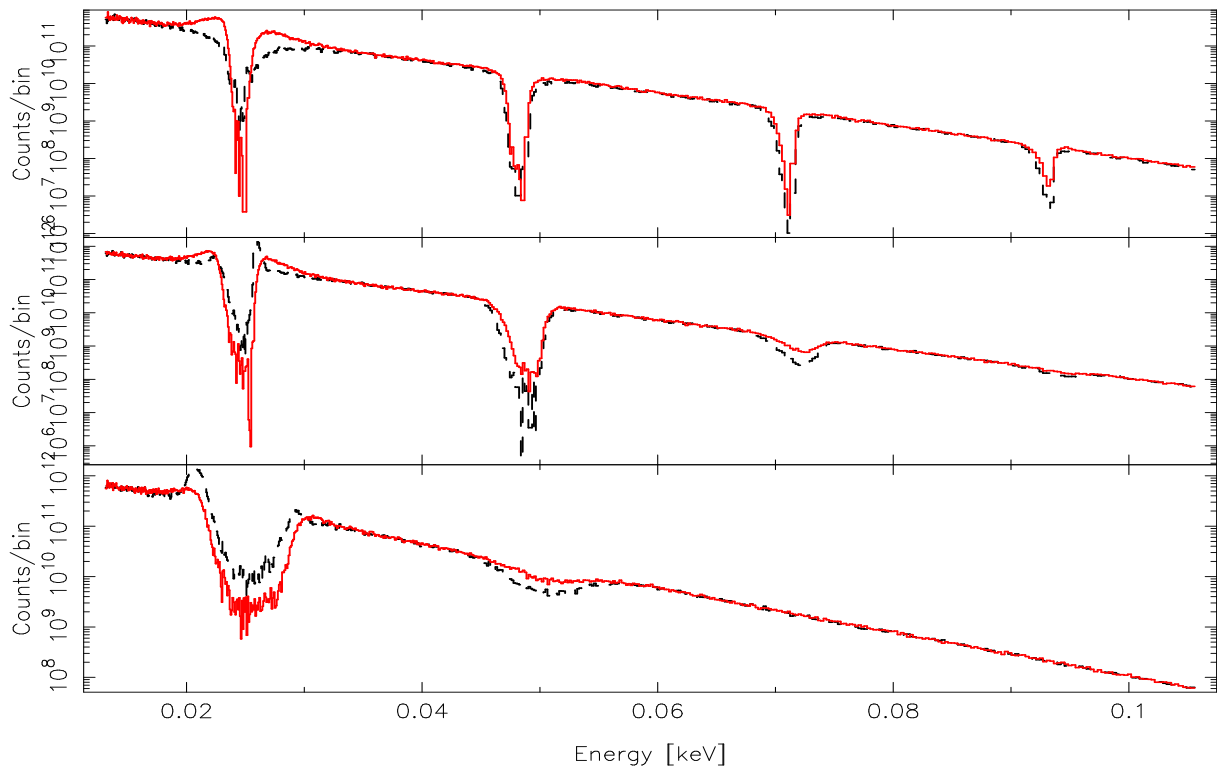


Figure 36: Same as figure 2 but for slab 1-1 geometry.

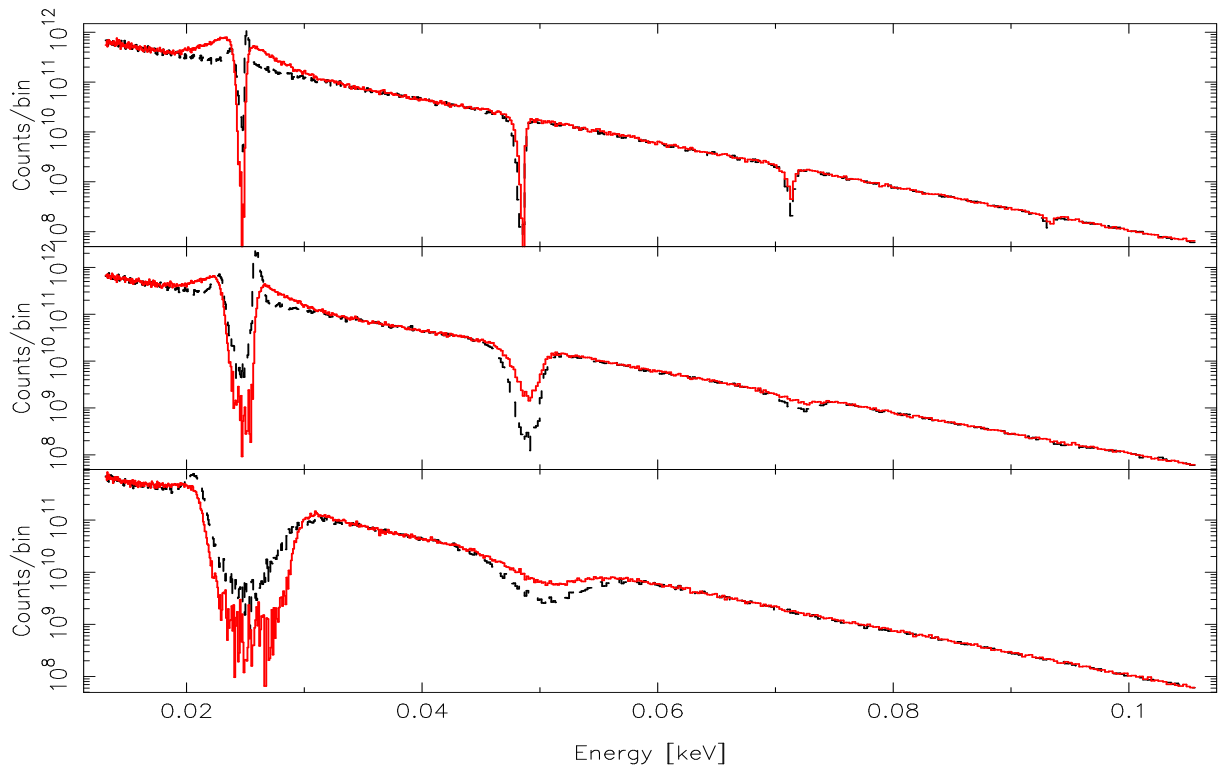


Figure 37: Same as figure 22 but for slab 1-1 geometry.

scheme was applied for the ability of multiprocessing. The information stored in those tables does not only contain the full profile integral and its cumulative distribution function, but also the spin dependent profile functions for initial electron spins up and down. The later ones are not used at the moment since all calculations are done using spin and polarization averaged identities but they are necessary if polarization effects are taken into account in future revisions of the simulation.

Another program called *CycloSim* is taking care of the actual propagation process using the *libaccp*. Great effort was put in the development of a framework which is not only taking into account some physical model properties like the presence of more than one source, more complex geometries, magnetic field gradients and velocity gradients which have not been implemented in the old MC code, but is also easily expandable to polarization dependent treatment. More over it is able to operate in a Master-Client mode as well as in a combined Master-Client / Client-Client mode. The later may be necessary if large interpolation tables have to be loaded into memory for each plasma configuration which may result in the need of distributed memory multiprocessing not only for speed up of simulations but also for having enough memory available.

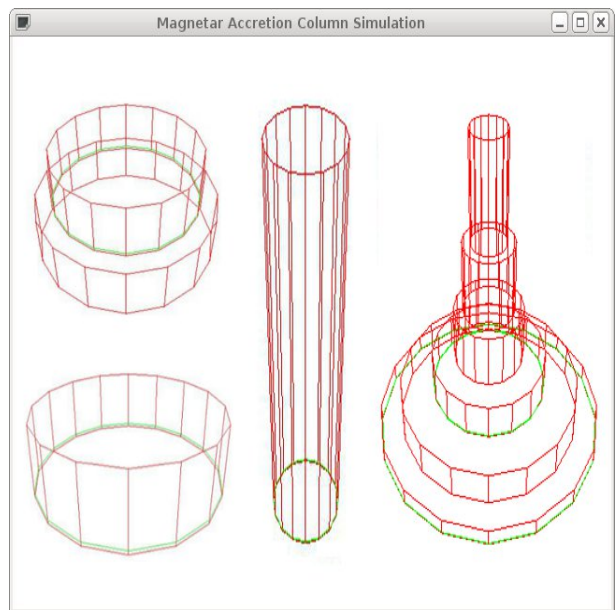


Figure 38: Visualization of some simulation geometries as seen in the OGL mode of *CycloSim*.

The program also has a debugging mode which makes it possible to visualize both the accretion column model and the emitted photons in an OpenGL window. Fig. 38 also shows the visualization of a simulation with a more sophisticated column geometry. Cylinder slices with different parameters can be created interactively as well as plane parallel sources lying under or between such slices. In the old MC program slabs are of infinite extent perpendicular to the magnetic field while they can have a certain optical depth perpendicular to the field in the *CycloSim* program. For the simulation of the old slab and cylinder geometries a very large optical depth of $\tau = 10^3$ was chosen perpendicular and parallel to the field respectively.

The position of a slab is determined by its magnetic field which is assumed to be constant within each slab. The width and the height of a slab in the visualization is proportional to the optical depth perpendicular and parallel to the magnetic field respectively. In Fig. 38 for example, the optical depths close to the surface are assumed to be the largest ones but that does not imply any restrictions on the radius of the accretion column which is related to the optical depth by the column density. Slab 1-0 and slab 1-1 can be seen in the lower and upper left corner respectively, the cylinder geometry is shown in the middle and an example of a more complicated configuration consisting of slab-like and cylinder-like slices on the right. The yellow circles are indicating the positions of the source planes.

4.7.2 Restrictions

The program was designed to avoid as many restrictions as possible, especially all common restrictions of other simulation codes. At the moment the implementation includes the slab 1-0 and slab 1-1 geometries which are based on flat circular planes emitting photons isotropically in all directions, but sources of any shape and origin can be implemented easily. Some changes involving the polarization depended storage of the calculated variables which will, of cause, increase the required disk space significantly have to be made if one wants to take into account polarization. Looking at future missions which will be able to determine the polarization states as well as spectra with even higher resolution this is highly desirable and already work in progress. For the moment all calculations are at least done by using methods ensuring that correct polarization dependent information is retrievable like the usage of physically meaningful electron wave functions.

4.7.3 Results

The following Section contains some preliminary results from the new cyclotron line model. Rather conservative sampling parameters and grids were used, because the program is still in the development phase. The new spectra are shown in Fig. 39–41. Slab 1-1 geometry was simulated by two identical slabs with optical depth $\tau_{\parallel} = 1.0 \times 10^{-3}$ each and a source plane between them emitting photons isotropically in all directions. The line positions agree with those from previous modeling attempts but the line shapes strongly differ. A major difference to the old MC code is that the first line is significantly deeper than the second one. Only for angles nearly perpendicular to the magnetic field the depth of the higher harmonics is comparable to the depth of the fundamental line. The expected broadening of the fundamental line for small angles to the field can be seen in the spectra as well as a very interesting local maxima in the the fundamental line for slab 1-1 geometry. The resulting double-peaked absorption features may provide useful information about the spawning process and its coherence with the line shape of the fundamental. Since there are no line wings in the new spectra it is possible that the spawned photons from higher harmonics fill up the inner fundamental line instead of its wings. Pavlov et al. (1991) discussed interactions with the radiation field which, for low magnetic fields

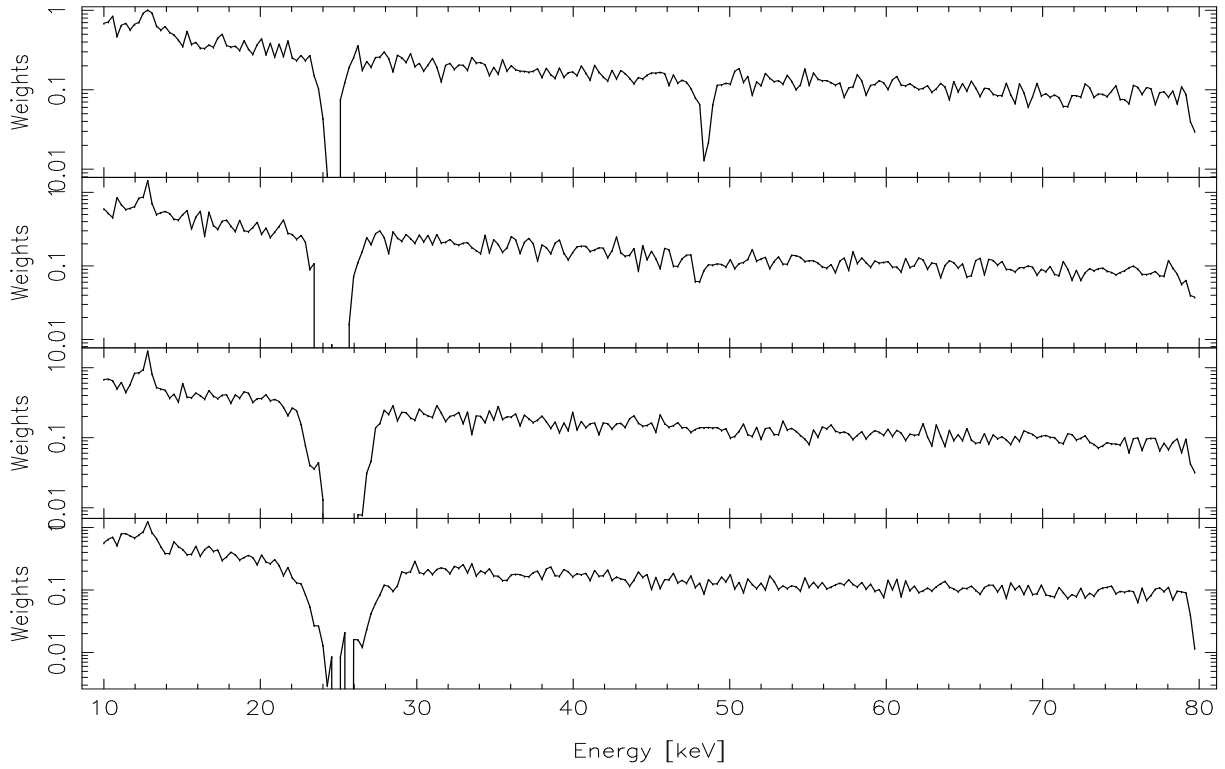


Figure 39: Spectra from *CycloSim* for slab 1-0 geometry. The magnetic field was set to $B = 0.05$ and a simple powerlaw input spectrum was used with a photon index of $\alpha = 1.0$. The four panels correspond to four angle bins with the top panel being the one for nearly perpendicular ($\mu \approx 0$) emission and the bottom one corresponds to photons escaping the line forming region nearly parallel to the magnetic field.

$B \sim 10^9 - 10^{11}$ G, should remove the degeneracy of the lowest Landau level, giving rise to an energy splitting. In the non-relativistic limit they found the amount of splitting to be

$$\Delta E \approx 0.6B \text{ keV} \quad (79)$$

If a resonance is corresponding to the transition involving the ground state, the line should split into a doublet with the low energy component arising due to the spin-down \rightarrow spin-down transition (no spin-flip). The component shifted to higher energies by ΔE arises from the spin-flip transition occurring for an initially positive electron spin. Taking into account transitions to higher Landau levels the line even becomes a triplet. Observing this splitting would require resolving power of $R \geq \frac{\omega_B}{\Delta E}$ at the cyclotron energy ω_B and one can look forward to new missions that might be able to offer this (see 5).

Another new feature is the small emission hump at 12 keV especially for slab 1-0 geometry. It may provide evidence for a certain preferred final energy of the scattering photons. But it is probably not the famous 10 keV emission feature (Mihara, 1995; Santangelo et al., 1998; Coburn et al., 2002) which is sometimes seen in observations because its position is changing with the magnetic field.

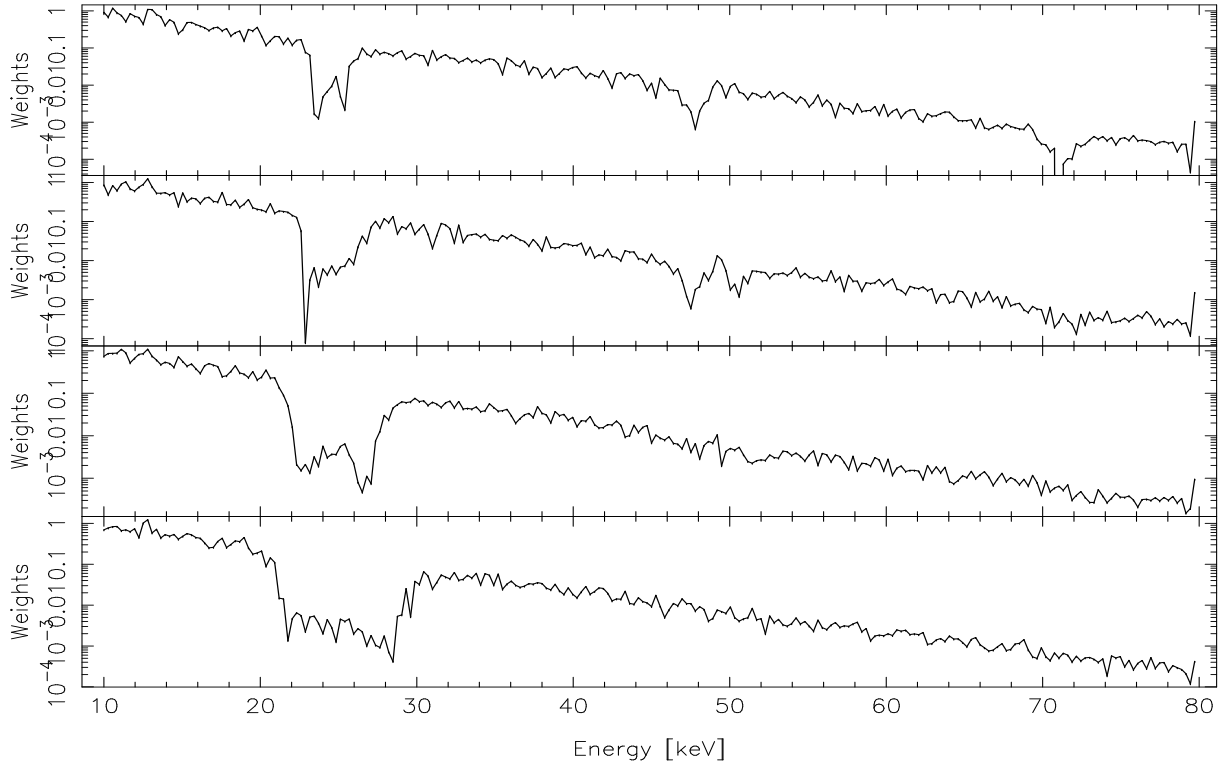


Figure 40: Spectra from *CycloSim* for slab 1-1 geometry. The magnetic field was again set to $B = 0.05$ and a powerlaw input spectrum with exponential energy cut off was used with a photon index of $\alpha = 1.2$, a folding energy of $E_{\text{fold}} = 10$ keV, and a cut off energy of $E_{\text{cut}} = 12$ keV.

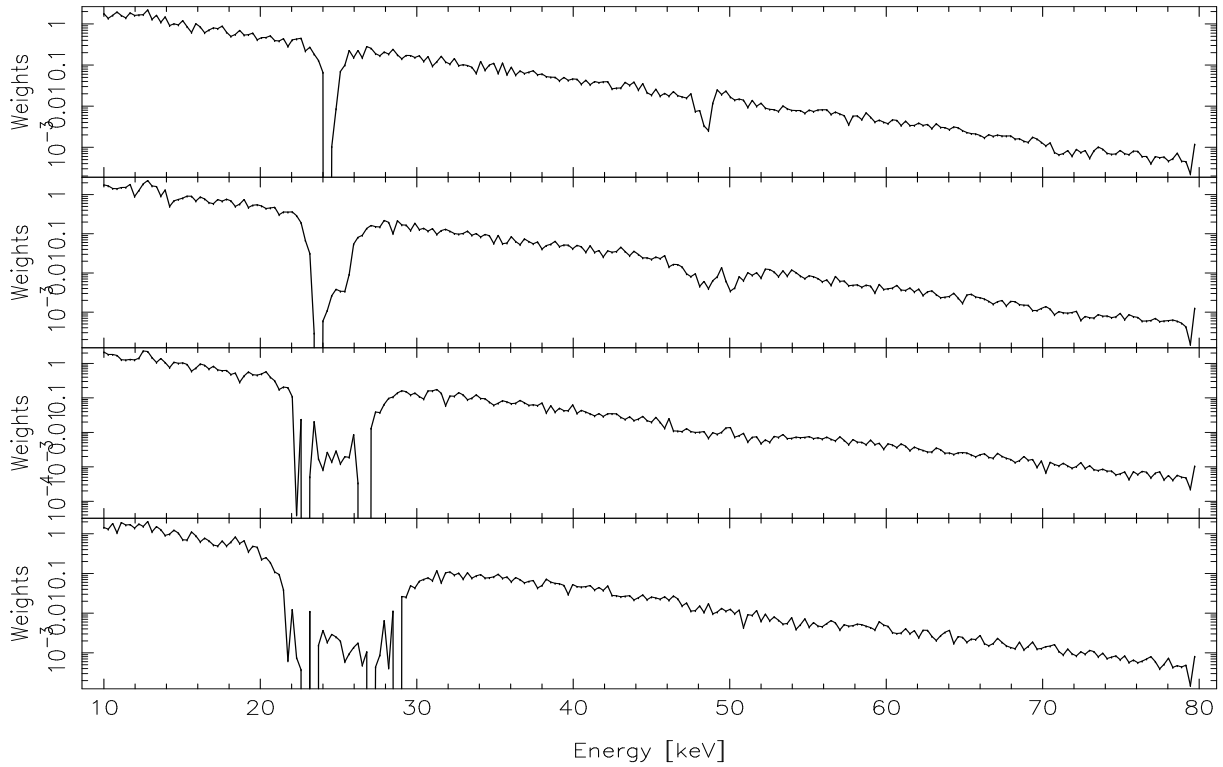


Figure 41: Spectra from *CycloSim* for cylinder geometry. See Fig. 40 for the parameters.

5 Summary and outlook

Cyclotron resonant scattering features are exposing the properties of the line forming region. By analyzing not only their position but also their shape much more information can be gained than just the magnetic field strength near to the neutron star. But several variables which are poorly constrained strongly influence the line shape. In this thesis the Monte-Carlo code from R. Araya was thoroughly revised and the mean free path calculation used up to now was replaced by a interpolation method accessing adaptively created profile tables. The new mean free paths lead to an effectively reduced optical depth by a factor of 2. This means that previously fittings with the model resulting in optical depth τ_{fit} were actually corresponding to optical depth of $\frac{\tau_{\text{fit}}}{2}$ though the shape of the fundamental would still deviate a little bit especially in the line wings. Furthermore a completely new Monte-Carlo code was developed with significantly less restrictions than other numerical models. This new code, called *CycloSim*, which is at the moment resulting in completely different spectra shall be tested in detail in future and extended further to include polarization effects.

Once reliable observational data about the polarization of X-ray binary system radiation is available even more information can be obtained. Results could potentially imply boundaries on some of the parameters which would be very useful since some parameters have to be fixed before one can get reliable values for the other ones.

Other promising possibilities to retrieve parameter boundaries are, for example, the studying of line depth ratios which seem to change significantly during an outburst and may provide first constrains for possible accretion geometries. Observational results in that direction, for example by Santangelo et al. (1999) for 4U 0115+63, often show that the second line is significantly deeper than the fundamental. This is believed to have its origin in the filling of the fundamental by spawned photons from higher landau level due to the preferred decay to landau level $n' = n - 1$ and therefore the injection of photons with energies within the full resonant width. Photons with energies slightly out of the width of the first fundamental may, for small optical depth, lead to line wings which are seen in both simulation codes but which are much less peaked in the later revisions and in the new code.

Another challenging field of research is the search for proton cyclotron lines which would appear at the proton cyclotron energy $E_{\text{cyc,p}} \approx 0.63B_{14}$ keV with B_{14} being the magnetic field strength in units of 10^{14} G. Such lines would provide evidence of neutron stars with ultra-strong magnetic fields $\geq 10^{14}$ G, also called magnetar, which perhaps exist in Soft Gamma-ray Repeaters (SGRs) and Anomalous X-ray Pulsars (AXPs) as discussed by Zane et al. (2001). A feature which is considered to be such a proton cyclotron line was found by Ibrahim et al. (2003) at 5.0 keV in an outburst of the Soft Gamma-ray Repeater SGR 1806–20. This line implies a magnetic field strength of 10^{15} G. An electron cyclotron line would result in a much weaker field and was excluded since the width of the absorption line of about ~ 0.5 keV is quite low compared to those observed for electron cyclotron lines and the resulting magnetic field in the order of 10^{11} G would be much lower than expected for SGRs. New instruments with better sensitivity will provide more information about magnetars and will allow an improvement of statistical source classifications by increasing the number of detected sources.

The Nuclear Spectroscopic Telescope Array (NuSTAR) is a satellite mission scheduled for launch in early 2012 (Harrison et al., 2010). It will be the first satellite mission to employ focusing optics in the hard X-ray band (8 – 80 keV) concurrently providing high resolution spectra by the usage of Cadmium Zinc Telluride (CdZnTe) detectors. The sensitivity will improve by a factor of 50 – 100 compared to previous collimated or coded mask imagers that have operated in this energy band (Harrison et al., 2010). The grazing incidence mirrors focus onto two shielded

solid-state pixel detectors, separated by a mast that extends the focal length to 10.15 m after launch (Koglin et al., 2009). These capabilities will allow NuSTAR to perform measurements of CRSF line profiles with unprecedented accuracy, necessitating models for CRSF profiles at the level discussed here.

Future X-ray missions like NuSTAR will also allow better measurements of the complex shape of the fundamental line and may resolve the doublet (or even triplet) splitting described in Section 4.7.3. For comparing the observational data to the old MC model the Green's functions approach from Schönherr (2007) can be used to fit the model to the data. Of course new Green's function tables have to be calculated first for taking into account the improvements of the code done as part of this thesis. Therefore the efficiency of the *accp* program which is currently limited by linear efficiency issues (see Section 4.5.4) should be improved first. Then the Green's function tables can be calculated relatively fast by interpolating photon mean free paths and electron momenta from the profile tables created by *accp*. Furthermore the new simulation code *CycloSim* will be further developed and results will be compared in the course of the CYCLO Cooperation. Some major points to be investigated are

- Comparison of Green's functions from the revised MC code and *CycloSim*
- Merging the MC models with the continuum model from Becker & Wolff (2007)
- Comparison of MC spectra and line shapes to the ones obtained by Nishimura (2008)
- Implementation of fully polarization depended calculations in the *CycloSim* code
- Angular redistribution caused by cyclotron resonant compton scattering
- Magnetic field geometry and two pole contributions (Blum & Kraus, 2000)

Along with improved observational data these studies will hopefully lead to a unified model one day revealing the last mysteries of cyclotron resonant scattering features.

References

- Abramowitz, M., & Stegun, I. A. 1964, Handbook of Mathematical Functions with Formulas, Graphs, and Mathematical Tables (Dover)
- Araya, R. A., & Harding, A. K. 1999, ApJ, 517, 334
- Barziv, O., Kaper, L., Van Kerkwijk, M. H., Telting, J. H., & Van Paradijs, J. 2001, AAP, 377, 925
- Becker, P. A. 1998, ApJ, 498, 790
- Becker, P. A., & Wolff, M. T. 2005, ApJL, 621, L45
- . 2007, ApJ, 654, 435
- Bildsten, L., et al. 1997, ApJS, 113, 367
- Blum, S., & Kraus, U. 2000, ApJ, 529, 968
- Bonazzola, S., Heyvaerts, J., & Puget, J. L. 1979, AAP, 78, 53
- Burnard, D. J., Arons, J., & Klein, R. I. 1991, ApJ, 367, 575
- Caballero, I. 2009, PhD thesis, IAAT University of Tuebingen
- Canuto, V., Lodenguai, J., & Ruderman, M. 1971, PRD, 3, 2303
- Canuto, V., & Ventura, J. 1977, Fundamentals of Cosmic Phys., 2, 203
- Chandrasekhar, S. 1931, MNRAS, 91, 456
- Coburn, W., Heindl, W. A., Rothschild, R. E., Gruber, D. E., Kreykenbohm, I., Wilms, J., Kretschmar, P., & Staubert, R. 2002, ApJ, 580, 394
- Daugherty, J. K., & Harding, A. K. 1986, ApJ, 309, 362
- Daugherty, J. K., & Ventura, J. 1978, PRD, 18, 1053
- Davidson, K. 1973, Nature, 246, 1
- Davidson, K., & Ostriker, J. P. 1973, ApJ, 179, 585
- Enoto, T., et al. 2008, PASJ, 60, 57
- Feng, W.-c. 2003, Queue, 1, 54
- Fragner, M. M., & Nelson, R. P. 2010, AAP, 511, A77
- Freeman, P. E., Lamb, D. Q., Wang, J. C. L., Wasserman, I., Lored, T. J., Fenimore, E. E., Murakami, T., & Yoshida, A. 1999, ApJ, 524, 772
- Fürst, F., et al. 2010, AAP, 519, A37+
- Goldberg, H. S., & Scadron, M. D. 1981, Physics of stellar evolution and cosmology, ed. Goldberg, H. S. & Scadron, M. D.

- Graziani, C. 1992, in BAAS 24, 756
- Gruber, D. E., Heindl, W. A., Rothschild, R. E., Coburn, W., Staubert, R., Kreykenbohm, I., & Wilms, J. 2001, ApJ, 562, 499
- Harding, A. K., & Daugherty, J. K. 1991, ApJ, 374, 687
- Harding, A. K., & Lai, D. 2006, Reports on Progress in Physics, 69, 2631
- Harrison, F. A., et al. 2010, in Instrumentation and Methods for Astrophysics, in press (arXiv:1008.1362v1)
- Heindl, W. A., Coburn, W., Gruber, D. E., Pelling, M. R., Rothschild, R. E., Wilms, J., Pottschmidt, K., & Staubert, R. 1999, ApJL, 521, L49
- Herold, H. 1979, PRD, 19, 2868
- Herold, H., Ruder, H., & Wunner, G. 1982, AAP, 115, 90
- Hoffmann, S., & Lienhart, R. 2008, OpenMP, ed. Hoffmann, S. & Lienhart, R.
- Ibrahim, A. I., Swank, J. H., & Parke, W. 2003, ApJL, 584, L17
- Isenberg, M., Lamb, D. Q., & Wang, J. C. L. 1998, ApJ, 505, 688
- Johnson, M. H., & Lippmann, B. A. 1949, Physical Review, 76, 828
- Kippenhahn, R., & Weigert, A. 1990, Stellar Structure and Evolution, ed. Kippenhahn, R. & Weigert, A.
- Kirk, J. G. 1985, AAP, 142, 430
- Klochkov, D., Shakura, N., Postnov, K., Staubert, R., & Wilms, J. 2006, ArXiv Astrophysics e-prints
- Koglin, J. E., et al. 2009, in Proc. SPIE 7437, 74370C–74370C–8
- Kretschmar, P., et al. 2005, ATEL 601, 1
- Kreykenbohm, I. 2004, PhD thesis, Univ. Tübingen
- Kreykenbohm, I., Coburn, W., Wilms, J., Kretschmar, P., Staubert, R., Heindl, W. A., & Rothschild, R. E. 2002, AAP, 395, 129
- Lamb, F. K., Pethick, C. J., & Pines, D. 1973, ApJ, 184, 271
- Latal, H. G. 1986, ApJ, 309, 372
- Levine, A. M., & Jernigan, J. G. 1982, ApJ, 262, 294
- Liermann, A., Hamann, W., Feldmeier, A., Oskinova, L. M., Rühling, U., & Todt, H. 2010, in Proc. Revista Mexicana de Astronomia y Astrofisica Conference, 38, 50–51
- McKeeman, W. M. 1962, Commun. ACM, 5, 604
- Melrose, D. B., & Parle, A. J. 1983, Australian Journal of Physics, 36, 799

- Meszaros, P. 1992, High-energy radiation from magnetized neutron stars, University of Chicago Press, Chicago
- Mihara, T. 1995, PhD thesis, Dept. of Physics, Univ. of Tokyo
- MPI Forum. Sept. 14, 2010, <http://www.mpi-forum.org/>
- Nagase, F. 1989, PASJ, 41, 1
- Nagase, F., Hayakawa, S., Sato, N., Masai, K., & Inoue, H. 1986, PASJ, 38, 547
- Nakajima, K. 2006, AGU Fall Meeting Abstracts, C5
- Nakajima, M., Mihara, T., Makishima, K., & Niko, H. 2006, ApJ, 646, 1125
- Nishimura, O. 2005, PASJ, 57, 769
- . 2008, ApJ, 672, 1127
- Nobili, L., Turolla, R., & Zane, S. 2008a, MNRAS, 386, 1527
- . 2008b, MNRAS, 389, 989
- Oppenheimer, J. R., & Volkoff, G. M. 1939, Physical Review, 55, 374
- Pavlov, G. G., Bezchastnov, V. G., Meszaros, P., & Alexander, S. G. 1991, ApJ, 380, 541
- Petterson, J. A. 1975, ApJL, 201, L61
- Rabi, I. I. 1928, Zeitschrift fur Physik, 49, 507
- Rappaport, S., Clark, G. W., Cominsky, L., Li, F., & Joss, P. C. 1978, ApJL, 224, L1
- Riffert, H. 1987, AAP, 172, 241
- Santangelo, A., del Sordo, S., Segreto, A., dal Fiume, D., Orlandini, M., & Piraino, S. 1998, AAP, 340, L55
- Santangelo, A., et al. 1999, ApJL, 523, L85
- Schanne, S., Götz, D., Gérard, L., Sizun, P., Falanga, M., Hamadache, C., Cordier, B., & von Kienlin, A. 2007, in INTEGRAL Observations of the Vela Region Focusing on Vela X-1 (eds), ESA-SP 622, Noordwijk: ESA Publications Division, 479
- Schönherr, G. 2007, PhD thesis, Univ. Tübingen
- Schönherr, G., Wilms, J., Kretschmar, P., Kreykenbohm, I., Santangelo, A., Rothschild, R. E., & Coburn, W. 2007, in Cyclotron Line Features of Magnetized Accreting Neutron Stars (eds), ESA-SP 622, Noordwijk: ESA Publications Division, 457
- Shakura, N. I., Prokhorov, M. E., Postnov, K. A., & Ketsaris, N. A. 1999, AAP, 348, 917
- Sina, R. 1996, PhD thesis, Univ. Maryland
- Sokolov, A. A., Ternov, I. M., Bagrov, V. G., Gal'Tsov, D. V., & Zhukovskii, V. C. 1968, Soviet Physics Journal, 11, 4

- Staubert, R., Shakura, N. I., Postnov, K., Wilms, J., Rothschild, R. E., Coburn, W., Rodina, L., & Klochkov, D. 2007, AAP, 465, L25
- Staubert, R., et al. 2004, in ESA Special Publication, Vol. 552, 5th INTEGRAL Workshop on the INTEGRAL Universe, ed. V. Schoenfelder, G. Lichti, & C. Winkler, 259
- Thorsett, S. E., & Chakrabarty, D. 1999, ApJ, 512, 288
- Truemper, J., Pietsch, W., Reppin, C., Voges, W., Staubert, R., & Kendziorra, E. 1978, ApJL, 219, L105
- Ventura, J. 1979, PRD, 19, 1684
- Wang, Y., & Frank, J. 1981, AAP, 93, 255
- Wheaton, W. A., et al. 1979, Nature, 282, 240
- Wilms et al. 2010, in Astrophysics of Neutron Stars 2010, AIP Conf. Proc., to be submitted
- Woosley, S. E., Heger, A., & Weaver, T. A. 2002, Reviews of Modern Physics, 74, 1015
- Zane, S., Turolla, R., Stella, L., & Treves, A. 2001, ApJ, 560, 384

Acknowledgments

This thesis would not have been possible to this extent without the help of several people whom I briefly want to thank in this section.

First of all I want to thank my advisor Jörn Wilms. He not only accepted my unusual working hours and gave me scope for development, but also helped me with advise whenever I got stuck. Furthermore he introduced me to the MAGNET community and therefore was responsible for me knowing the right persons to talk to about ideas and problems.

In that way I got to know Gabriele Schönherr. I am very grateful to her providing me all the information required for getting the MC code from R. Araya to work. She gave me lots of input for my thesis and never got tired of discussing the problems I had.

Peter Kretschmar also provided significant input. Thank you for that and for believing in my abilities to write a new simulation code!

It is impossible for a single person to consider all aspects of CRSFs and their formation. Therefore I am very glad to got to know Peter Becker and Mike Wolff whose continuum model is not only very convincing, but also capable of being merged with the Monte-Carlo approach described in this thesis. I am really excited about continuing this collaboration.

The number of numerical models simulating cyclotron profiles is rapidly increasing at the moment. Though the results agree in some aspects, they differ drastically in others. For that reason a comparison with other models is inevitable and I want to thank Osamu Nishimura for providing his profiles and spectra for such a comparison. The striking similarity of his profiles to my own calculations was an encouraging sign for me to be on the right track.

Working at the Dr. Karl Remeis Observatory was the most pleasant working experience I ever had. Bamberg is a very beautiful city and few people have the possibility to work in such a nice building complex, but the atmosphere is man-made. So I want to thank all my colleagues for being so nice. For example Manfred who helped me a lot in getting to know ISIS (I'd be interested in how often you heard this) and Ingo who actually was responsible for me choosing this topic, just to mention a few of them.

Last but not least I want to thank my mother for being the coolest mom in the world and force-feeding me during the past week.

Erklärung

Ich versichere, dass ich diese Arbeit selbstständig verfasst und keine anderen als die angegebenen Quellen und Hilfsmittel benutzt habe.

Erlangen, den 14.09.2010

.....